The Dissertation Committee for Yongjin Lee certifies that this is the approved version of the following dissertation:

First Principles-based Molecular Modeling of Thermal Transport in Silicon-based Nanomaterials

Committee:

Gyeong S. Hwang, Supervisor

John G. Ekerdt

Li Shi

Charles B. Mullins

Isaac C. Sanchez

First Principles-based Molecular Modeling of Thermal Transport in Silicon-based Nanomaterials

by

Yongjin Lee, B.S.;M.S.

Dissertation

Presented to the Faculty of the Graduate School of
The University of Texas at Austin
in Partial Fulfillment
of the Requirements
for the Degree of

Doctor of Philosophy

The University of Texas at Austin
August 2014

Dedicated to my wife Sukyoung Park and my parents, Jongman Lee and Moonhwa Hur

Acknowledgements

The person who has had the largest impact on my life these past several years is my wife, Sukyoung Park. I would like to thank her for her encouragement and support. I am blessed to have someone who shows me constant and unconditional love. Words cannot describe the amount of joy and happiness she brings into my life.

The last five years of my life in Austin has been everything that I hoped it would be, and for this I am thankful to many. My advisor, Professor Gyeong S. Hwang, provided the initial motivation for the work presented here, and allowed me to take the project where I thought it should go. I am grateful to him for his patience, enthusiasm, and willingness to discuss anything, be it about research, academia, or life in general. The other members of my committee, Professors John G. Ekerdt, Li Shi, Charles B. Mullins, and Isaac C. Sanchez, have provided support during the dissertation process. I also would like to thank all former and current members in the Hwang group for intellectually stimulating discussions and fellowship they provided, who include Soohwan Lee, Hyun Woo Kim, Sangheon Lee, Robert J. Bondi, Hyung Chul Ham, John A. Stephens, Kyoung Eun Kweon, Eunsu Paek, Chia-Yun Chou, Dhivya Manogaran, Yu-Hao Tsai, Alexander J. Pak, Haley Maren Stowe, and Myungsuk Lee.

I would like to thank the Texas Advanced Computing Center for use of their computing resources. And I am grateful for support from the Donald D. Harrington Graduate Fellows Program.

Lastly, I would like to thank my family for their endless love and support.

First Principles-based Molecular Modeling of Thermal Transport in Silicon-based Nanomaterials

Publication No.__________

Yongjin Lee, Ph.D.
The University of Texas at Austin, 2014

Supervisor: Gyeong S. Hwang

In today's nanotechnology, a critical issue is to gain the ability to control the structure and function of matter with a deeper understanding of the quantitative and qualitative relationship among their synthesis conditions, structures, and properties. Experiments may provide information regarding the behavior of nanomaterials, but their interpretations are often controversial due largely to the difficulty of direct measurement. Hereupon, with the amazing advance in computer technology since the late 20th century, computational modeling in science and engineering is increasingly important particularly in the fields of nanoscience and nanotechnology while it can provide researchers with significant insights into atomic-level interactions in various materials systems and underlying fundamental theories.

The ability of engineering thermal conductivity of materials on the nanoscale has become extremely important in various applications including electronics and energy storage/conversion technologies. Due to technical difficulties in experimentally measuring the thermal conductivity of disordered and complex nanostructures, there has been much interest in use of theoretical and computational methods to investigate thermal transport properties nanostructured materials.

One computational method that can perform an accurate analysis for the thermal conductivity of new or complex systems is molecular dynamics (MD), due to its capability of predicting the behaviors of atoms in large systems. In this work, we have developed a comprehensive MD-based computational platform capable of predicting and explaining thermal transport in disordered and complex nanostructured materials. The unique features include construction of realistic nanostructures, determination of reliable force fields, and direct simulation of large systems, which are allowed by coupling various state-of-the-art computational methods including quantum mechanics, molecular mechanics, statistical theories, and massively parallel computing.

The computational scheme was applied to describe thermal transport in various silicon and carbon-based disordered and nanostructures. First, the effects of defects including vacancy clusters, substitutional dopants, and dopant-defect complexes on the thermal conductivity of bulk crystalline silicon were investigated. Next, we analyzed the factors affecting heat transport in silicon-germanium and ternary silicon-germanium-tin alloys. Lastly, we performed the analysis of heat transport in silicon-based nanostructures such as nanowires and polycrystalline structures.

Table of Contents

List of Tables

List of Figures

Chapter 1: Introduction

1.1 Background and Motivation

Thermal conductivity is an important property in many applications including micro- and nano-electronics and optoelectronics [1-3] such as microprocessors and semiconductor light-emitting diodes, and energy conversion/storage technologies [4-10] including thermoelectric (TE) generators, photovoltaic devices, and electrochemical batteries.

For example, with advanced nanoscale fabrication processes such as molecular sputtering [11,12], chemical vapor deposition [13,14], and molecular beam epitaxy [15,16], modern electronic devices have high power densities [17] (See Fig 1.1); high power densities in the nanoscale dimensions cause generation of a significant amount of waste heat [18-20].

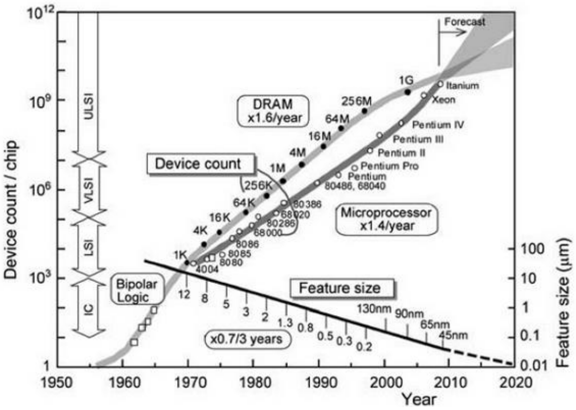

Figure 1.1: Trends in device count/chip and feature size of Metal-Oxide-Semiconductor (MOS) devices [17].

Therefore, effective heat removal is a crucial factor for thermal management engineering including the operation, stability, and reliability of nanoscale devices [21-24], which requires accurate prediction of the thermal transport properties of such small devices.

Also, with the ever growing demand for renewable energy, there has been great interest in TE energy conversion that turns waste heat into electrical energy.[25-28] Currently, in the U.S., about 60 % of the total energy is lost as waste heat in the form of hot exhaust gases, cooling water, and heat lost from hot equipment surfaces (see Fig 1.2) [29]. Therefore, recovering waste heat losses gives an attractive opportunity for an emission-free and less-costly energy resource.

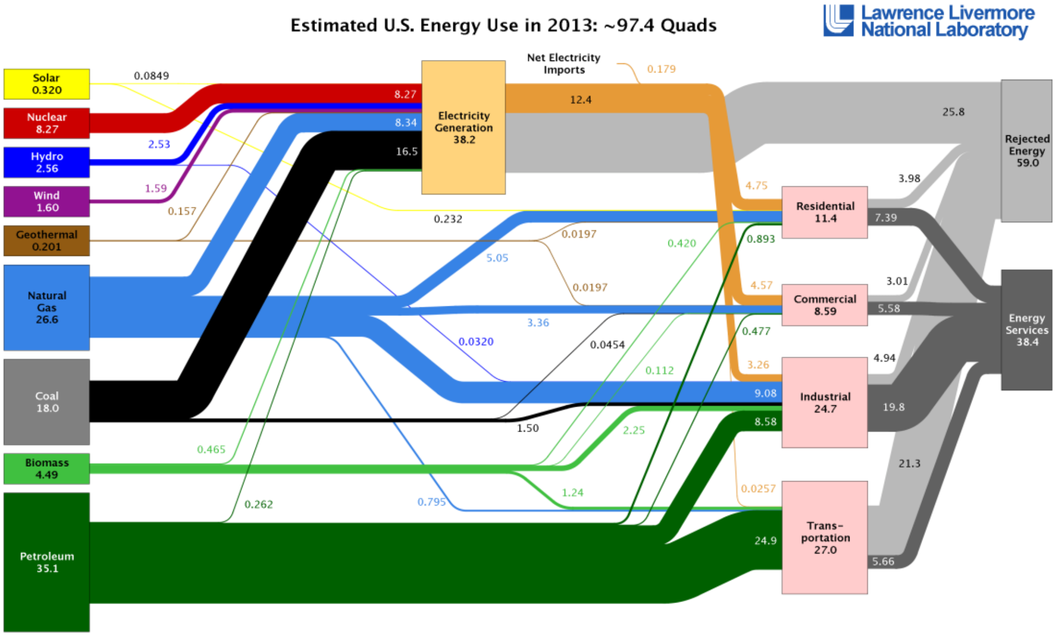

Source: LLNL 2014. Data is based on DOE/EIA-0035(2014-03), March, 2014. If this information or a reproduction of it is used, credit must be given to the Lawrence Livermore National Laboratory and the Department of Energy, under whose auspices the work was performed. Distributed electricity represents only retail electricity sales and does not include self-generation. EIA reports consumption of renewable resources (i.e., hydro, wind, geothermal and solar) for electricity in BTU-equivalent values by assuming a typical fossil fuel plant "heat rate." The efficiency of electricity production is calculated as the total retail electricity delivered divided by the primary energy input into electricity generation. End use efficiency is estimated as 65% for the residential and commercial sectors 80% for the industrial sector, and 21% for the transportation sector. Totals may not equal sum of components due to independent rounding. LLNL-MI-410527

Figure 1.2: Estimated U.S. energy use in 2013. About 60 % of the total energy is lost as waste heat. [29]

The efficiency of TE devices is measured by the figure of merit (*ZT*) which is defined in dimensionless form as: $ZT = S^2\sigma T/\kappa$, where T is the absolute temperature, S the Seebeck coefficient, and σ and κ refer to the electrical conductivity and the thermal conductivity, respectively.[30] Because *ZT* is inversely proportional to κ, disordered materials (e.g., alloys [31-35], aerogels [36-38]) are used for TE applications due to their low thermal conductivities, and there have been much efforts to develop highly efficient TE materials by reducing their κ via nanostructuring [39-43]. Therefore, significant efforts have been undertaken to increase the fundamental understanding how to control and manipulate κ of disordered or nanostructured materials.

However, experimentally measuring and characterizing the κ of disordered or nanostructured devices and materials is still challenging, due to technical difficulties caused by the extremely small size, complex geometry dependence of the thermal properties of materials [44,45], and coexistence of numerous elements affecting thermal conduction. For this reason, hence, there has been much interest in use of theoretical and computational methods to investigate the thermal transport properties for characterizing and designing nanostructured materials.

An accurate and robust prediction/description of heat transport properties requires insight into the movement and scattering of heat carriers. In a dielectric or semiconducting solid where the valence electrons are tightly bounded to the atomic nuclei, the thermal energy is mainly transported by phonons which are energy waves consisting of lattice vibrations [45]. Various approaches employing the Boltzmann transport equation (BTE) [46,47], classical molecular dynamics (MD) [48,49], or quantum-mechanics based equations [50,51] have been developed to study phonon transport in bulk and nanostructured materials.

BTE-based calculations require the properties of the full spectrum of phonon modes which are obtained by fitting the BTE solutions to experimental κ data. Therefore, these phenomenological methods have very poor predictive power; these approaches could not be applicable for new or complex systems.

To overcome this drawback, newly-developed approaches obtain the necessary phonon properties from first principles density functional theory (DFT) calculations. These methods accurately predict the phonon properties and κ of bulk or well-ordered structures [52-55]. However, there are an issue of computational cost in applying them to nanostructured systems that consist of over several thousands of atoms and disordered systems that require a supercell cell with an infinite number of atoms, by definition, despite the dramatic increase in computing power and the significant advancement of theoretical formalisms in recent years. Also, while DFT calculations using the perturbation methods [56,57] are applied to study disordered systems [58,59], their applications are often limited especially for long-range disorder systems.

In this work, we have used MD simulations. MD has good predictive power; only required inputs are atomic configurations and appropriate interatomic potentials. κ is a material property related to energy transport in non-equilibrium state, different with static and equilibrium properties such as density and specific heat. Hereupon, the rapid development of massively parallel computing techniques allows that MD predicts the position and momentum space trajectories of atoms in large systems (tens and hundreds of thousands of atoms) for sufficiently large time scales to obtain steady state within disordered and complex nanostructures. Therefore, MD simulations have potential to be capable of explaining the effect of atomic level behaviors on the κ (bulk scale property) of new and complex systems. Previously, MD simulations with empirical force fields were widely applied to estimate the κ of various materials and structures such as bulk [60,61], nanoparticles[62], nanotubes [63], and also to investigate how structural imperfections such as defects [64,65], impurities [66], surfaces [67-69], and disordered alloys [70] affect lattice κ.

However, for successful MD modeling of thermal transport in new and complex nanostructures, it is necessary to satisfy important prerequisites. First, construction of realistic structures for simulation cells is required. Phonon properties are closely related to the atomic configuration and bonding nature of materials. Therefore, it is required that simulation cells accurately represent the structural features of real systems. Also, it is essential to employ accurate force fields for thermal transport description. In MD simulations, all atomic and momentum trajectories are governed by interatomic forces calculated using force-fields. While previous empirical force fields have been successfully employed to study the structural, energetic, and mechanical properties, however, they often describe lattice dynamics unsatisfactory, and need to be improved for accurate κ estimation. For many new or complex systems, appropriate potentials for describing heat transport may not be available. Finally, while BTE- and DFT-based methods predict κ from phonon mode analysis, MD predicts κ directly at the system level. Therefore, in order to better understand complicate phonon transport phenomena in nanostructures, it may be required to perform analysis of phonon properties.

1.2 Statement of Objectives and Organization of this Dissertation

There are two major objectives for this thesis work:

1) Developing a comprehensive MD-based computational platform capable of predicting and explaining thermal transport in disordered and complex nanostructured materials. The computational approach involves the following four modules:

- Construction of realistic nanostructures with atomic-scale precision
- First principles-based determination of force fields for κ prediction
- Direct simulation of heat transport in a large system using massively parallel computing
- Detailed atomic-scale analysis to better understand complicate heat transport phenomena

2) Applying this computational scheme to investigate heat transport in various Si or C based disordered/nanostructures materials

In Chapter 2, two MD methods used for predicting κ are introduced. Also, we explain our novel force-field optimization method [71] used to obtain force fields for κ calculations.

In Chapter 3, the effects of defects on κ of bulk crystalline silicon (*c*-Si) are investigated using non-equilibrium MD simulations. First, we consider three different-sized fourfold vacancy clusters; Tetra- (V_4), hexa- (V_6), and dodeca-vacancy (V_{12}), with particular interest to study how phonon transport is affected by vacancy concentration and cluster size in association with fourfold coordination-induced lattice distortions. We discuss the correlation between phonon scattering and cluster size, based on the relative rates of vacancy scattering associated with defect-induced with strain fields. Next, we examined the underlying mechanisms for κ suppression in crystalline Si by substitutional doping with different elements (boron (B), aluminum (Al), phosphorus (P), and arsenic(As)). In particular, the relative effects of doping-induced mass disorder, bond disorder, and lattice strain were assessed using nonequilibrium MD simulations. Stillinger-Weber (SW) potential parameters for Si-dopant interatomic interactions were optimized by fitting to relevant atomic forces from first-principles calculations. Lastly, it is now well adopted that as the As doping level increases highly stable As-vacancy clusters can be formed, particularly the As_nV (n= 2, 3, 4) complex in which a vacancy (V) is surrounded by substitutional As atoms. While the phonon scattering due to defects would be a function of not only defect concentration but also defect structure, to date no research has focused on the effect of As-V clusters on the κ of Si. We attempted to investigate the effect of the As_4V complex.

In Chapter 4, heat transport in alloy systems is investigated. First, we present the effect of supercell size in predicting the κ of silicon-germanium (SiGe) alloys, which addresses the importance of a choice of supercell size. Next, we perform comprehensive MD analysis for factors affecting heat transport in SiGe alloys; particularly the effects of the composition and local segregation (microsegregation) of alloying elements. Moreover, we attempt to study heat transport in ternary silicon-germanium-tin (SiGeSn) alloys with newly optimized force fields.

Chapter 5 is dedicated to the analysis of heat transport in Si-based nanostructures. First, we investigate the origin of the reduced κ of Si nanowires (SiNWs) through a computational analysis of thermal transport in SiNW with tailored surface structures. Next, we present a computational analysis of thermal transport in SiGe alloy nanowires (SiGeNWs), with particular focus on the relative roles of alloy scattering and boundary scattering to the significant reduction of κ. Next, a new concept of core-shell NWs by utilizing SiGe alloys is proposed and its impact on thermal transport in the core-shell structures is examined using MD simulations. Furthermore, in order to address the grain size and boundary effects on heat transfer, a new Monte Carlo-based method is developed to generate polycrystalline structures, and the effect of grain boundaries on thermal transport is discussed.

Lastly, in Chapter 6, the important results of the work presented are summarized.

Chapter 2 Theoretical Background

2.1 Molecular Dynamics Methods for Predicting Thermal Conductivity

2.1.1 Non-Equilibrium Molecular Dynamics

In Non-equilibrium molecular dynamics (NEMD)[72], κ is obtained according to Fourier's law, by: $J = -\kappa\, dT/dz$, where J is the steady-state heat flux and dT/dz is the temperature gradient. NEMD is analogous to an experimental procedure, in which the heat flux (or temperature gradient) is calculated from the imposed temperature gradient (or heat flux). In our NEMD calculations, the temperature gradient is obtained from the imposed heat flux, as implemented in Large-scale Atomic/Molecular Massively Parallel Simulator (LAMMPS)[76]. To induce heat flow, we define a heat sink(S_C) and a heat source(S_H) in each simulation cell, as shown in Fig. 2.1. The velocity vectors of the hottest atom in the heat sink and the coldest atom in the heat source are interchanged (if the hottest atom has a higher kinetic energy than the coldest atom). The unphysical energy transfer (from the cold region to the hot region) leads to a heat flow in the opposite direction by thermal conduction. At steady state, both fluxes are equal in magnitude, and the total heat flux is obtained from the sum of the kinetic energies transferred. As such, the κ of a given system is then calculated by:

$$\kappa = -\frac{J}{(\partial T)} = -\frac{\sum_{swaps} (m/2)(v_{hot}^2 - v_{cold}^2)}{2tA(\partial T)} \tag{2.1}$$

where v_{hot} and v_{cold} refer to the velocities of the atoms involved in the energy exchange in the cold and hot segments, respectively, t is the simulation of time, A is the cross-sectional area perpendicular to the heat flow direction, and ∂T is the temperature gradient in the longitudinal direction. The factor of 2 in the denominator indicates that heat flows in two directions due to the periodic boundary condition imposed in the *longitudinal* direction (see Fig. 2.1.).

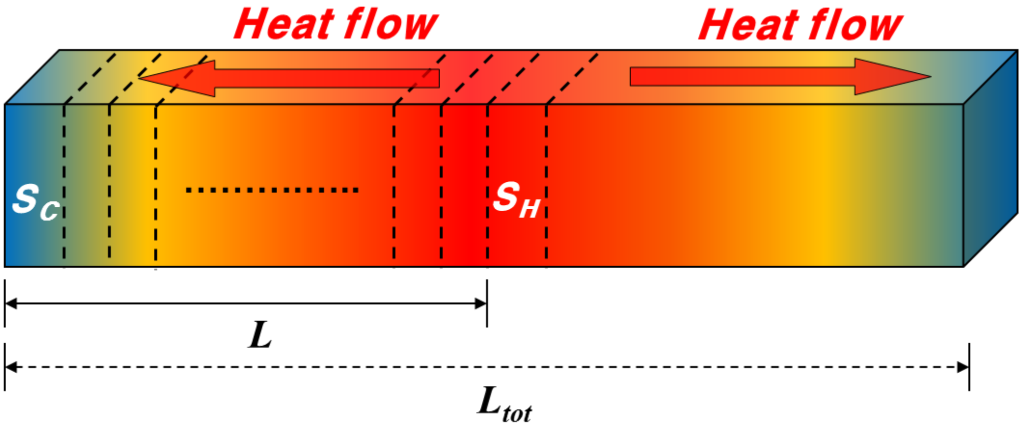

Figure 2.1: Schematic illustration of a rectangular-shaped simulation domain with periodic boundary conditions imposed in all three directions. The simulation cell consists of several layers including heat source (S_H) and two heat sink (S_C) layers; Heat flows in two directions due to the periodic boundary condition imposed in the longitudinal direction, as indicated. $L = 1/2L_{tot}$ where L_{tot} is the total length of the simulation cell.

In the direct method, the predicted κ is a function of simulation cell length. If the axial length of the simulation cell is not sufficiently longer than the mean free path of phonons in the system, phonon scattering in the heat sink and source regions may inhibit thermal conduction and consequently lower κ.[77,78] The finite-size effect is often unavoidable if a finite-size simulation cell is employed in determination of bulk thermal conductivities. That dependence can be removed by extrapolating the simulation results with various finite-size cells to the infinite system. According to Schelling *et al.*[60], the relationship between size-dependent κ and simulation cell length ($L_{tot} = 2L$, where L is the distance between the centers of the heat source and sink layers, which is a half of the total simulation cell length) is given by: $1/\kappa \propto 1/l_\infty + 2/L$,where l_∞ is the phonon mean free path for the infinite system. From linear extrapolation with a set of calculated ($1/L$, $1/\kappa$) values to $1/L = 0$, we can approximate the bulk κ.

This method, on the basis of Matthiessen's rule, assumes that the inverse of the effective phonon mean free path (l_{eff}) can be obtained by adding the inverses of the bulk phonon mean free path (l_∞) and the boundary scattering contribution (in a finite system), i.e., $1/l_{eff} = 1/l_\infty + 2/L$. The factor of 2 in the boundary scattering term accounts for the mean scattering distance of phonons traveling from the heat source to the heat sink. According to the simple kinetic theory, $\kappa = 1/3\, C_v \mathrm{vl}$, where C_v is the specific heat of phonons per unit volume, v is the group velocity of acoustic branches, and l is the mean free path of phonons, the thermal resistivity ($1/k$) is given by: $1/\kappa = 1/\kappa_\infty + \alpha/L$ where α is a size-independent constant ($= 6/C_v v$). Thus, we can evaluate the bulk κ by extrapolating a corresponding $1/\kappa$ *vs* $1/L$ plot to $L \rightarrow \infty$ (or $1/L \rightarrow 0$).

2.1.2 Equilibrium Molecular Dynamics

The Equilibrium molecular dynamics (EMD) method relies on the fact that the regression of the thermal fluctuations of an internal variable, in our case the thermal flux, obeys macroscopic laws. Hence, the time decay of the fluctuations of the flux is proportional to the κ based on the fluctuation-dissipation theorem[75]. This is mathematically expressed by the Green-Kubo formalism [73,74] which states that the time integral of the heat flux autocorrelation function is proportional to the thermal conductivity tensor [79].

$$J(\mathrm{t}) = \frac{d}{dt}\sum_i r_i(t)\varepsilon_i(t) \tag{2.2}$$

$$\kappa = \frac{1}{3k_BT^2\Omega}\sum_{\alpha=1}^{3}\int_0^{\infty}\langle J_\alpha(0)J_\alpha(t')\rangle dt' \tag{2.3}$$

where r_i is the position of atom i, ε_i is the total energy density associated with atom i, k_B is the Boltzmann constant, T is the temperature, Ω is the volume of the system, and α runs over Cartesian coordinates. The integration of Eq.(2.3) is the heat current autocorrelation function. A large number of time origins within the ensemble average are required for good convergence. The Green-Kubo approach generally requires a higher computational cost than NEMD, which tends to be its major drawback.

2.1.3 Quantum Correction of Thermal Conductivity Predicted by MD

In the MD approach, the temperature is commonly calculated from the velocities of constituent atoms based on the equipartition theorem of classical statistical mechanics: $\frac{3}{2}Nk_BT_{MD} = \frac{1}{2}\sum_{i=1}^{N} mv_i^2$,where N is the number of atoms in a chosen region (one unit or shell here), k_B is the Boltzmann constant, v_i is the velocity of atom, and m is the atomic mass. However, when the system temperature is below the Debye temperature, quantum corrections to the MD temperature and κ are necessary. By assuming that the total system energy is the mean kinetic energy at T_{MD} and equals to the total phonon energy at a quantum temperature T, the quantum correction can be:

$$< E >= \frac{3}{2} N k_B T_{MD} = \int_0^{\omega_D} D(\omega)(\frac{1}{2} + \frac{1}{\exp(\hbar\omega / k_B T) - 1})\hbar\omega d\omega \tag{2.4}$$

where $D(\omega)$ is the phonon density of states for all acoustic branches, ω is the phonon frequency, and the ½ in the phonon energy term represents the effect of zero point energy. Here, the phonon occupation number is described in terms of the Planck distribution function ($\frac{1}{\exp(\hbar\omega / k_B T) - 1}$). From $J = -\kappa_{MD} \frac{dT_{MD}}{dz} = -\kappa \frac{dT}{dz}$, the corrected κ is estimated to be[80] $\kappa = \kappa_{MD} \frac{dT_{MD}}{dT}$.

2.2 First Principles-based Force Field Parameterization using Force Matching Approach

Empirical force fields such as three-body SW[25] and Tersoff[81] interatomic potentials have been successfully employed to study the structural, energetic, and mechanical properties of Si-based materials[82,83]. However, their description of lattice dynamics is often unsatisfactory despite its importance in assessing thermal transport properties[84]; for instance, previous MD simulations based on original SW and Tersoff parameters yielded significant overestimates of κ of Si, i.e., 235.7±7.5 $\mathrm{Wm^{-1}K^{-1}}$ at 300K (Tersoff[65]) and 119±40 $\mathrm{Wm^{-1}K^{-1}}$ at 500 K (SW[60]), as compared to experimental values of 130 W/mK at 300K and 76.2 $Wm^{-1}K^{-1}$ at 500 K[85]. It is likely an insurmountable task to generate a single force field that can provide an adequate description of all physical and chemical properties, even for a prototypical semiconductor like Si. Therefore, it would be necessary to at least modify existing force fields for specific applications, such as lattice κ calculations.

While lattice dynamics directly depends on force constants between atoms[86], earlier studies demonstrated substantial improvement in description of lattice dynamical properties through modification of relevant force constants. Jian *et al*.[87] showed that the SW potentials modified to fit the available experimental values of bulk modulus and phonon frequencies (particularly optical mode at the Γ point and transverse acoustic mode at the X point) yielded considerably improved phonon-dispersion relations for Si and Ge. Very recently, Lindsay and Broido[88] presented improved Tersoff and Brenner potential parameters for phonon thermal transport in carbon nanotubes and graphene that were optimized to better fit measured phonon frequencies and zone-center acoustic velocities.

The main framework of our force-field optimization method is as follows. First, the DFT force data for parameter optimization were obtained by displacing selected atom in the *x*, *y*, and *z* directions. The restoring forces acting on the displaced atom and its neighbors were considered to be matched in the parameter adjustments. The optimal values for parameters were obtained through minimization of the cross-validation error (ξ); $\xi^2 = \frac{1}{N}\sum_{n=1}^{N}(F_{DFT}^{(n)} - F_{FF}^{(n)})^2$, where $F_{DFT}^{(n)}$ and $F_{FF}^{(n)}$ refer to the DFT and force-field forces, respectively, of the n^{th} of N total training data for force matching.

2.2.1 Application to Bulk Silicon

To improve the description of lattice dynamics, using a force-matching method[26] we adjusted three SW parameters (σ, ε, and λ) to fit DFT results for both the lattice spacing and the lattice restoring forces arising from local lattice distortions.

Within the SW[25], the total energy (Φ) is given by the sum of two- (Φ_2) and three-body (Φ_3) interactions:

$$\Phi(r) = \sum_{i,j(i<j)} \Phi_2(r_i, r_j) + \sum_{i,j,k(i<j<k)} \Phi_3(r_i, r_j, r_k) \tag{2.5}$$

The two body potential (Φ_2) is a function only of radial distance (r), described in terms of a combination of inverse powers and an exponential function [Eq. (2.6)], and the three-body potential possess full translational and rotational symmetry to give a diamond structure of solid Si, given as the product exponential and cosine functions [Eq. (2.7)].

$$\Phi_2(r_{ij}) = \begin{cases} \varepsilon A(Br_{ij}^{-p} - r_{ij}^{-q})\exp\left[1/(r_{ij} - a)\right], & r_{ij} < a \\ 0 & r_{ij} \geq a \end{cases} \tag{2.6}$$

$$\Phi_3(r_i, r_j, r_k) = h(r_{ij}, r_{ik}, \theta_{ijk}) + h(r_{ij}, r_{jk}, \theta_{ijk}) + h(r_{ki}, r_{kj}, \theta_{ikj}) ; \tag{2.7}$$

$$h(r_{ij}, r_{ik}, \theta_{jik}) = \varepsilon\lambda \exp\left[\gamma/(r_{ij} - a) + \gamma/(r_{ik} - a)\right](\cos\theta_{jik} + 1/3)^2$$

where the subscripts *ij*, *ik*, and *jik* represent pairs and triplets involving atoms *i*, *j*, and *k*, r_{ij} is the interatomic distance between atoms *i* and *j* (normalized by a characteristic length σ), and θ_{ijk} is the angle between bonds *ij* and *ik*.

In the original study, the seven parameters (A, B, p, q, a, λ, and γ) were adjusted to give a diamond lattice structure in the solid state and fit MD simulation results to experimental observations for melting temperature and liquid structure. In addition, the values of σ and ε were chosen to match the observed lattice constant and atomization energy of crystalline Si at 0K, respectively. Although the SW potential overall gives a fairly realistic description of crystalline Si, as stated earlier the thermal conductivities calculated based on the original SW parameters[25] tend to be overestimated. Since lattice dynamics directly depends on force constants between atoms[86], this implies that the original set of parameters may describe the Si lattice somewhat rigid, which is probably related to the fact that the energy-scaling parameter (ε) was fitted to the atomization energy at 0K. Note that thermal conduction at a finite temperature inherently involves lattice fluctuations, e.g., the mean atomic displacement in *c*-Si is about 0.077 Å at room temperature[28]; such thermal-induced lattice distortions would lead to a softening of the lattice and consequently require smaller force constants in describing the thermal transport properties near or above room temperature.

To improve the description of lattice dynamics, using a force-matching method [26] we adjusted three SW parameters (σ, ε, and λ) to fit DFT results for both the lattice spacing and the lattice restoring forces arising from local lattice distortions. The values of σ were chosen to match the LDA/GGA lattice constants for the Si diamond structure. In the SW potential, εA and ελ determine the relative strength between the two- and three-body interactions. Since A is preset, ε and λ were tuned to fit the DFT restoring forces.

Our DFT calculations were performed within the local density approximation (LDA) and the Perdew-Wang 91 generalized gradient approximation (GGA-PW91)[89], using the Vienna Ab initio Simulation Package (VASP)[90]. We used Vanderbilt-type ultrasoft pseudopotentials [91] to represent the interaction between ion cores and valence electrons, and a planewave basis set with a kinetic energy cutoff of 160 eV. We used a 64-atom cubic supercell and a (2×2×2) k-point grid in the scheme of Monkhorst-Pack for the Brillouin zone sampling. The predicted GGA (LDA) Si lattice constants are 5.4571 (5.3865) Å, which were used for MD simulations.

The DFT force data for parameter optimization were obtained by displacing one atom in the *x*, *y*, and *z* directions by 0.2 Å; the magnitude of the displacements was carefully determined from test calculations with different values which were greater than the mean atomic displacement of about 0.077 Å in *c*-Si at 300K[28]). The restoring forces acting on the displaced atom and its four first- and twelve second-nearest neighbors were considered to be matched in the SW parameter adjustments. On the third-nearest neighbors and beyond, the forces due to the center-atom displacement are negligible (< 0.01 eV/ Å in the absolute value). The optimal values for ε and λ were obtained through minimization of the cross-validation error (ξ); $\xi^2 = \frac{1}{N}\sum_{n=1}^{N}(F_{DFT}^{(n)} - F_{SW}^{(n)})^2$, where $F_{DFT}^{(n)}$ and $F_{SW}^{(n)}$ refer to the DFT and SW forces, respectively, of the n^{th} of N total training data for force matching.

Table 2.1: Parameters of the Stillinger Weber interatomic potential; original[25] [SW(ORI)] and modified values based on fit to GGA [SW(GGA)] and LDA [SW(LDA)] calculations (this work).

	Σ	ε (eV)	λ	
SW(ORI)	2.0951	2.1683	21	A = 7.049556277 B = 0.6022245584 γ = 1.2 a = 1.8 p = 4.0 q = 0.0
SW(GGA)	2.1051937	1.41992	29.5304	
SW(LDA)	2.0780213	1.49662	26.4091	

Table 2.1 summarizes the modified parameters based on GGA [SW(GGA)] and LDA [SW(LDA)] calculations, together with the original parameters [SW(ORG)] for comparison. In Fig. 2.2, we compare the restoring forces from the SW and DFT calculations; both SW(GGA) and SW(LDA) well reproduce the DFT forces acting on the center atom and its neighbors while SW(ORG) yields consistently overestimated values. In the three-body SW potential, the forces can be decoupled into two- (F) and three-body (G) contributions; that is, $F = \frac{1}{3\sigma^2}\frac{d^2\Phi_2}{dr^2}\Big|_{r=2^{1/6}}$ and $G = \frac{8\varepsilon\lambda}{27\sigma^2 r^2}\exp(\frac{2r}{r-a})\Big|_{r=2^{1/6}}$, where σ, ε, λ, and *a* are the SW parameters. Looking at the relative two- and three-body forces of SW(GGA) and SW(LDA) with respect to SW(ORI), there is a significant reduction in the two-body forces (γ_F= 0.65/0.70 for GGA/LDA) while the three-body force reduction is relatively smaller (γ_G= 0.91/0.88 for GGA/LDA). The decrease of forces indicates that SW(GGA) and SW(LDA) will describe the Si lattice softer than SW(ORI).

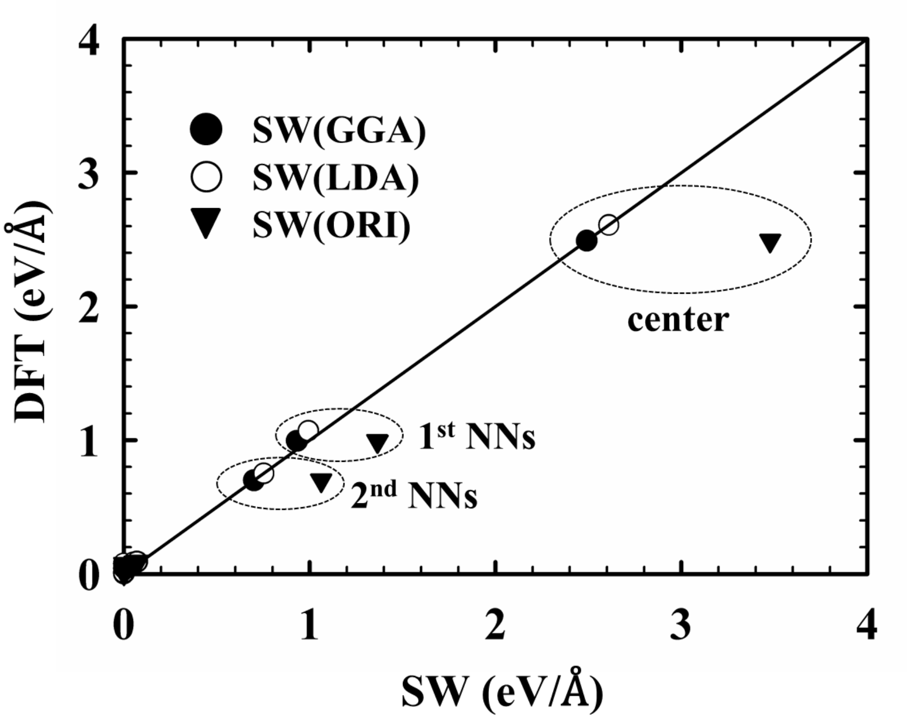

Figure 2.2: Discrepancies between DFT and SW predictions for the restoring forces acting on the displaced atom (center) and its four first- (1st NNs) and twelve second-nearest neighbors (2nd NNs)

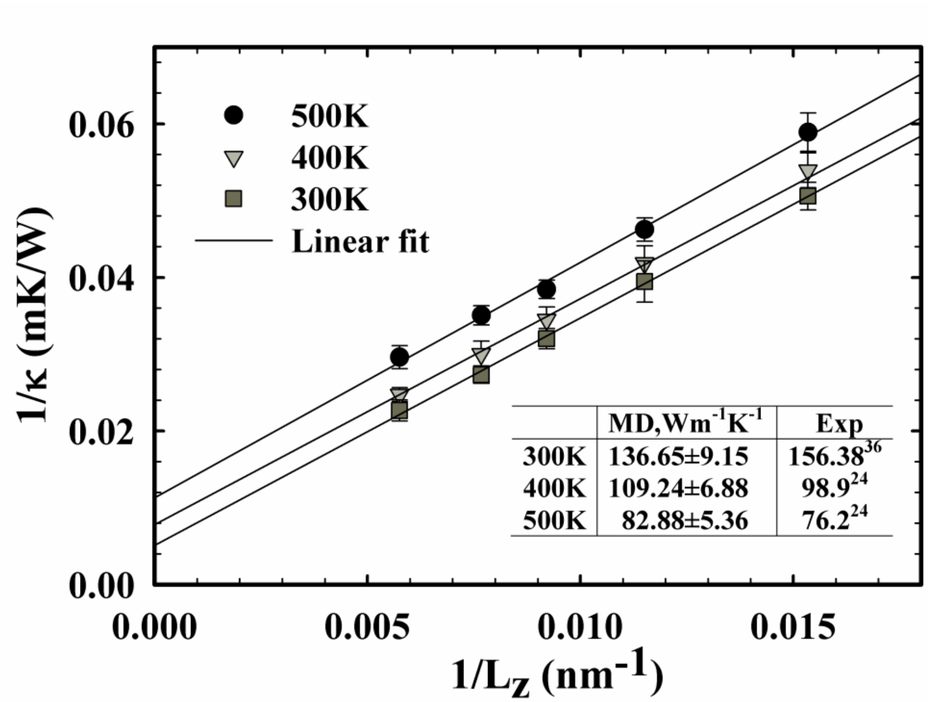

	MD, $Wm^{-1}K^{-1}$	Exp
300K	136.65±9.15	156.38[36]
400K	109.24±6.88	98.9[24]
500K	82.88±5.36	76.2[24]

Figure 2.3: Thermal resistivity (1/*κ*, after quantum corrections) for *c*-Si as a function of simulation cell length at three different temperatures as indicated; for each set, the linear line indicates the best-fit linear regression. L_z is the distance between the heat source and heat sink centers, which is half of the total simulation domain length (L_{tot}). The inset summarizes the calculated thermal conductivities of *c*-Si based on SW(GGA), with the available experimental values for comparison.

As shown in Fig. 2.3, we calculated the bulk thermal conductivities of *c*-Si by extrapolating calculated ($1/L_z$, $1/\kappa$) values to $1/L_z = 0$. For each system, we performed ten independent NEMD simulations with different initial velocity distributions to obtain good statistics; the system was initially equilibrated at a target temperature within the canonical (NVT) ensemble with a Nosé-Hoover thermostat for 100 picoseconds (*ps*), followed by 2000 *ps* of microcanonical (NVE) MD while imposing a heat flux (with a velocity swap interval of 100 MD steps) and measuring the ensuing temperature gradient. A time step of 1 femtosecond (*fs*) was adopted for all MD simulations reported herein.

Each calculated temperature profile was obtained by averaging over 10^5 MD steps (100 *ps*) after equilibrium was reached. Those chosen conditions have been proven to be sufficient to provide reasonable results for all cases considered.

We calculated thermal conductivities at 500K for three different sets of SW parameters. Here, the relatively high temperature (= 500K) was intentionally chosen to check the reliability of the modified parameter sets while minimizing (or avoiding) the possible errors associated with quantum corrections[80]; the corrections are only on the order of ≈ 7% at 500K for the experimental value (= 645K) of the Debye temperature. After quantum corrections, the calculated κ values of 82.88 ± 5.36 $Wm^{-1}K^{-1}$ and 83.84 ± 7.71 $Wm^{-1}K^{-1}$ based on SW(GGA) and SW(LDA), respectively, are in good agreement with the experimental value of 76.2 $Wm^{-1}K^{-1}$ [85], while SW(ORI) leads to a considerable overestimation (124.97 ± 14.02 $Wm^{-1}K^{-1}$). This result clearly demonstrates that the modified parameter sets derived from both GGA and LDA forces can describe reasonably well the κ of Si; we expect that the force-matching approach can also be applicable to other materials. The calculated κ values (after quantum corrections) based on SW(GGA) at 300K and 400K also listed in the inset of Fig. 2.3. The overall good agreement with experiment suggests that the force-matched SW potentials would be a reliable choice for describing Si thermal transport properties in the temperature regime.

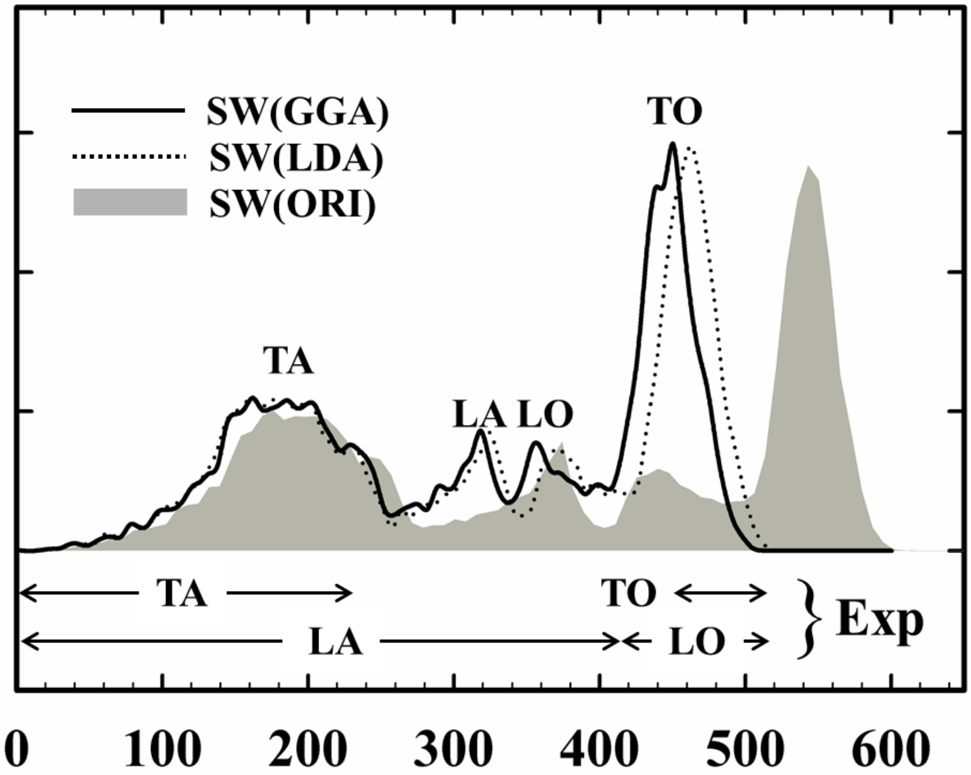

Figure 2.4: Phonon density of states (PDOS) calculated based on different sets of SW parameters, as indicated; each of which consists of four longitudinal acoustic (LA), transverse acoustic (TA), longitudinal optical (LO), and transverse optical (TO) branches. For comparison, the relative positions of the four phonon branches extracted from experimental phonon-dispersion relations[92,93] are also presented, as indicated.

Figure 2.4 shows calculated phonon density of states (DOS) based on the modified and original parameters sets, together with relevant experimental data for comparison. For each case, the vibrational modes were determined by diagonalizing a Hessian matrix obtained from numerical differentiation of analytical forces that were calculated by displacing all constituent atoms (in a 512-atom cubic supercell) in the *x*, *y*, and z directions by 0.02 Å. The phonon spectrum is composed of four branches such as longitudinal acoustic (LA), transverse acoustic (TA), longitudinal optical (LO), and transverse optical (TO). The force-matched potentials [SW(GGA) and SW(LDA)] reasonably well reproduce the relative positions of the four peaks as observed in earlier experiments[92,93]; on the other hand, the original parameter set [SW(ORI)] yields the upshifted frequencies (blue shift). The blue shift of the phonon branches is directly related to the increase of phonon group velocity; hence, SW(ORI) is well expected to cause overestimation of κ, according to the kinetic theory, $\kappa \propto \nu C_v l$, where v is the group velocity of acoustic branches, C_v is the specific heat of phonons per unit volume, and l is the mean free path of phonons[85].

Finally, we compared the phonon dispersion relations of c-Si from SW(GGA)/SW(ORI)-based calculations using the GULP computer program[94]. As shown in Fig. 2.5, the most noticeable difference between the SW(GGA)- and SW(ORI)-based dispersion curves occurs in the description of optical branches. The SW(ORI) significantly overestimates the optical frequencies while the SW(GGA) and experimental values are in good agreement; the highest optical frequency of 502.57/514.48 cm^{-1} (at Γ) as estimated from the SW(GGA)/SW(LDA) calculations is much closer to the experimental measure[93] of 518.0284 cm^{-1}, compared to the SW(ORI) value of 594.76 cm^{-1}. The optical frequency overestimation may lead to the reduced phase space for phonon-phonon scattering, as the three-phonon phase space tends to be inversely related to the characteristic phonon frequency scale determined by the highest optical frequency[95,96]. As a result of the reduction of three-phonon umklapp scattering processes, the SW(ORI) likely causes a significant overestimation of the κ at room temperature and above where phonon scattering dominates.[97] The results unambiguously suggest that the improved prediction of κ by the modified SW(GGA)/SW(LDA) parameter sets is largely due to their tendency to yield a better fit to the phonon frequencies, as compared to the original SW(ORI) parameter set.

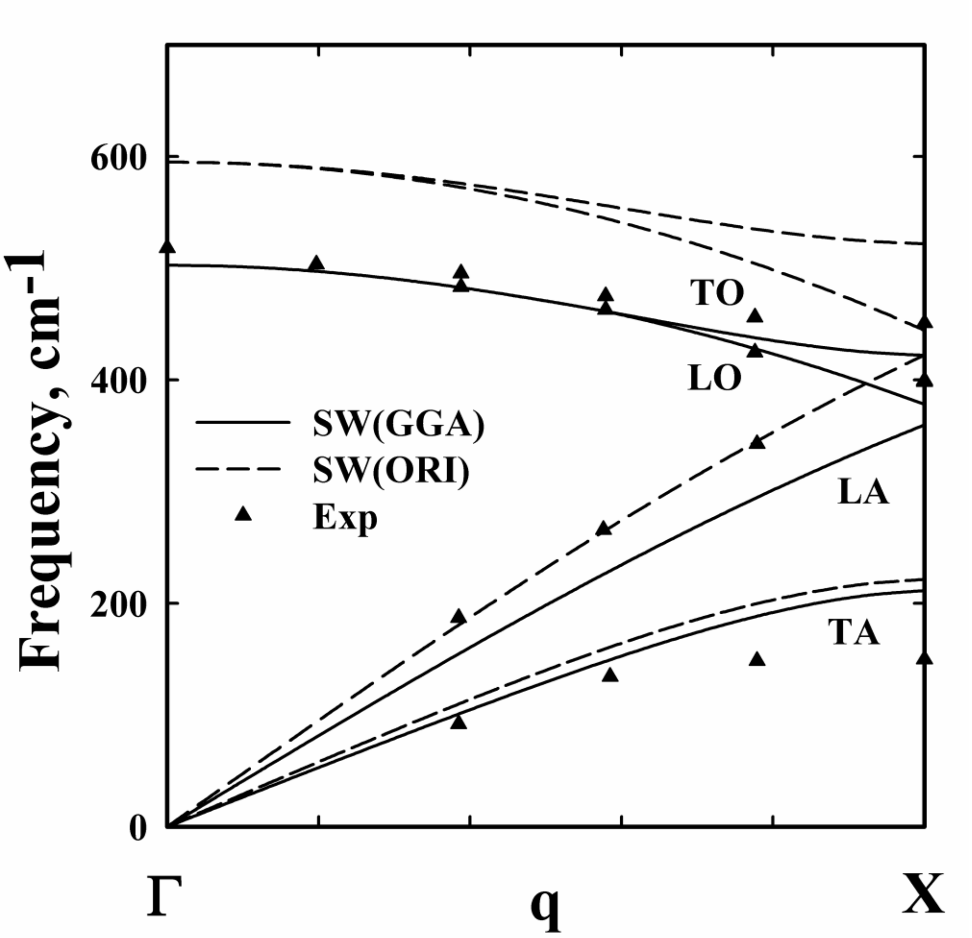

Figure 2.5: Phonon dispersion for *c*-Si along high-symmetry directions. The SW(GGA) and SW(ORI)-based calculations were performed using the GULP (General Utility Lattice Program) computer program[94]. The solid and dashed lines correspond to the modified [SW(GGA)] and original [SW(ORI)] parameter sets, respectively. Triangles indicate experimental data from Ref. [93].

2.2.2 Application to Magnesium Silicide (Mg_2Si)

In order to test the ability of our force matching approach in obtaining accurate force fields for describing heat transport in complex materials, we also attempted to re-optimize first principles-based force fields for Mg_2Si. The compounds of Mg_2Si and their solid solutions have recently been of interest for a TE application due to their demonstration of high *ZT*s in the medium temperature range of 500-800 K [30,98]. Unlike covalently-bonded Si, Mg_2Si exhibits both ionic and covalent bonding characters, as shown in Fig 2.6. Therefore, Mg_2Si can be a good model system to test the applicability of our approach to various types of bonding and force field formula.

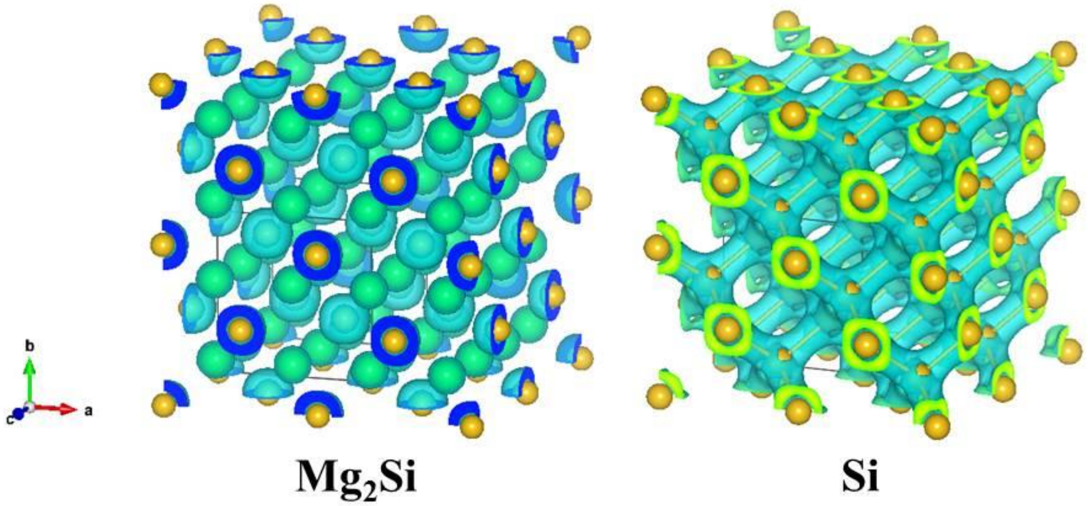

Figure 2.6: Color map (3D) showing atomic configuration and partial charge distribution of Mg_2Si and Si. Partial charge distribution was obtained from the Bader charge analysis[99].

To describe the atomic interactions between Mg-Mg, Mg-Si, and Si-Si, the Buckingham potential function [100] was employed. This potential consists of an exponential term to describe the repulsive potential between atoms, an r^{-6} attractive term, and long range term for coulombic interactions. The general Buckingham potential function is given by:

$$\mathrm{U} = A_{ij} e^{-r_{ij}/\rho_{ij}} - \frac{C_{ij}}{r_{ij}^{6}} + E_c \tag{2.8}$$

Three adjustable parameters (A_{ij}, ρ_{ij}, C_{ij}) are used to match the potential function to the structural and energetic properties.

To describe the long range coulombic interactions, the Wolf summation method [101] was employed. This method is based on the observation that the Coulombic summation does not converge as a result of the potential non-neutrality of the total charge contained within the spherically truncated system of cutoff radius r_c.[102] If charge-neutralization of such a system is achieved, the correct equivalent system energy can be computed by

$$E_c \;=\; \frac{1}{2}\sum_{i=1}^{N}{}_{j\neq i}\sum_{r_{ij}<r_c} \frac{q_i q_j}{r_{ij}}\Big(erfc(\alpha r_{ij})\Big) - \lim_{r_{ij}\to r_c} \frac{q_i q_j}{r_{ij}}\Big(erfc(\alpha r_{ij})\Big) \tag{2.9}$$

$$-\left(\frac{\Big(erfc(\alpha r_{ij})\Big)}{2r_c} + \frac{\alpha}{\sqrt{\pi}}\right)\sum_{i=1}^{N} q_i^2$$

The first term represents the traditional coulombic sum, the second term represents the unbalanced surface charges within the sphere of radius r_c, which are subtracted from the total energy [103], and the third term explains the shift in the correct energy of the system by the charge neutralized energy. For each term, a damping function is applied in order to make this method computationally more efficient. The damping parameter α determines how fast the complementary error function ($\mathrm{erfc}(\alpha r_{ij})$) decays to zero [101], which sets the cutoff radius r_c necessary for the system to converge. In this study, the r_c was set to 12 Å, and α was thus carefully determined between 0.1 and 0.5.

Table 2.2: Optimized Parameters of the Buckingham interatomic potential for Mg_2Si.

	Si-Si	Si-Mg	Mg-Mg
A_{ij}(eV)	3620.69	3687.26	1816.36
ρ_{ij}(Å)	0.4221	0.3186	0.3535
C_{ij}(eVÅ^6)	1207.64	281.53	269.91
	q_{Mg} = 0.66897, q_{Si} = -1.33794		

In Table 2.2, the optimized parameters from the force matching approach are summarized. In this work, 10 parameters (q_{si}, A_{ij}, B_{ij}, and C_{ij}, where i,j = Mg or Si) were optimized using a force-matching method [71]. To satisfy the charge-neutrality condition, we set $q_{Mg} = -\frac{1}{2}q_{Si}$. Using a 96-atom cubic supercell (with 32 Si and 64 Mg atoms), DFT force data for the parameter optimization were obtained by displacing one Si or Mg atom in the *x*, *y*, and *z* directions by 0.1~0.2 Å. All DFT calculations were performed within GGA-PW91 [89], using the VASP[90]. We used Vanderbilt-type ultrasoft pseudopotentials [91] to represent the interaction between ion cores and valence electrons, and a planewave basis set with a kinetic energy cutoff of 300 eV. We used a (4×4×4) k-point grid in the scheme of Monkhorst-Pack for the Brillouin zone sampling.

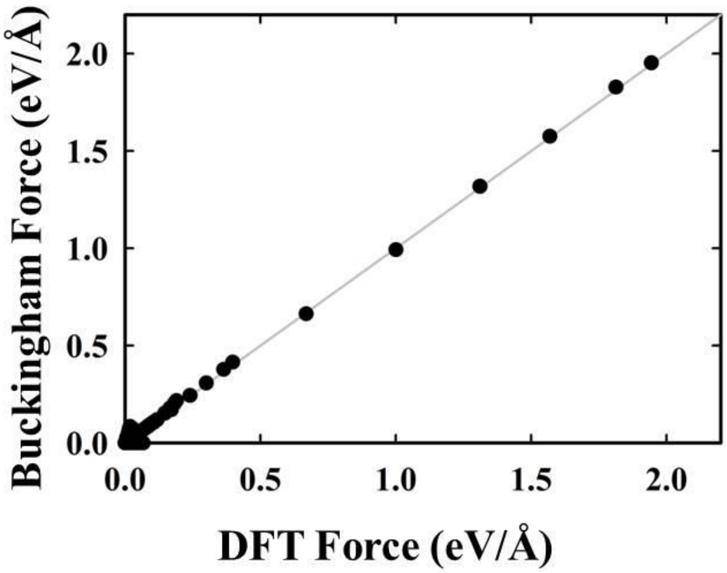

Figure 2.7: Comparison between predicted DFT and Buckingham potential forces acting on the Mg and Si atoms. Gray linear line indicates |Buckingham Force| = |DFT Force|.

Figure 2.7 shows the comparisons of the restoring forces from our modified potential and DFT-GGA calculations; overall, the modified Buckingham potential parameters provide excellent reproduction of corresponding DFT forces. Next, we tested our optimized potential for MD trajectories. MD trajectories were obtained using a 768-atom rectangular periodic cell. The system was first equilibrated at 300K within the canonical (NVT) ensemble with a Nosé-Hoover thermostat for 100 picoseconds (*ps*) with a time step of 0.5 femtosecond (*fs*). After equilibration, trajectories were obtained within the NVE ensemble at every 10000 time steps. Figure 2.8 shows the comparisons of forces from our modified potential and DFT calculations for several MD trajectories. Overall, the modified Buckingham potential parameters well reproduce corresponding DFT forces. It is noteworthy that the restoring forces on individual atoms from MD are within the range of force data for force matching processes, which confirms the validity of imposed displacement on each atom in the force matching approach.

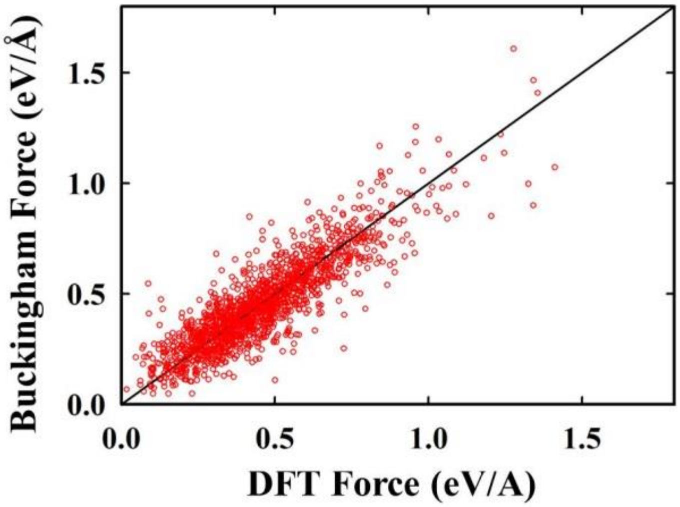

Figure 2.8: Comparison between predicted DFT and Buckingham forces acting on the Mg and Si atoms for MD snapshots of 768 atoms supercell. Gray linear line indicates |Buckingham Force| = |DFT Force|.

The phonon density of states (PDOS) of the 4116-atom Mg_2Si cell calculated using our optimized potential is compared in Fig 2.9 with DFT results on a small 324-atom cell. The eigenmodes of the system and their frequencies are obtained by direct diagonalization of the dynamical matrix, computed using the finite differene method with the atomic forces. Compared to DFT, the force-matched potential reproduces the relative positions of phonon branches reasonably well; longitudinal acoustic (LA), transvers acoustic (TA), longitudinal optical (LO), and transverse optical (TO).

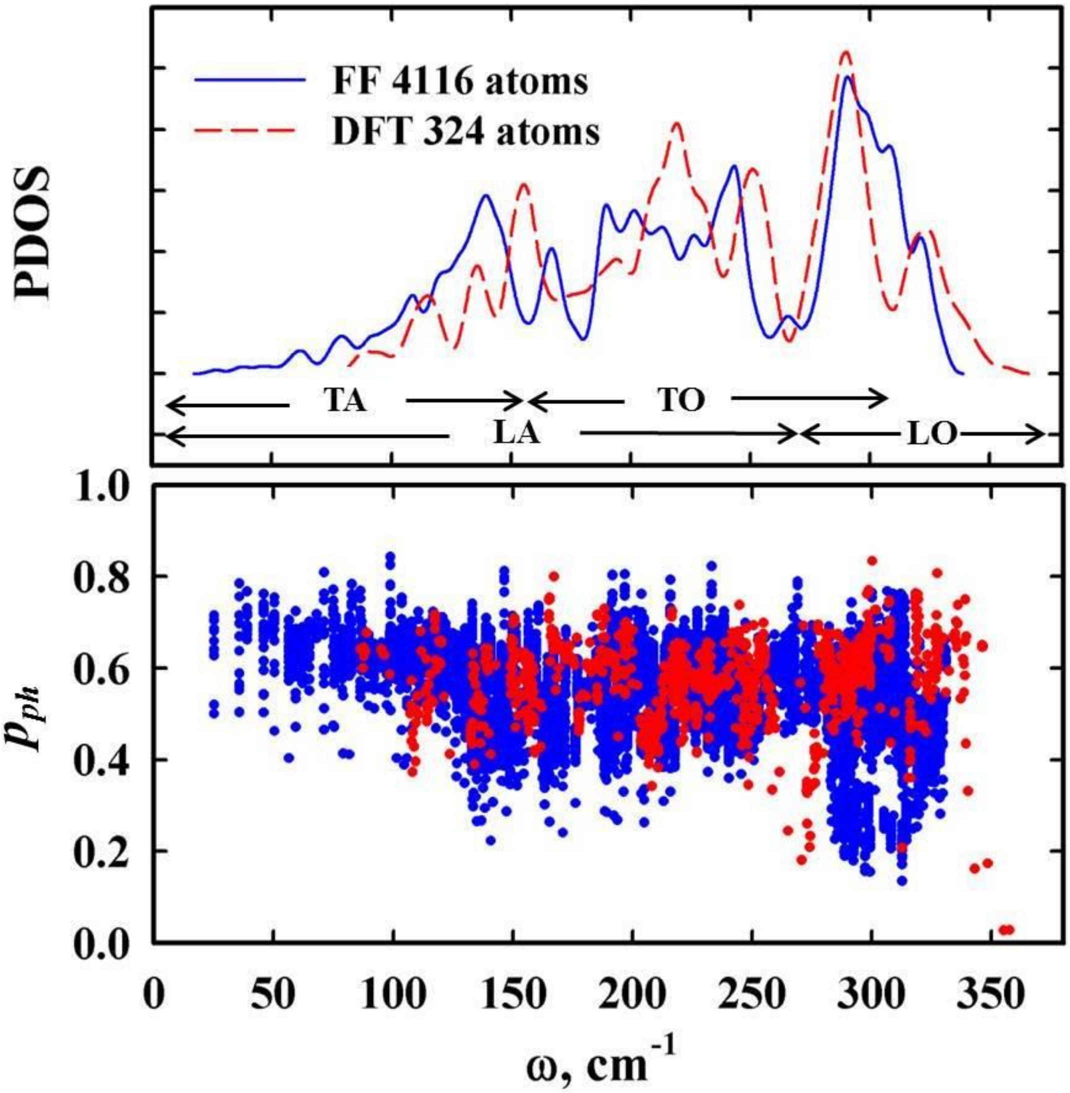

Figure 2.9: Phonon density of states (PDOS) and phonon participation ratio (p_{ph}) for Mg_2Si calculated using DFT and optimized Buckingham forcefield(FF). PDOS consists of four longitudinal acoustic (LA), transverse acoustic (TA), longitudinal optical (LO), and transverse optical (TO) branches. Blue (or red) solid line or dots indicates PDOS or p_ω obtained using FF (or DFT), respectively.

A discrepancy is present in describing phonon properties over 330 cm^{-1}, because the optimized potential which lacks the Born effective charges does not reproduce LO/TO splitting at the Γ point which is a redshift of the LO mode away from the TO mode (LO-TO splitting) [56] typically observed in polar semiconductors like Mg_2Si. Although there has been no study directly explaining the effect of LO/TO splitting at the Γ point on κ predicted by MD, we could expect that the effect is not significant, based on Shiomi et al.' recent study [104] which stated the inclusion of the non-analytical term for LO/TO splitting negligibly affects first-principles-based κ prediction. Also, it is noteworthy that PDOS for the DFT model don't yield values for low frequencies below 100 cm^{-1} due to its small cell size.

While the PDOS gives information averaged over all vibrational modes present in the structure, the participation ratio p_{ph}, characterizes each mode individually and serves as a useful discriminant of spatial localization. p_{ph} is defined for an eigenmode with frequency ω as [105,106] $p_{ph}^{-1} = N \sum_j \left(\sum_\alpha \varepsilon_{j\alpha}^{*} \varepsilon_{j\alpha} \right)^2$, where N_T is the total number of atoms and ε is the eigenvector corresponding to the eigenmode with frequency ω. Indicating the fraction of atoms participating in a given normal mode of vibration, the value of p_{ph} always lies between 1 and $1/N_T$; that is, $p_{ph} = 1$ if all N_T atoms vibrate with equal amplitude while $p_{ph} = 1/N_T$ for a mode involving only one atom. The values of p_{ph} for the optimized force field and DFT of Mg_2Si are reported in Fig 2.9. The overall shape of p_{ph} is reasonably reproduced by the optimized force field.

We calculated the lattice $\kappa(\kappa_L)$ of Mg_2Si as a function of temperature from 300K to 700K. For NEMD simulations, we employed a rectangular-shaped simulation domain with periodic boundary conditions imposed in the *x*, *y*, and *z* directions, where heat conduction occurs in the *z* (or <100>) direction. We adopted the DFT optimized lattice constant of 6.342 Å along <100> which is in good agreement with an experimentally reported value of 6.338 Å [107]. The cross-sectional area of each simulation domain is 3.802×3.802 nm^2, while the domain is axially divided into a number of thin shells (each of which contains 432 atoms). The thickness of the heat source and heat sink layers is set to L_S = 6.342 Å (corresponding to one shell in the axial direction or 432 atoms), and the total axial length of the rectangular domain varies from L_{tot} = 40.58, 81.17, 121.76, and 162.35 nm (corresponding to 64, 128, 192, and 256 shells, respectively). For each system, we performed ten independent NEMD simulations with different initial velocity distributions; the system was initially equilibrated at a target temperature within the NVT ensemble with Nosé-Hoover thermostat for 500 picoseconds (*ps*), followed by 4000 *ps* of constant energy (NVE) MD while imposing a heat flux and measure the ensuing temperature gradient. A time step of 0.5 femtosecond (*fs*) was adopted for all MD simulations reported herein. Each bulk κ value was obtained through extrapolation of finite-size results to infinite size.

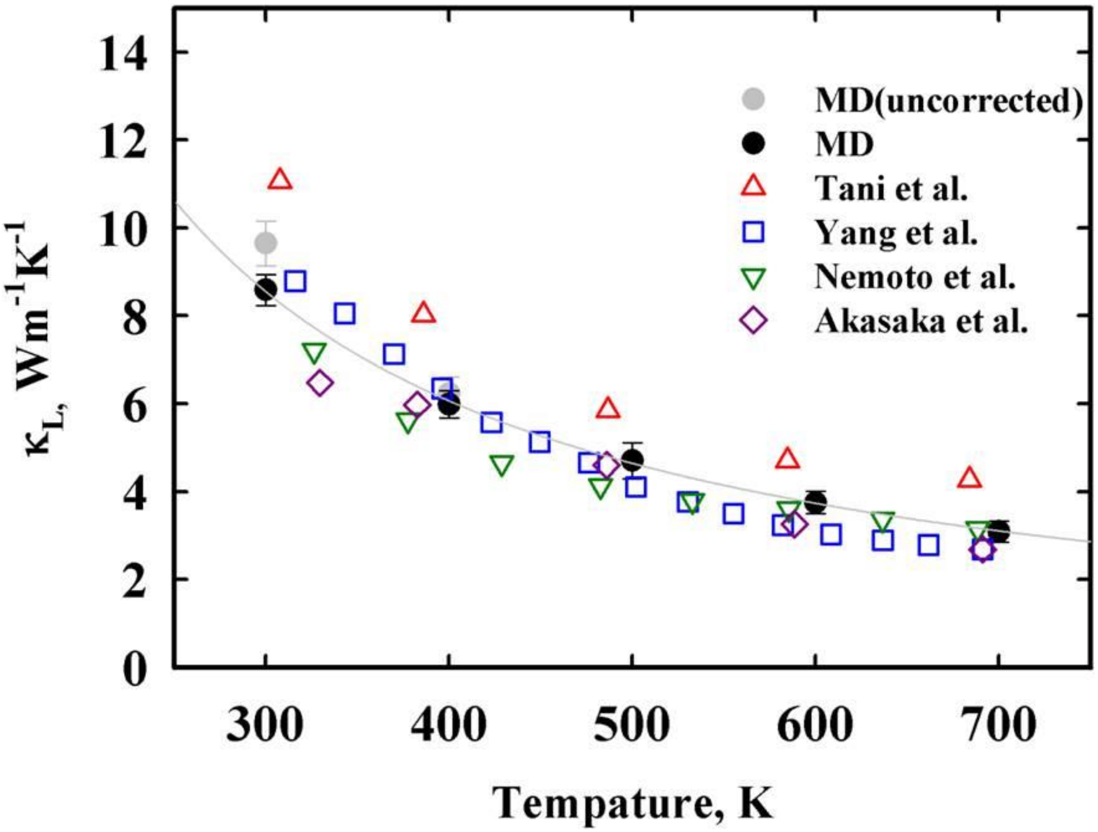

Figure 2.10: Calculated lattice thermal conductivities (κ_L) of Mg_2Si versus temperatures with experimental data of Tani et al.[108], Yang et al.[109], Nemoto et al.[110], and Akasaka et al.[111]. Filled grey circles correspond to MD results without quantum correction.

Figure 2.10 shows predicted κ_L in comparison with available experimental data [108-111]. Experimental data for κ_L were extracted from the measured total κ using the Wiedemann-Franz law. We can see that the predicted values by MD are in good agreement with previous experimental data. Especially, we compare calculated κ_L with experimental ones at 500, 600, and 700K which are higher than the Debye temperature (=419 K[112]) of Mg_2Si, because MD results below the Debye temperature require quantum corrections which might cause extrinsic errors [80]. At 500, 600, and 700K, κ_L is predicted to be 4.70±0.41, 3.75±0.24, and 3.09±0.29 $Wm^{-1}K^{-1}$, showing good agreement with the corresponding experimental values of 4.10 [109], 3.03, and 2.68 $Wm^{-1}K^{-1}$ at 501.9, 608.3, and 691.1 K, respectively. The predicted κ_L decreases monotonically with increasing temperature, indicating an increase in phonon-phonon scattering which is the primary source of thermal resistance for Mg_2Si. [113]. The gray line is a fit by $\kappa \propto T^{-\alpha}$ with α = 1.19, which is quite consistent with earlier experimental studies showing the κ_L of Mg_2Si is proportional to T^{-1}. This result clearly demonstrates that the modified parameter sets derived from DFT forces can describe reasonably well the lattice κ of Mg_2Si. The overall good agreement with experiments suggests that the force-matched potentials would be a reliable choice for describing the thermal transport properties of Mg_2Si in the temperature range examined.

Chapter 3 Effect of Defects on Thermal Conductivity of Crystalline Silicon

3.1 Introduction

Recently there have been several attempts to utilize Si-based materials for TE application, while compound semiconductors have been widely used for TE materials.[31,114,115] Si is more abundant, safer, and cheaper than compound semiconductors and also has well-established low-cost process technology, making it attractive for TE applications. However, bulk crystalline Si (*c*-Si) is well known to be a very inefficient TE material because of its high κ; the *ZT* of bulk Si is 0.01 at room temperature.[116] Much research[117-120] has been directed towards finding ways to reduce the κ of Si-based materials to increase *ZT*. While heat conduction in Si is mainly governed by phonon transport, recently many attempts have been made to suppress the κ by introducing phonon scattering through nanostructuring, doping, and alloying.[67,70, 121] Phonon-boundary scattering has been found to bring about a substantial reduction of κ in Si nanostructures such as nanowire and thin film. Moreover, introduction of defects and dopant impurities at the atomic level is expected to lower the κ[117-120]

In bulk *c*-Si, mono- and di-vacancies are likely mobile even at room temperature[122,123], and thus most vacancies have been thought to remain in the form of clusters or complexes with other defects and impurities. According to very recent theoretical studies[124,125], small vacancy clusters (V_n, $3 \leq n \leq 48$) tend to be fourfold coordinated by nullifying dangling bonds created by Si lattice atom removal; in this size regime, the bond energy gain by fourfold-coordination is predicted to exceed the strain energy increase via consequent lattice distortions. Unlike point-like defects, phonon scattering due to vacancy clusters would be a function of not only vacancy concentration but also cluster size[126]. Particularly, the fourfold coordination of vacancy defects can cause significant lattice distortions around them, which could play an important role in impeding phonon transport.

In addition, the presence of chemical impurities in Si would lead to scattering of phonons, which can in turn significantly influence κ suppression. Substitutional dopants result in a significant reduction in κ of Si. With a Ge concentration of 6.2×10^{19} cm^{-3}, the κ of Ge-doped Si layers was reduced by nearly a factor of two [127]. For dopants concentrations in the range over 10^{20} cm^{-3}, bulk Si doped with boron (B) or phosphorous (P) shows the reduction in κ as large as a factor of 20 at 300K [128]. Despite their significant roles in κ suppression, the atomic-level mechanisms underlying the phonon-impurity scatterings in Si-based materials have been an ongoing problem and need to be further investigated. To the best of our knowledge, most of the earlier theoretical investigations [117,129,130] have focused on explaining the variation of κ with temperature and dopant concentration based on Klemens formula [131] and Holland model[132], not the specific contributions of different dopants. Garg et al.[57] performed a detailed analysis of alloying effect on κ in bulk SiGe alloy, which addressed the effect of mass disorder. Unlike SiGe, other dopants may show other effects besides mass disorder.

Furthermore, in the current semiconductor technology, ever higher doping levels are required due to the continuing decrease of device scales[133]. In many theoretical studies[134-136] in addition to recent experiments[137,138], it have been reported that as the doping level increases, highly stable As clusters formed with a vacancy (V) surrounded by substitutional As atoms (As_nV), with n = 2,3,4. Due to the As clustering phenomena, Si layers with these doping levels may exhibit unexpected properties such as a higher electrical resistance [139]. While phonon scattering due to defects would be a function of not only defect concentration but also defect structures, to date any research has not focused on the effect of As clusters on the κ of Si.

In this chapter, we discuss how the presence of vacancy defects, substitutional and agglomerated dopants affects the κ of Si using non-equilibrium MD simulations. First, the role played by fourfold vacancy clusters in scattering of phonons in bulk *c*-Si is investigated, particularly the concentration and size effects, using three different-size clusters (V_4, V_6, and V_{12}). Next, with the SW potential model[25] modified based on the first principles-based force matching method[71], our present study attempts to address the underlying causes of phonon-impurity scattering for different types of dopants, especially related to the mass disorder, bond disorder, and lattice strain induced by dopant incorporation. Lastly, the effect of defect-dopant agglomeration on the κ of As-doped Si is investigated, with comparison to that of fully dispersed substitutional dopants.

3.2 Effect of Vacancy Defects on Thermal Conductivity of Si

3.2.1 Fourfold-Coordinated Vacancy Clusters

As model defects, we adopted stable fourfold-coordinated tetra- (V_4), hexa- (V_6), and decavacancy (V_{12}) clusters from the previous work of Lee and Hwang[124]; the predicted lowest energy configurations of the vacancy clusters are shown in Fig. 3.1. The fourfold-coordinated structures remained stable during MD simulations at 300K, which is not surprising considering that all Si atoms are fourfold coordinated with no significant distortions. The predicted formation energies (per vacancy) of 2.04, 1.53, and 1.15 eV using the Tersoff potential are close to the DFT values of 1.88, 1.62, and 1.16 eV for V_4, V_6, and V_{12}, respectively. This implies that the empirical potential can describe reasonably well the structure and energetics of fourfold-coordinated vacancy defects where the bond lengths and bond angles insignificantly deviate from their equilibrium values.

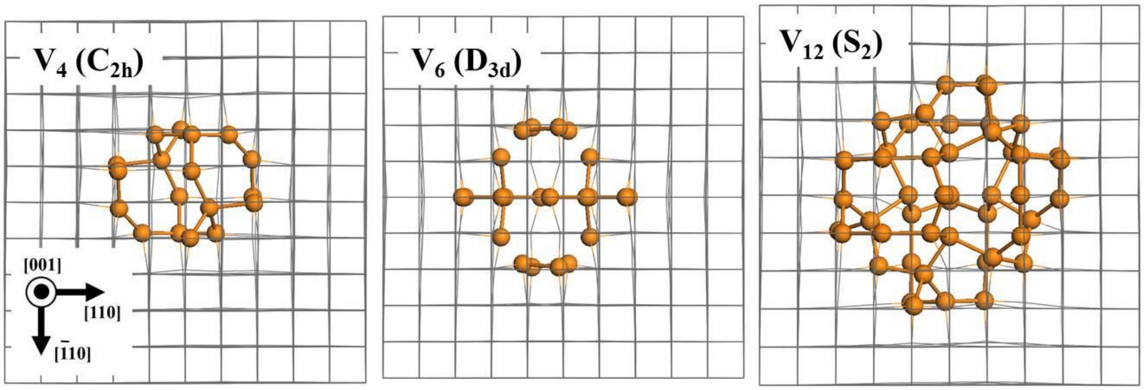

Figure 3.1: Minimum energy configurations of fourfold tetra- (V_4), hexa- (V_6), and deca-vacancy (V_{12}) clusters considered in this work. Wire frame represents bulk Si lattice, and spheres represent highly strained atoms due to the fourfold coordination of the neighboring atoms around the vacancies.

3.2.2 Effect of Vacancy Clusters on Thermal Conductivity

For each simulation cell, either V_4, V_6 or V_{12} clusters at a given concentration were randomly embedded in the middle layers which are separated from the heat sink and source layers by 5.4313 nm-thick buffer layers, as illustrated in Fig. 3.2. As such, the periodic simulation cell consists of heat source and sink layers (indicated as S_H and S_C, respectively), two vacancy-embedded intermediate (I) layers, and two buffer (B) layers. Since there is velocity switching-induced non-physical phonon scattering in the heat source/sink segments[77,78], it might be necessary to place vacancy defects outside those regions to better assess phonon transport in the defective structures with no unphysical scattering effect. In addition, we assured that linear temperature gradients were established in the vacancy-embedded layers by adjusting the length of buffer layers (in which temperature profiles were frequently highly non-linear).

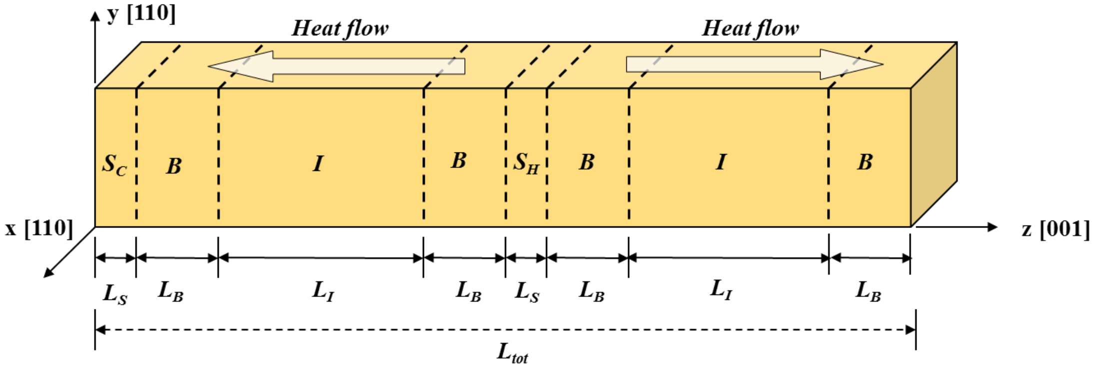

Figure 3.2: Schematic illustration of the three-dimensional periodic simulation cell that consists of heat source (S_H), heat ink (S_C), buffer (B), and intermediate (I) layers; corresponding layer thicknesses (L_S, L_B, L_I) are also shown. Vacancy clusters are randomly embedded only in the intermediate (I) layers to avoid the influence of velocity switching-induced non-physical phonon scattering in the heat source and sink regions. Heat flows in two directions due to the periodic boundary condition imposed in the <100> direction, as indicated.

For all simulation cells, fixed lattice constants of 5.4313Å along <100> and 3.8405Å along <110> were used for *c*-Si, as obtained from volume optimization with the Tersoff potential model. The cross-section of each simulation cell consists of 10×10 units (corresponding to 3.8405 × 3.8405 nm^2 or 400 atoms). The heat source/sink layer with a thickness of L_S = 5.4313 Å contains one unit in the axial direction (corresponding to 400 atoms), and the thickness of each buffer layer was set to L_B = 54.313 Å (corresponding to 10 units in the axial direction or 4000 atoms). The axial length of the vacancy-embedded intermediate layer was varied from L_I = 21.7252, 43.4504, 65.1756, to 86.9008 nm (corresponding to 40, 80, 120, and 160 units, respectively, in the <100> direction). Periodic boundary conditions are imposed in the *x*, *y*, and *z* directions, while heat conduction occurs in the *z* direction.

For the composite simulation cell employed in this work, the overall thermal resistivity equals to the length-weighted average resistivity:

$$\kappa_{eff}^{-1} = \{(2L_B + L_S)/L_z\}\kappa_B^{-1} + (L_I/L_z)\kappa_I^{-1}, \tag{3.1}$$

$$\text{from} \quad J = -\kappa_{eff}\frac{\Delta T}{L_z} = -\kappa_S\frac{\Delta T_S}{L_S} = -\kappa_B\frac{\Delta T_B}{L_B} = -\kappa_I\frac{\Delta T_I}{L_I},$$

where $\Delta T = \Delta T_S + \Delta T_B + \Delta T_I$ and $\kappa_S = \kappa_B$. The effective conductivity is rewritten as:

$$\kappa_e = \frac{\kappa_B\kappa_I}{\kappa_I\delta_B + \kappa_B\delta_I} \tag{3.2}$$

where $\delta_B = (2L_B + L_S)/L_z$ and $\delta_I = L_I/L_z = 1 - \delta_B$. Substituting Eq.(3.1) into Eq.(3.2), we obtain

$$\frac{1}{\kappa_{eff}} = \frac{1}{\kappa_B}\delta_B + \frac{1}{\kappa_I}\delta_I = \left(\frac{1}{\kappa_\infty} + \frac{\alpha}{2L_B + L_S + L_I}\right) \tag{3.3}$$

If $L_I >> 2L_B+L_S$ (or $\delta_B \approx 0$ and $\delta_I \approx 1$), the κ of the composite cell (κ_{eff}) can be assumed to be equal to that of the vacancy-embedded matrix (κ_I). Thus, we can evaluate the contribution of vacancy scattering to bulk κ by extrapolating a corresponding $1/\kappa_{eff}$ *vs* $1/L_z$ plot to $L_z \rightarrow \infty$ (or $1/L_z \rightarrow 0$)

For the sake of reference, first we calculated κ for bulk *c*-Si at 300K by extrapolating the simulation results with various finite-size cells to the infinite system. Since the defect free *c*-Si system has higher κ (i.e., a smaller intercept in the $1/\kappa$ vs. $1/L_z$ plot) than other defected systems, a relatively longer simulation cell is needed for more precise extrapolation. Within the composite cell scheme, the intermediate layer thickness (L_I) was varied from 21.7252, 43.4504, 65.1756, 86.9008, to 130.3512 nm (corresponding to 40, 80, 120, 160, and 240 units, respectively, in the <100> direction), while the thicknesses of the heat source/sink and buffer layers were fixed at L_S = 5.4313 Å and L_B = 54.313 Å, respectively.

The insets of Fig. 3.3 show temperature profiles from the longest and shortest simulation cells, which clearly demonstrate that the temperature profiles in the intermediate layers (hatched) are well fitted to linear functions while they are virtually symmetric about the center of the heat source (or sink) layer. This advocates that heat conduction in the intermediate layers obeys Fourier’s law with no significant interference from the heat source and sink, and it also occurs symmetrically in the simulation domain.

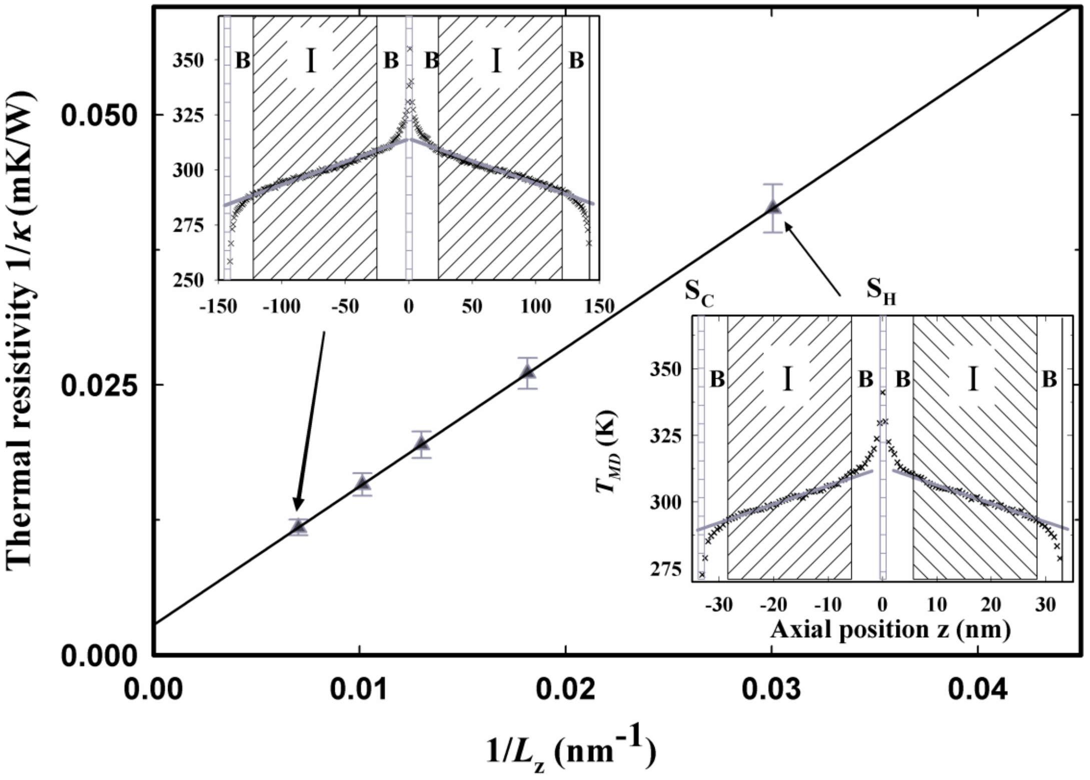

Figure 3.3: Thermal resistivity (1/*κ*, with quantum correction) for defect-free Si as a function of simulation cell length at 300 K. L_z is the distance between the centers of the heat source and sink layers, which is a half of the total simulation cell length (L_{tot}). Insets show MD temperature (T_{MD}) profiles as function of axial position (z) from the longest and shortest simulation cells, exhibiting linear temperature gradients in the intermediate layers (hatched), as represented by thin solid lines. In the insets, S_H, S_C, B, and I indicate the heat source, heat sink, buffer, and intermediate layers, respectively.

In Fig 3.3, calculated $1/\kappa$ values are plotted as a function of $1/L_z$, exhibiting a linear pattern. From a standard least squares linear regression, the slope and intercept of the $1/\kappa$ vs $1/L_z$ plot are estimated to be 2.56×10^{-9} m^2K/W and 0.0028 mK/W, respectively. From the intercept, the predicted κ value of 235.71 ± 7.53 $W/m^{-1}K^{-1}$ (before quantum correction = 357.14 ± 11.41 $W/m^{-1}K^{-1}$) appears to be overestimated compared to the experimentally reported value of 156 $W/m^{-1}K^{-1}$ [85]. This discrepancy could be attributed to the tendency that the Tersoff potential would describe the Si structure somewhat rigid.[140] Taking the slope and intercept values, we also estimated the bulk phonon mean free path by: l_∞ = [slope]/[2 × intercept]; the predicted value of 228.991 ± 10.521 nm is comparable to 300 nm as experimentally estimated.[141,142]

Next, we examined how the presence of vacancy defects affects κ. For each defect type, we considered four different vacancy concentrations (n_v = 0.15, 0.6, 0.9, and 1.5%.). Figure 3.4 shows selected time-averaged temperature profiles that were used to compute κ for V_{12} at n_v = 0.15, 0.6, 0.9, and 1.5%. All of the temperature profiles are fitted by linear functions (represented by solid lines) in the vacancy-embedded intermediate layers, although strong nonlinear profiles are shown in the buffer layers, particularly near the heat source/sink layers. This confirms that the defective regions are not affected by the unphysical scattering associated with velocity swapping.

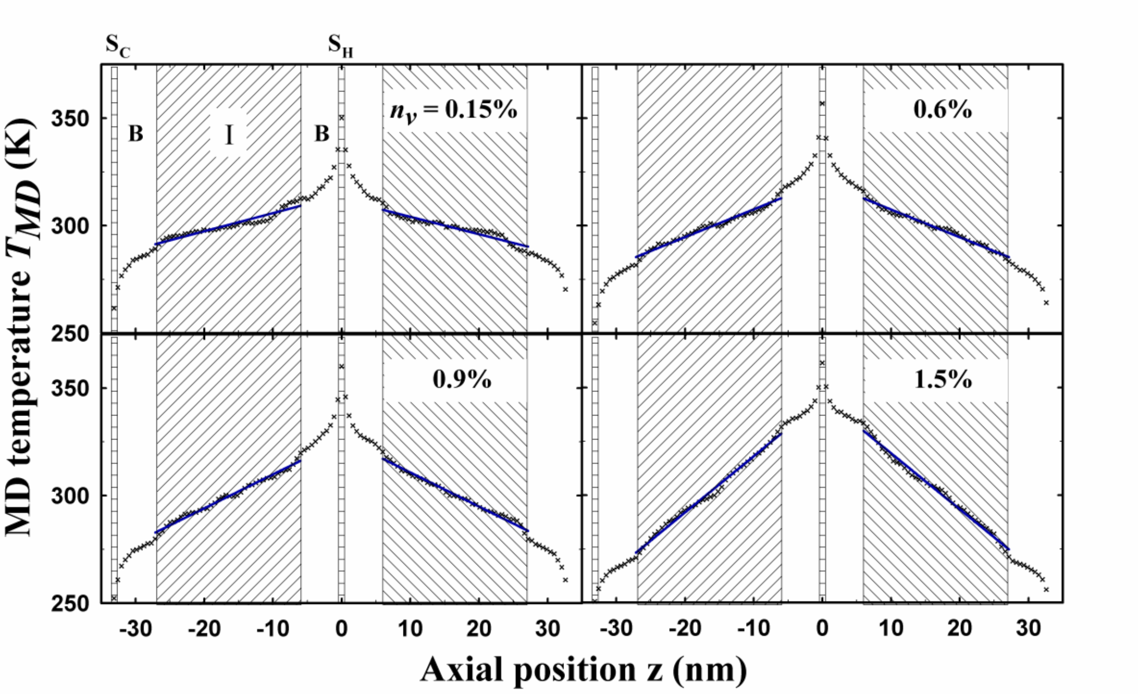

Figure 3.4: MD temperature (T_{MD}) profiles sampled from the V_{12}-embedded defective systems of four different vacancy concentrations, n_v = 0.15, 0.6, 0.9, and 1.5%. Data are from the simulation cell consisting of 10×10×122 units (corresponding to 3.8405×3.8405×65.1756 nm^3) and the sample temperature of 300K. All profiles exhibit linear temperature gradients in the intermediate layers (hatched), as represented by thin solid lines. S_H, S_C, B, and I indicate the heat source, heat sink, buffer, and intermediate layers, respectively.

Figure 3.5 shows predicted κ values as a function of vacancy concentration for V_4, V_6, and V_{12}. As n_v increases, κ rapidly decreases; the presence of 1.5% vacancies leads to a 95 % reduction in κ (13.20±0.33, 10.65±0.23, and 10.60±0.20 Wm^{-1}K^{-1} for the V_{12}, V_6, and V_4 cases, respectively), as compared to the defect free *c*-Si (235.71±7.53 Wm^{-1}K^{-1}). Even with n_v = 0.15%, phonon transport tends to be significantly impeded, as κ drops by over 60% (175.35±24.2, 98.99±8.17, and 87.42±9.84 Wm^{-1}K^{-1} for the V_{12}, V_6, and V_4 cases). Note that at n_v = 0.15% there are only two V_{12}, four V_6, or six V_4 clusters in the 10×10×40 simulation cell (16000 atoms). The large standard deviation of κ at low vacancy concentrations (especially when n_v = 0.15%) is due to the fact the heat transfer from the source to the sink is strongly affected by the location of vacancy clusters. As the number of clusters increases, the standard deviation decreases with a well-converged κ.

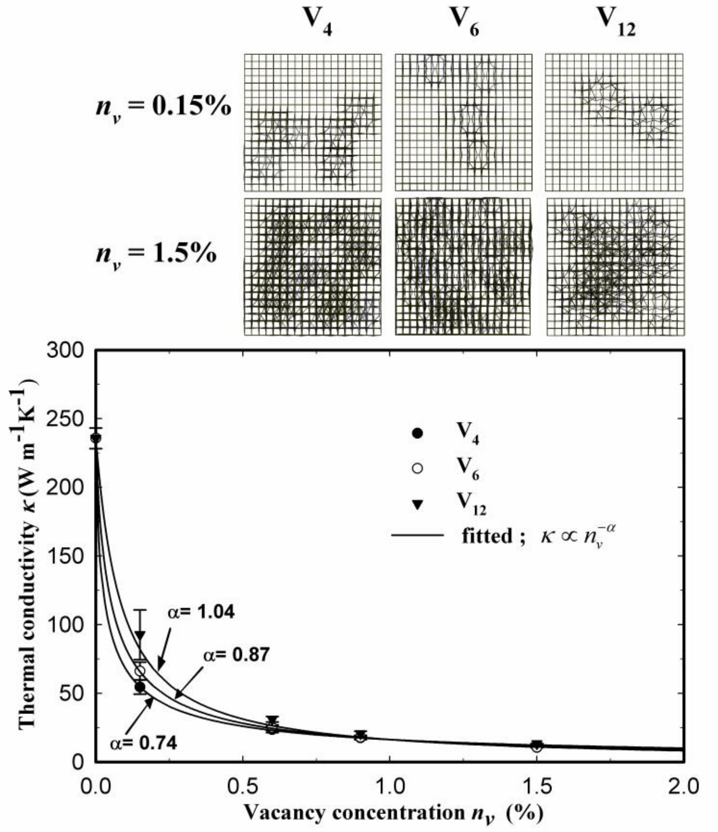

Figure 3.5: Calculated bulk thermal conductivities at 300K (with quantum correction) as a function of vacancy concentration for the V_4, V_6 and V_{12}-embedded Si systems. In the upper panels, selected cross-section wireframe views along the heat flow (or <100>) direction are also shown for two different vacancy concentrations.

Figure 3.5 also shows a non-linear decay of κ with n_v. The calculated values are well fitted with an inverse power law relation, $\kappa \propto n_v^{-\alpha}$, with α = 1.04, 0.87, and 0.74 respectively for the V_{12}, V_6, and V_4 cases. The nonlinear relation between κ and n_v has also been reported for carbon materials such as carbon nanotubes[63] and diamond[140]. The exponent α is a measure of how rapidly κ drops with increasing n_v; that is, a smaller exponent implies a steeper decrease of κ. According to our results, smaller clusters would more effectively inhibit phonon transport for the same vacancy concentration.

It is worth noting that the reduction of κ with n_v is a function of cluster size particularly when n_v is low. To understand the correlation between phonon scattering and cluster size, we approximated the rate of vacancy scattering in the vacancy-embedded region; here, the rate of phonon scattering due to vacancy aggregates is, according to previous studies[143,144], given by: $\tau^{-1} = cn\pi d_e^2/4$, where c is the phonon group velocity, n is the number density of vacancy clusters, and d_e is the effective diameter assuming the vacancy cluster is spherical. Suppose c is insignificantly affected by cluster size, the normalized scattering rate for V_6 or V_{12} with respect to V_4 can be approximated by: $\gamma_{V_N} = \tau_{V_N}^{-1}/\tau_{V_4}^{-1} = n_{V_N} d_{e,V_n}^2 / n_{V_4} d_{e,V_4}^2$ (N = 6 or 12). Here, the effective diameters were estimated based on defect-induced strain fields. For each vacancy cluster, we first counted the number of Si atoms that have strain energy higher than a given cutoff value, and then calculated the volume of a corresponding spherical compartment which can accommodate the strained Si and vacant atoms in the c-Si lattice. With the volume, the corresponding effective diameter was calculated by: $d_e = (6V/\pi)^{1/3}$.

For cutoff strain energies of 0.02-0.2 eV, the effective diameters are roughly estimated to be 13.35-7.72 Å, 15.02-8.14 Å, and 17.01-8.70 Å for V_4, V_6, and V_{12}, respectively. Taking the average values of the diameters (as the energy cutoff is rather arbitrary), γ_{V_6} and $\gamma_{V_{12}}$ are approximated to be 0.75 ± 0.05 and 0.59 ± 0.09, respectively, at $n_v = 0.15\%$. The increase of scattering rate with decreasing cluster size unequivocally supports our simulation results showing that the presence of smaller clusters leads to a more rapid reduction in κ for the same vacancy concentration. We admit that this approach would be oversimplified, but should be physically sound and sufficient for approximation of the scattering rate variation with cluster size, considering that phonon scattering is, to a large extent, determined by defect-induced lattice distortions. The cluster-size dependence of κ becomes insignificant as the density of vacancy clusters increases. When $n_v = 1.5$ %, κ is virtually no longer a function of cluster size. This is likely related to the fact that the projected areas of clusters in the heat flow direction largely overlap and nearly cover the heat flow cross-section, as illustrated in Fig. 3.4. Note that phonons travel in straight lines from the source to the sink; the transport of most of the phonons could be blocked if the cross-section is covered by vacancy clusters, and thus phonon transport becomes rather insensitive to the cluster size.

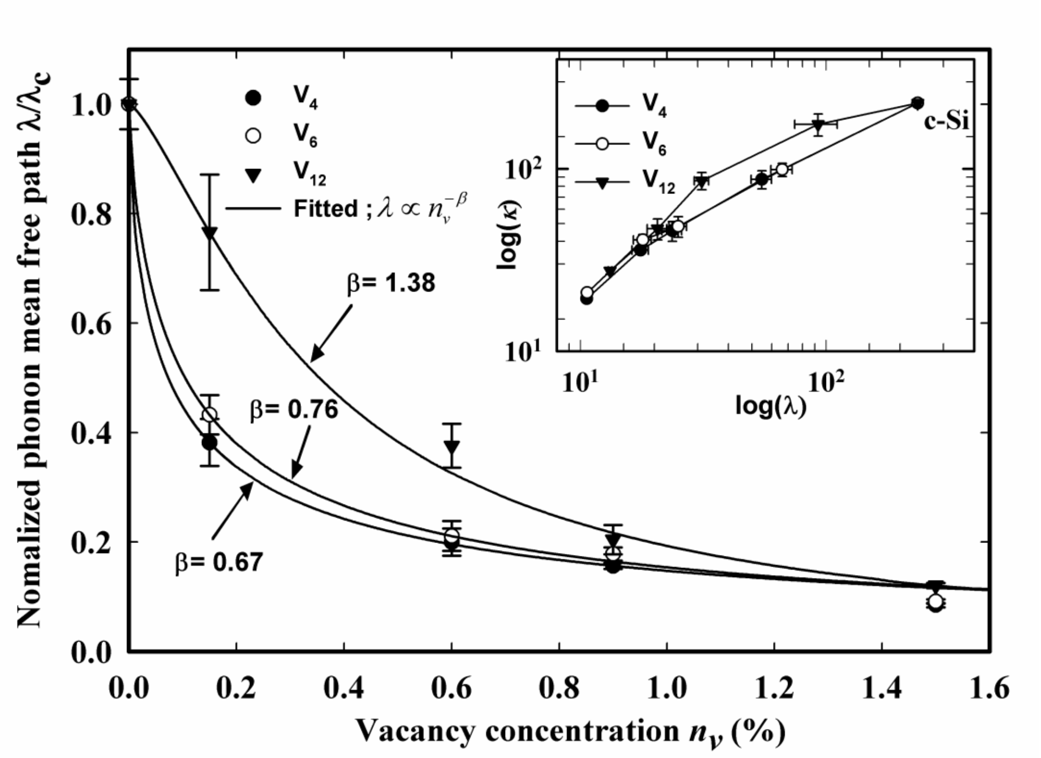

Figure 3.6: Calculated normalized phonon mean free paths at 300K as a function of vacancy concentration for the V_4, V_6 and V_{12}-embedded Si systems. Inset shows a correlation between thermal conductivity and phonon mean free path; both κ and l rapidly decrease with n_v.

Finally, we estimated how the phonon mean free path is affected by vacancy concentration and cluster size. Figure 3.6 shows the normalized phonon mean free paths for various vacancy-embedded systems with respect to the bulk value ($\lambda = l/l_{c\text{-}Si}$). The normalized mean free paths rapidly decrease with n_v; at $n_v = 1.5$ % the predicted values are 0.1202±0.0046, 0.0913±0.0039, and 0.0846±0.0038 for the V_{12}, V_6, and V_4 cases, respectively. Similar to the variation of κ (see Fig. 3.5), the results are also well fitted to an inverse power law relation, $l \propto n_v^{-\beta}$, with β = 0.67, 0.76, and 1.38 for the V_4, V_6, and

V_{12} cases, respectively. In addition, the inset clearly shows that there is a direct correlation between κ and phonon mean free path, consistent with the kinetic theory ($\kappa \propto l$). In undoped (or lightly doped) semiconductors, heat is transported primarily by lattice vibrations (phonons) at moderate temperatures (where the effect of radiation is negligible).[45] Likewise, electronic and radiative contributions can be ignored in the c-Si system considered; therefore, the mean free path of phonons is an important indicator regarding how effectively thermal energy is carried through the model Si structures.

3.3. Mechanisms of Thermal Conductivity Suppression in Doped Si

In this work, we perform a quantitative analysis of the effects of dopants on phonon transport in *c*-Si, particularly the underlying mechanisms of phonon scattering due to different types of dopants including boron (B), aluminum (Al), phosphorous (P), and arsenic (As).

3.3.1 Force matching-based Stillinger-Weber (SW) Potential Parameter Optimization

For NEMD simulations, we employed a general form of SW potential function. The SW parameters were optimized for Si-X (X = B, P, As, or Al) systems using a force-matching method[71] based on DFT calculations of the restoring forces associated with atomic displacements. The DFT force data for the parameter optimization were obtained by displacing a dopant atom or its neighboring atoms in the *x*, *y*, and *z* directions by 0.08 Å. The restoring forces acting on the displaced atom and its four first-nearest neighbors were considered to be matched in the SW parameter adjustments. On the third-nearest neighbors and beyond, the forces due to the center-atom displacement turn out to be negligible (less than 0.01 eV/ Å in the absolute value). In this work, the force constants for the second-nearest Si neighbors and beyond were assumed to be the same as those for *c*-Si; although the second-nearest Si atoms have three-body interactions with the dopant atom (Si-Si-X), the contribution is likely to be insignificant.

Our DFT calculations were performed within the GGA-PW91[89], using the VASP[90]. We used Vanderbilt-type ultrasoft pseudopotentials[91] to represent the interaction between ion cores and valence electrons, and a planewave basis set with a kinetic energy cutoff of 250 eV. We used a 64-atom cubic supercell that contains one dopant atom and 63 Si atoms for optimizing Si-dopant interaction potentials. A (2×2×2) *k*-point grid in the scheme of Monkhorst-Pack was used for the Brillouin zone sampling.

Table 3.1 summarizes the modified parameters from the force matching approach; the σ values were chosen to match the Si-X bond distances (X = B, Al, P, As) from DFT-GGA calculations. In addition, the equilibrium Si-Si-X bond angles (θ_0) were obtained from DFT-GGA calculations, while the equilibrium Si-Si-Si and Si-X-Si bond angles were set at 109.47° (tetrahedral bond angle). Figure 3.7 shows the comparisons of the restoring forces from our SW and DFT-GGA calculations; overall, the modified SW parameters provide excellent reproduction of corresponding DFT forces (acting on the center dopant atoms and their Si neighbors).

Table 3.1: Modified parameters of the Stillinger-Weber interatomic potential for Si-X interactions (X = B, P, As, and As); σ, ε, λ, *a*, and cosθ_o values were optimized based on DFT-GGA calculations of local lattice structure and restoring forces arising from local lattice distortions.

	Si-B	**Si-P**	**Si-Al**	**Si-As**
σ	1.8675	2.0994	2.1483	2.1702
ε (eV)	1.2496	1.0235	1.4858	1.0772
λ	33.8815	64.3998	17.5472	49.9274
a	1.6452	1.8003	1.8379	1.8688
cosθ_0	-0.4195	-0.3298	-0.3251	-0.3036

$A = 7.049556277$, $B = 0.6022245584$,

$p = 4.0$, $q = 0.0$, and $\gamma = 1.2$.

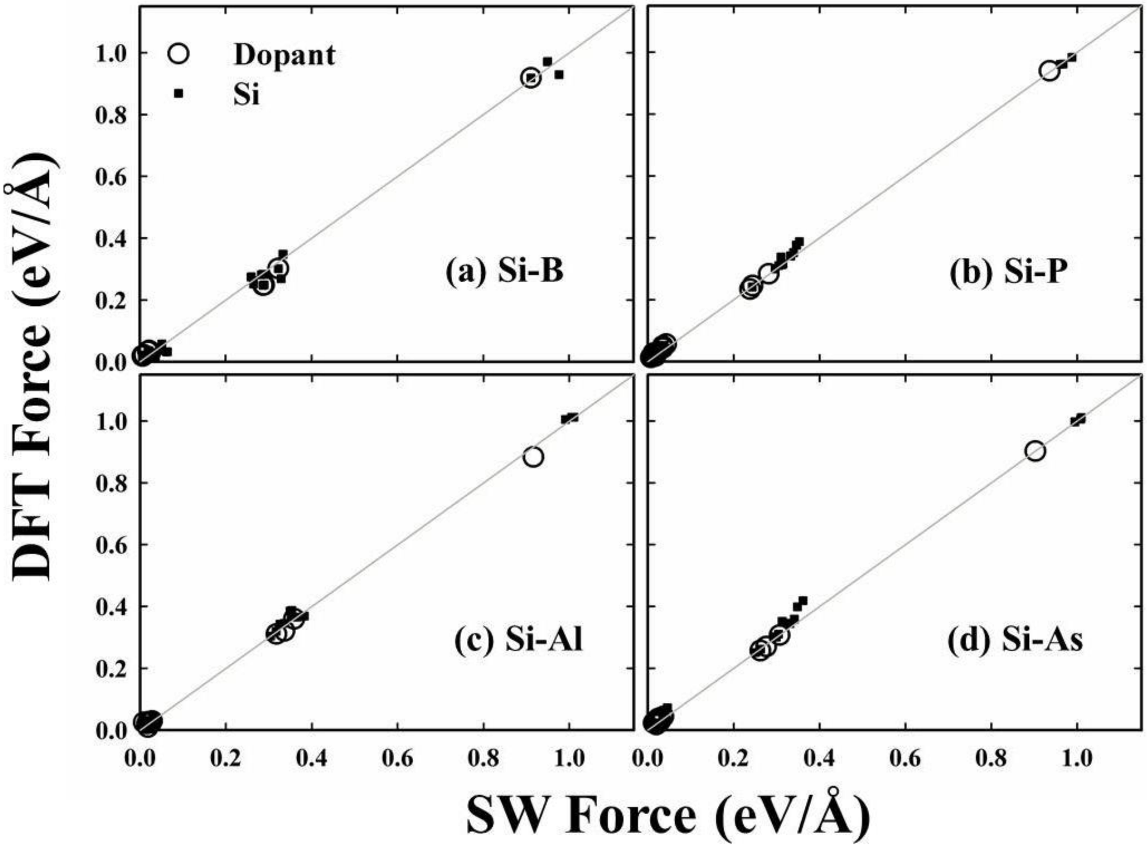

Figure 3.7: Comparison between predicted DFT and Stillinger-Weber (SW) forces acting on the displaced dopant atom and its four first-nearest Si atoms for four different doped systems as indicated.

3.3.2. Validity of Re-optimized SW Potential for Predicting Thermal Conductivity of Doped Si

To assess the reliability of the SW interatomic potential with modified parameters, we compared calculated κ values with existing experimental data for bulk *c*-Si doped with B at various doping concentrations. For NEMD simulations, we used a composite cell scheme employed in chapter 3.2. Dopant atoms were assumed to remain isolated without making any pairs or larger clusters, and they were placed in a random manner in the simulation domain; the dopant concentrations in the S_H/S_C, B and I layers were controlled to be (nearly) equal.

Figure 3.8 shows predicted κ values for B-doped bulk *c*-Si at B concentrations of n_B = 1.21875, 2.4375, 4.875, and 7.3125×10^{20} atoms/cm^3 (corresponding to the atomic percentages of x_B = 0.25, 0.5, 1, and 1.5 at.%, respectively). For comparison, the experimental data available from the published literature are also plotted. Note that each bulk κ value was obtained through extrapolation of finite-size results to infinite size, as shown in the inset (here, $L_z = ½ L_{tot}$); refers to Ref. 20 for a more detailed description of the computational technique. For a given simulation-cell-size and dopant-concentration system, we performed twenty-five (25) independent NEMD simulations considering five (5) different atomic-level spatial distributions of dopants, for each of which five (5) different initial velocity distributions were also taken into account. In this work, doped Si systems considered were assumed to have the same T_D as Si (= 645 K[85]), as the atomic fractions of dopants are very small (< 0.01); note that the Debye temperature of an alloy system ($A_{1-x}B_x$) is typically approximated by the linear relation $T_D(AB) = (1-x)T_D(A) + xT_D(B)$ [145] .

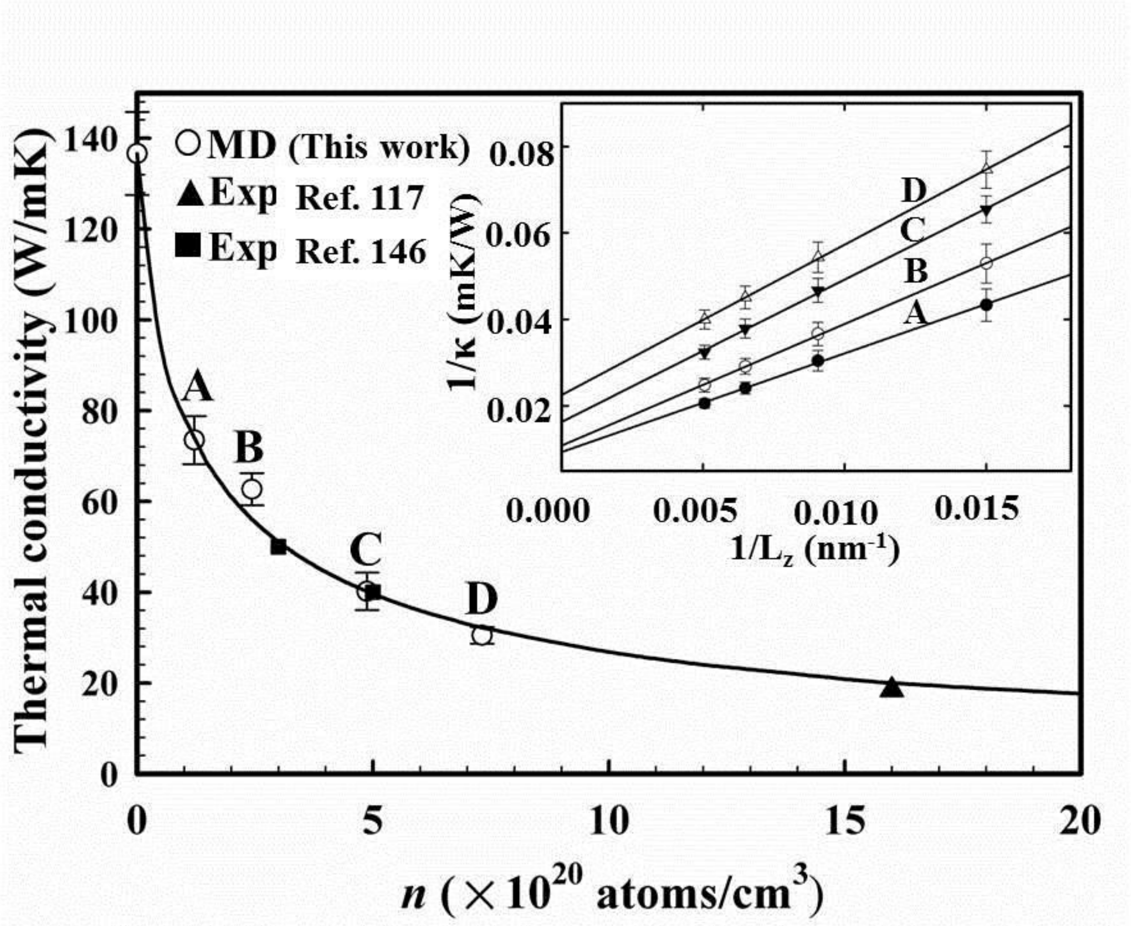

Figure 3.8: Comparison Calculated bulk thermal conductivities of B-doped Si at 300K as a function of dopant concentration (n_B), together with available experimental data for comparison. The solid line indicates a fitted curve to the simulation result, which is $\kappa = \kappa_{Si} / \left[1 + A\left(\frac{n_B}{10^{20}}\right)^{\alpha} \right]$ with A = 0.74186, α = 0.7411, and κ_{Si} = 136.65 $\mathrm{Wm^{-1}K^{-1}}$. The inset shows thermal resistivity ($1/\kappa$, after quantum corrections) for B-doped Si at different doping concentrations as specified; for each set the linear line indicates the best-fit linear regression. Here, L_z is the distance between the heat source and heat sink centers, which is half of the total simulation cell length.

The calculated κ values (after quantum corrections) are well fitted by $\kappa = \kappa_{Si} / \left(1 + A\bar{n}_B^{\alpha}\right)$ with A = 0.74186 and α = 0.7411, where κ_{Si} is the thermal conductivity of undoped *c*-Si (= 136.65 $\mathrm{Wm^{-1}K^{-1}}$), and $\bar{n}_B$ is the dimensionless B concentration (= $n_B/10^{20}\mathrm{cm^{-3}}$); the inverse power-law relationship has been widely adopted to describe the effect of point-like impurities (or defects) on lattice κ [63,65,66,140]. We can see that the predicted value of 39.27 ± 5.54 $\mathrm{Wm^{-1}K^{-1}}$ (at n_B = 4.875×10^{20} /cm^3) is very close to the experimentally reported value of 40 $\mathrm{Wm^{-1}K^{-1}}$ (at $n_B \approx 5\times10^{20}$/cm^3)[146]. In addition, the fitted relation shows good agreement with the experiment data of about 50 $\mathrm{Wm^{-1}K^{-1}}$ at $n = 3\times10^{20}$ /cm^3 and 18.5 $\mathrm{Wm^{-1}K^{-1}}$ at $n = 1.6\times10^{21}$ /cm^3. The excellent agreement between the simulation and experiment results increases our confidence in the validity of the modified SW parameters for use of estimating the lattice κ of doped *c*-Si at moderate temperatures.

3.3.3 Relative Effectiveness of B, Al, P, and As in Thermal Conductivity Suppression

Using the same NEMD approach as described in the previous section, we examined how different substitutional dopants (B, Al, P, and As) affect the κ of *c*-Si. Since our intention was to compare the impurity scattering strengths among those doped systems, here we considered only a doping concentration of $n = 4.875 \times 10^{20}$/cm^3. For different doped systems, dopants were placed at the same sites to avoid any possible unwanted effect associated with the disparity between their spatial distributions. Compared to the undoped case (κ_{Si} = 136.65 ± 9.15 W/mK), the introduction of Al, P, B, and As dopants leads to a considerable reduction in κ; as summarized in Fig. 3.9, the calculated ordering is κ_{SiAl}(total) = 78.18 ± 6.85 > κ_{SiP}(total) = 56.73 ± 5.21 > κ_{SiB}(total) = 39.27 ± 5.54 > κ_{SiAs}(total) = 18.32 ± 2.17 W/mK. Our simulations clearly demonstrate that As and B doping can more effectively suppress thermal transport in *c*-Si compared to P and Al. Overall, the simulation results are consistent with existing experimental observations. For instance, according to Liu *et al.*[117], κ_{SiP} appears to be about twice larger than κ_{SiAs} when $n = 2.3\times10^{20}/\text{cm}^3$; in addition, Asheghi *et al.*[129] demonstrated that B doping tends to cause a greater suppression of κ than P doping.

3.3.4 Relative Contributions of Mass Disorder, Bond Disorder, and Lattice Strain for Each Dopant

Phonon scattering by substitutional dopants can be attributed to the atomic mass and/or atomic radius differences between the host and dopant atoms; the mass and radius disparities are respectively related to the so-called ‘mass disorder’ and ‘lattice strain’ effects. In addition, the existence of the heterobonds between dissimilar (host and dopant) atoms may cause phonon scattering (the so-called ‘bond disorder’ effect). Next, we discuss the relative contributions of mass disorder, bond disorder, and lattice strain to the κ suppression in each doped system.

Mass disorder effect. — The effect of mass disorder was examined by assuming that dopant atoms have the same radius and force constants as Si (see Table 3.1), but they have their own masses ($m_B = 10.81$, $m_{Al} = 26.98$, $m_P = 30.97$, $m_{As} = 74.92$, $m_{Si} = 28.08$); that is, the contributions of bond disorder and lattice strain were excluded. Here, dopant atoms were located at the same sites in the simulation cell as described in the previous section.

As summarized in Fig. 3.9, the κ suppression is more enhanced with increasing the ratio of mass difference ($\Lambda = |m_{Si}-m_x|/m_{Si}$, x = B, Al, P, As); the order from lowest to highest is as follows, κ_{SiAl}(mass) = 123.61 ± 8.97 $Wm^{-1}K^{-1}$ (Λ = 0.039) < κ_{SiP}(mass) = 83.13 ± 7.28 $Wm^{-1}K^{-1}$ (Λ = 0.103) < κ_{SiB}(mass) = 41.82 ± 4.98 $Wm^{-1}K^{-1}$ (Λ = 0.615) < κ_{SiAs}(mass) = 19.05 ± 1.98 $Wm^{-1}K^{-1}$ (Λ = 1.668). The simulation results well advocate the model suggested by Abeles for the alloy scattering strength (Γ) due to mass difference[147]; $\Gamma \propto \left[\frac{(1-x_i)M_i-(1-x_i)M_h}{x_iM_i+(1-x_i)M_h}\right]^2$, where x_i and M_i are the fractional concentration and the mass of the impurity atom, and M_h is the mass of the host atom; if $x_i \ll 1$, $\Gamma \propto \left(\frac{M_i-M_h}{M_h}\right)^2 = \Lambda^2$.

For As, κ_{SiAs}(mass) (= 19.05 $Wm^{-1}K^{-1}$) is very close to κ_{SiAs}(total) (=18.32 $Wm^{-1}K^{-1}$), indicating that the mass disorder effect is primarily responsible for κ suppression in the As-doped system. Likely, in the B-doped case where the mass difference is also significant, the extent of κ reduction [$\Delta\kappa_{SiB}$(mass) = $\kappa_{Si} - \kappa_{SiB}$(mass)] due to mass disorder is predicted to be 94.83 (= 136.65 − 41.82) $Wm^{-1}K^{-1}$, which is about 97 % of the total reduction of 97.38 ($\Delta\kappa_{SiB}$(total) = $\kappa_{Si} - \kappa_{SiB}$(total) = 136.65 − 39.27) $Wm^{-1}K^{-1}$. On the other hand, the mass disorder contribution appears to be relatively insignificant for the Al- and P-doped cases, only about 22 % and 67 %, respectively.

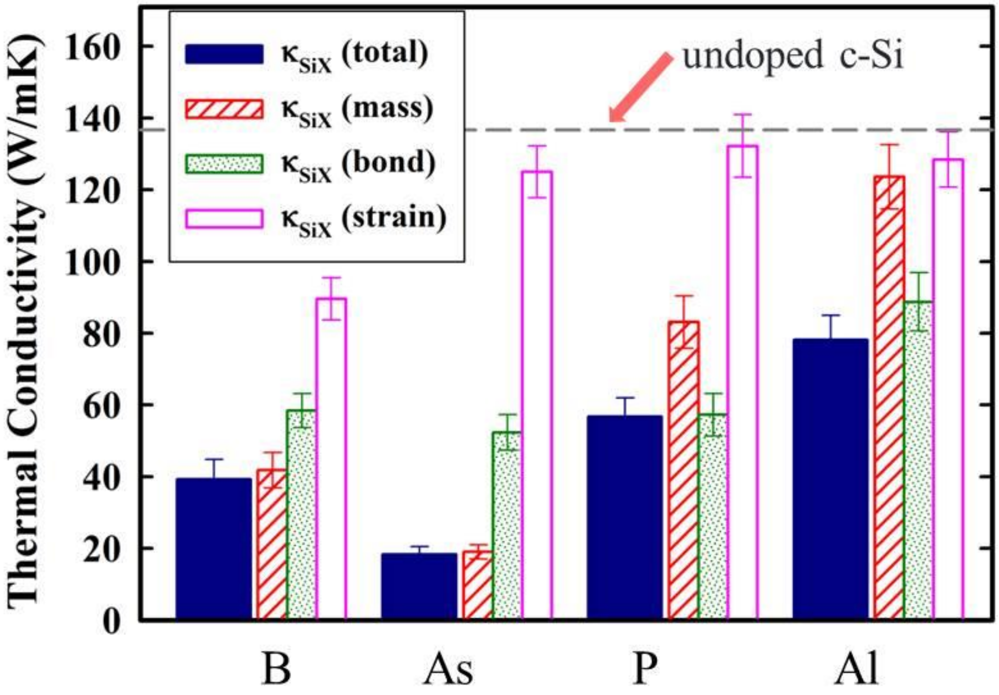

Figure 3.9: Calculated thermal conductivities (after quantum corrections) for bulk *c*-Si doped with B, As, P and Al at *T*= 300K and *n* = 4.875 × $10^{20}/\text{cm}^3$. The dashed horizontal line indicates the predicted κ value of undoped Si (= 136.65 $\text{Wm}^{-1}\text{K}^{-1}$). For each doped system, besides its bulk value [indicated as κ_{SiX}(total)], the κ values calculated by isolating each of the effects of mass disorder [κ_{SiX}(mass)], bond disorder [κ_{SiX}(bond)], and lattice strain [κ_{SiX}(strain)] are also plotted.

Bond disorder effect. — To look at the bond disorder effect, the masses and radii of dopant atoms were assumed to be the same as those of the host Si atom, while other force constants optimized for each doped system were used (see Table 3.1). Our calculations show that the κ reduction due to bond disorder can be significant for all four doped systems, following the order of [κ_{SiAl}(bond) = 88.74 ± 8.13 > κ_{SiB}(bond) = 58.41 ± 4.74 > κ_{SiP}(bond) = 57.26 ± 5.88 > κ_{SiAs}(bond) = 52.31 ± 4.96 $Wm^{-1}K^{-1}$]. Interestingly, for the Al- and P-doped cases, the bond disorder effect is found to be more important than the mass disorder effect; that is, $\Delta\kappa_{SiAl}$(bond) [= $\kappa_{Si} - \kappa_{SiAl}$(bond) = 47.91 $Wm^{-1}K^{-1}$] and $\Delta\kappa_{SiP}$(bond) [= $\kappa_{Si} - \kappa_{SiP}$(bond) = 79.39 $Wm^{-1}K^{-1}$] are about 82 % and 99 % of $\Delta\kappa_{SiAl}$(total) (= 58.47 $Wm^{-1}K^{-1}$) and $\Delta\kappa_{SiP}$(total) (= 79.92 $Wm^{-1}K^{-1}$), respectively.

In the three-body SW potential, the inter-atomic forces can be decoupled into two-body (*F*) and three-body (*G*) contributions; that is, $F \propto \frac{\varepsilon}{\sigma^2}$ and $G \propto \frac{\varepsilon\lambda}{\sigma^2}$, where σ, ε, and λ are SW parameters. Looking at the two-body and three-body force components associated with dopant atoms, relative to the host Si lattice, we can notice that only the two-body contribution tends to be important for Al [γ_F(Al) = 1.005 and γ_G(Al) = 0.597], whereas both two-body and three-body force disturbances play a comparably important role in causing phonon scattering in the B-, P-, and As-doped cases [γ_F(B) = 1.118, γ_G(B) = 1.283; γ_F(P) = 0.725, γ_G(P) = 1.581; γ_F(As) = 0.713, γ_G(As) = 1.207].

Lattice strain effect. — We looked at the lattice strain effect by assuming that dopant atoms have the same mass and force constants as Si, except $\theta_{Si\text{-}Si\text{-}X}$ and $\sigma_{Si\text{-}X}$ (x = dopant). As summarized in Fig. 3.9, our calculations suggest that the doping-induced strain may play a minor role in suppressing the lattice κ, particularly in the P- and As-doped systems (whose κ values are lower only by 3 % and 9 %, respectively, compared to the undoped Si reference). This is not surprising considering there is no significant dopant-induced local lattice distortion; note the small difference of length unit parameter between Si-dopant ($\sigma_{\text{Si-P}}$ = 2.0994, $\sigma_{\text{Si-As}}$ = 2.1702) and Si-Si ($\sigma_{\text{Si-Si}}$ = 2.1052, from our DFT-GGA calculations), and also that the bend angles of $\theta_{\text{Si-Si-P}}$ (= 109.3˚) and $\theta_{\text{Si-Si-As}}$ (= 107.6˚) are close to $\theta_{\text{Si-Si-Si}}$ (= 109.5˚). Compared to Al, P and As, B causes relatively more lattice distortions ($\theta_{\text{Si-Si-B}}$ = 114.8˚) because of its smaller radius ($\sigma_{\text{Si-B}}$ = 1.8675) and thus leads to a larger strain effect; nonetheless, the contribution of lattice strain turns out to be far smaller than those of mass disorder and bond disorder.

3.4 Effect of Dopant Agglomeration in Arsenic Doped Silicon

3.4.1 Force Field Optimization for Si-As Interactions

For NEMD simulations, we employed a general form of SW potential function. The SW parameters for Si-As interactions of As_4V-doped Si were optimized using a force-matching method[71]. Fig. 3.10 shows a schematic view of As_4V complex fully relaxed using the DFT, with important geometric information. Using a 63-atom cubic supercell (one As_4V complex + 59 Si atoms), the DFT force data for the parameter optimization were obtained by displacing As atoms or its neighboring Si atoms in the *x*, *y*, and *z* directions by 0.08 Å. The restoring forces acting on the displaced atom and its first-nearest neighbors were considered to be matched in the SW parameter adjustments.

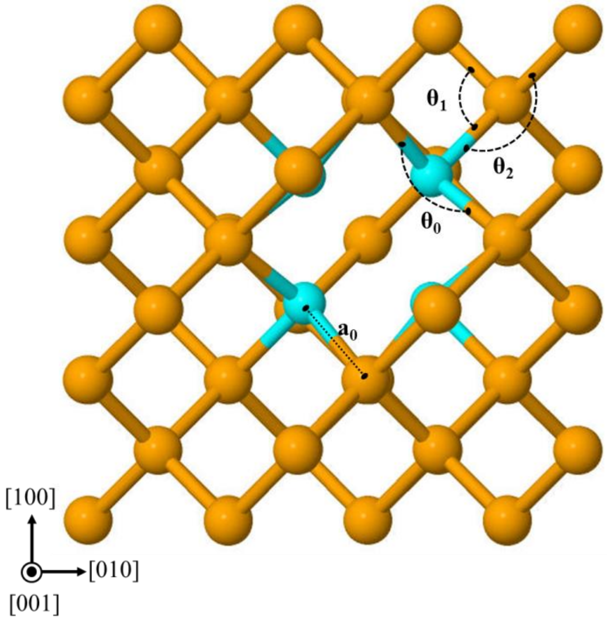

Figure 3.10: A schematic view of As_4V complex embedded in Si matrix; Si atom(orange) and As atom (cyan); a_0 = 2.4359 Å, θ_0 = 103.509°, θ_1 = 106.469°, and θ_2 = 115.728°.

Table 3.2 summarizes the modified parameters for As_4V complex from the force matching approach. The σ value was chosen to match the Si-As bond distances from DFT-GGA calculations. In addition, the equilibrium Si-As-Si bond angles (θ_0) were obtained from DFT-GGA calculations. For substitutional As dopant, Si-Si-As bond angles retained as 109.47° (= bond angle for Si diamond structure). However, the formation of As_4V complex introduces significant lattice distortions to neighboring Si atoms. To take into account this, two equilibrium Si-Si-As bond angles (106.469° and 115.728°) from DFT calculations were employed. Fig. 3.11 shows the comparisons of the restoring forces from our SW and DFT- GGA calculations; overall, the modified SW parameters provide excellent reproduction of the corresponding DFT forces (acting on As atoms and their Si neighbors) for the As_4V doped system.

Table 3.2: Modified parameters of the Stillinger-Weber interatomic potential for Si-As interactions for As_4V; σ, ε, λ, a, and $\cos\theta_o$ values were optimized based on DFT-GGA calculations of local lattice structure and restoring forces arising from local lattice distortions.

	Si-As		
σ	2.1702		
ε (eV)	1.2451		
λ	39.4445		
a	1.7717		
	Si-As-Si	As-Si-Si	
$\cos\theta_0$	-0.2337	-0.2835	-0.4340
A = 7.049556277, B = 0.6022245584, p = 4.0, q = 0.0, and γ = 1.0.			

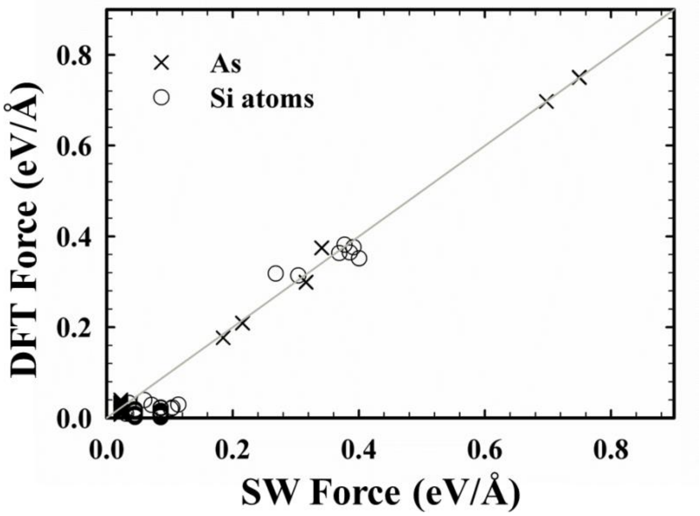

Figure 3.11: Comparison between DFT and Stillinger-Weber (SW) forces acting on the displaced As atom and its first-nearest Si atoms for As_4V doped systems. Solid line indicates |SW Force - DFT Force| = 0.

3.4.2 Thermal Conductivity Suppression in As_4V Doped Si

Using NEMD with the SW potential model, the thermal conductivities of As_4V-doped Si systems were calculated at various doping concentrations at 300K. To compare the impurity scattering strengths between substitutional As-doped and As_4V-doped Si, the κ values for point As-doped bulk *c*-Si were calculated at corresponding concentrations. For the interactions of substitutional As and Si, we adopted parameter set from our previous work [148]. For NEMD simulations, we employed the composite cell scheme (see section 3.2). As_4V complexes were assumed to remain isolated without making any overlaps among themselves, and they were placed in a random manner in the simulation domain; the dopant concentrations in the S_H/S_C, B and I layers were controlled to be (nearly) equal. Each bulk κ value was obtained through extrapolation of finite-size results to infinite size. For a given simulation-cell-size and dopant-concentration system, we performed twenty-five (25) independent NEMD simulations considering five (5) different atomic-level spatial distributions of dopants, for each of which five (5) different initial velocity distributions were also taken into account. For quantum correction, doped Si systems considered were assumed to have the same T_D as Si where T_D(Si) = 645 K [85], as the atomic fractions of dopants are very small (< 0.015).

Fig. 3.12 shows predicted bulk κ values for As_4V-doped *c*-Si and As-doped *c*-Si at *As* concentrations of n_{As} = 1.21875, 2.4375, 4.875, and 7.3125×10^{20} atoms/cm^3 (the atomic percentages of x_{As} = 0.25, 0.5, 1, and 1.5 at.%, respectively). For As doped-Si, the calculated κ values (after quantum corrections) are well fitted by $\kappa = \kappa_{Si} / \left(1 + A\bar{n}_{As}^{\alpha}\right)$ with A = 1.3496 and α = 0.9381, where κ_{Si} is the thermal conductivity of undoped *c*-Si (=136.65 $Wm^{-1}K^{-1}$) at 300K from our previous work[71], and $\bar{n}_{As}$ is the dimensionless As concentration (= $n_{As}/10^{20}cm^{-3}$); the inverse power-law relationship has been widely adopted to describe the effect of point-like impurities (or defects) on lattice κ [63,65,140,149]. The fitted relation shows good agreement with the experimental values [116] of about 107.4 $Wm^{-1}K^{-1}$ at $n = 0.17\times10^{20}$ /cm^3 and previous predictions [150] based on experimental data of As-doped Si films. Interestingly, compared to the point As-doped case, the introduction of As_4V complexes leads to a considerably larger reduction in κ; as shown in Fig. 3.12, at n_{As} = 4.875×10^{20} atoms/cm^3, κ (As) = 19.619 ± 2.547 > κ (As_4V) = 10.279 ± 1.782 $Wm^{-1}K^{-1}$. Fitting of $\kappa = \kappa_{Si} / \left(1 + A\bar{n}_{As}^{\alpha}\right)$ to the calculated κ values (after quantum corrections) gives A = 2.106 and α = 1.044. The exponent α is a measure of how rapidly κ drops with increasing n; that is, a larger exponent for As_4V complex implies a steeper decrease of κ. According to our results, As_4V complex can more effectively suppress thermal transport in *c*-Si compared to the point As-doped case.

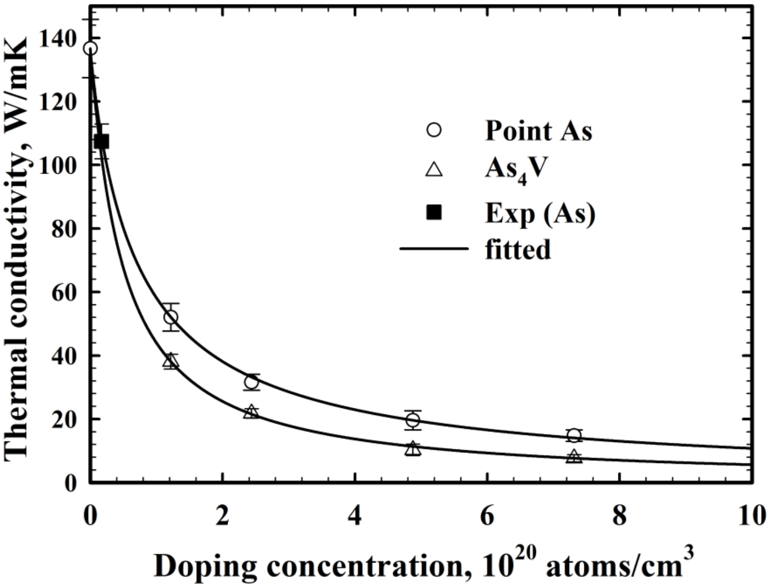

Figure 3.12: Calculated bulk thermal conductivities of As_4V- or As- doped Si at 300K as a function of dopant concentration (n_{As}), together with available experimental data of As- doped Si for comparison. The solid line indicates a fitted curve to the simulation result, which is $\kappa = \kappa_{Si} / \left[1 + A \left(\frac{n_{As}}{10^{20}} \right)^{\alpha} \right]$ with κ_{Si} = 136.65 $Wm^{-1}K^{-1}$. Thermal conductivities of As_4V-doped Si are clearly lower than those of As-doped Si.

3.4.3 Origin of Difference in Thermal Conductivity Suppression between As- and As_4V-Doped Si

As proposed in our previous study [148], phonon scatterings by substitutional dopants can be attributed to the 'mass difference', 'atomic radius disparity', and ‘heterobond formation’ between the host and dopant atoms. Similarly, the phonon scattering by agglomerated As dopants can be attributed to the presence of atomic mass differences and/or heterobonds; the mass and bond disparities are respectively related to the so-called ‘mass disorder’ and ‘bond disorder’ effects. In addition, the ‘lattice disorder’ effect can be defined as the combination of the atomic radius differences between dissimilar (host and dopant) atoms and the existence of the vacancy.

In order to understand the origin of the differences in κ suppression between substitutional and agglomerated As dopants, we investigated the relative contributions of three factors in κ suppression in As- and As_4V-doped Si, and their differences.

First, the effect of mass disorder was examined by assuming that dopant atoms have the same radius and force constants as Si, but they have their own masses (m_{As} = 74.92 and m_{Si} = 28.08). In order to exclude the lattice disorder effect in As-doped Si, vacancies in As_4V were replaced with Si atoms, which makes 5 atom-clusters (As_4Si) consisting of one Si surrounded by four As atoms. Our calculations show that the κ reduction due to mass disorder is significant for both cases; the extent of κ reduction due to mass disorder is predicted to be [$\Delta\kappa_{As}(\text{mass}) = \kappa_{Si} - \kappa_{As}(\text{mass}) = 117.031\ Wm^{-1}K^{-1}$] or [$\Delta\kappa_{As4V}(\text{mass}) = \kappa_{Si} - \kappa_{As4V}(\text{mass}) = 115.456\ Wm^{-1}K^{-1}$] for As- or As_4V- doped Si, respectively. It turns out that the mass disorder is more effective in reducing κ in As-doped Si than As_4V-doped Si, because the uniform distribution of scattering centers is more effective in reducing κ than the agglomerated case. However, the difference is not significant because all As atoms in As_4V are paired with neighboring Si atoms, therefore, they work as active scattering centers due to mass disorder.

Next, to look at the bond disorder effect, the masses and radii of dopant atoms were assumed to be the same as those of the host Si atom, while other force constants optimized for each doped system were used. Here, we used the model structures having As_4Si clusters for the As_4V doped case, again. Our calculations show that the κ reduction due to bond disorder can be significant for both doped systems, following the order of [$\kappa_{As}(\text{bond}) = 84.34 \pm 8.13 > \kappa_{As4V}(\text{bond}) = 78.54 \pm 6.48$]. Our calculation indicates that the bond disorder effect is more significant in the As-doped case than the As_4V-doped case. In the SW potential, the inter-atomic forces can be decoupled into two-body (*F*) and three-body (*G*) contributions; that is, $F \propto \frac{\varepsilon}{\sigma^2}$ and $G \propto \frac{\varepsilon\lambda}{\sigma^2}$, where σ, ε, and λ are SW parameters. Looking at the two-body and three-body force components associated with dopant atoms, relative to the host Si lattice, $\gamma_F(As_4V) = 0.824$ and $\gamma_G(As_4V) = 1.102$. It is noteworthy that both the two- and three-body disturbance tends to be smaller, compared to substitutional As; $\gamma_F(As) = 0.713$ and$\gamma_G(As) = 1.207$, due to the loss of coordination in As_4V, which was similarly observed in previous theoretical work [151].

Lastly, we looked at the lattice disorder effect by assuming that dopant atoms have the same mass and force constants as Si, except $\theta_{Si\text{-}Si\text{-}X}$ and $\sigma_{Si\text{-}X}$ (x = dopant). For the As_4V doped case, the lattice disorder due to the existence of vacancies is also included. While the doping-induced strain may play a minor role in suppressing the lattice κ in the As-doped systems (whose κ value is lower only by 9 %, respectively, compared to the undoped Si reference), the contribution of lattice disorder turns out to be significant in As_4V-doped case; $\Delta\kappa_{As4V}(\text{lattice}) = \kappa_{Si} - \kappa_{As4V} = 97.01\ Wm^{-1}K^{-1}$.

These results demonstrate that the significant difference in the lattice disorder effect between the As- and As_4V-doped cases might be a major factor for the further decrease in the κ of As_4V doped Si.

To better understand these results, we examined transmission characteristics of phonons in As- and As_4V-doped Si using the nonequilibrium Green's function (NEGF) approach [152-155]. Here, we ignored nonlinear phonon-phonon scatterings, as our primary concern was to understand the dependence of defect scattering on the local dopant structures. Considering only elastic scattering events, the ballistic thermal conductance (σ) at a given temperature can be expressed by the Landau formula[152-155]; $\sigma = \frac{1}{2\pi}\int_0^\infty d\omega\hbar\omega T(\omega)\frac{\partial f}{\partial T}$, where f is the Bose distribution for phonons. Based on the Caroli formula, the frequency-dependent phonon transmission coefficient is given by $T_{ph}(\omega) = Tr(G^r\Gamma_L G^a\Gamma_R)$, where G^r (G^a) represents the retarded (advanced) Green's function of the central scattering region and Γ_L (Γ_R) describes the interaction between the left (right) electrode and the central region. Here, the dynamic matrices for the G and Γ calculations were obtained from the second derivative of the SW potential energy surface with a displacement of 0.02 Å. Within the NEGF framework, as illustrated in Fig. 3.13, each calculation system consists of a central scattering alloy region and two semi-infinite Si leads; the axial lengths of the scattering region and each lead were set to 33.13 Å and 5.52 Å, respectively. The As or As_4V in the scattering region were randomly distributed with a doping level of $n_{As} = 4.875\times10^{20}$ /cm^3.

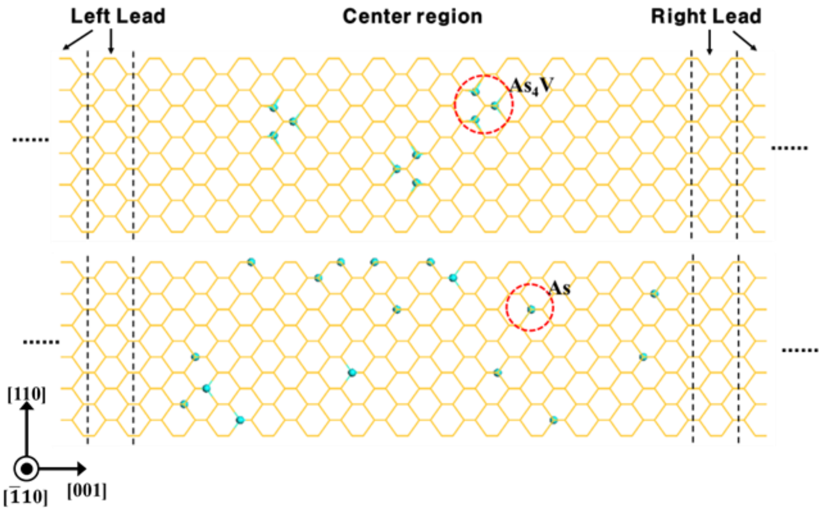

Figure 3.13: Simulation cells for non-equilibrium green's function (NEGF) method. The doping level in the center region is $n_{As} = 4.875\times10^{20}$ /cm^3.

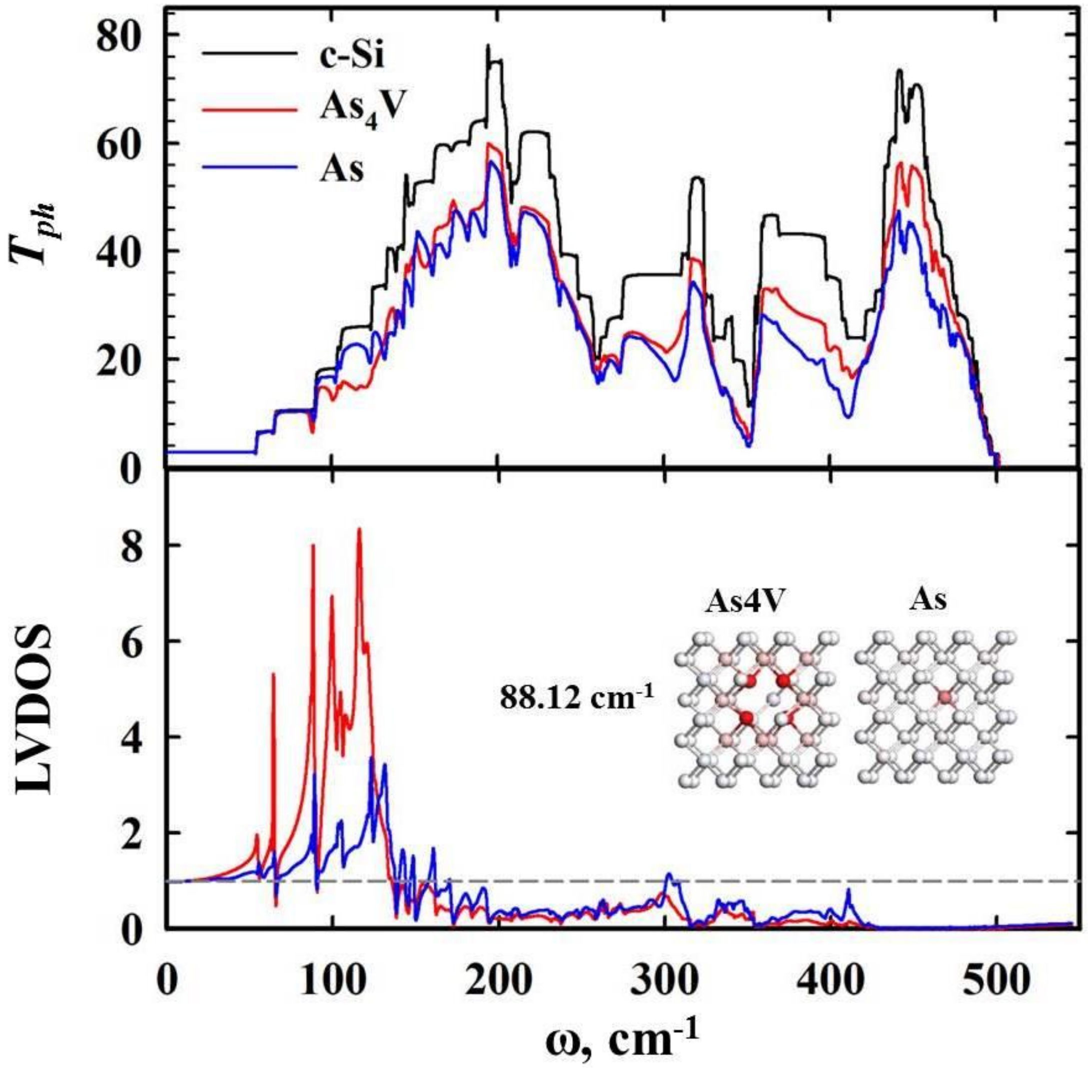

Figure 3.14: (TOP) Frequency-dependent phonon transmission coefficient (T_{ph}) calculated for As and As_4V doped Si, with comparison to the undoped Si case. (BOTTOM) Local vibrational densities of states (LVDOS) for As atoms; blue or red solid lines corresponds to As atoms in As_4V- or As-doped Si and grey dashed horizontal line indicates LVDOS = 1 which means all atoms have the same LVDOS. Atomistic views of LVDOS near As atoms are also shown at ω = 88.12 cm^{-1}. Red color on atom indicates high density.

The phonon transmission function ($T_{ph,As}$) for As-doped Si and $T_{ph,As4V}$ for As_4V-doped Si are described in Fig. 3.14. For the sake of reference, $T_{ph,Si}$ for undoped Si is also shown. For undoped Si, there are some regular steps, indicating that all phonons from the lead can pass through the center region without any scattering. On the other hand, $T_{ph,As}$ and $T_{ph,As4V}$ are dramatically deviated from $T_{ph,Si}$ owing to defect scattering. For both types of dopant, the channels for phonon transport are significantly reduced for most modes. $T_{ph,As}$ in the high frequency range are more reduced than $T_{ph,As4V}$. This may suggest that the case with evenly distributed scattering centers is more effective in reducing κ.

Interestingly, while $T_{ph,As}$ in the low frequency range below about 130 cm^{-1} remains unchanged or slightly changed, $T_{ph,As4V}$ is significantly reduced in the frequency range. Fig. 3.14 shows the normalized local vibrational density of states (LVDOS) for As atoms obtained using NEGF. At low frequencies where large suppression of phonon transmission for As_4V complex occurs, localization of eigenmodes on As atoms becomes more significant. A strong, spatially local resonant excitation in the region of defects (e.g. point defects and vacancies) at low frequencies was seen in previous studies [156,157]. Resonance scattering from a low-frequency local mode occurs by the scattering of phonons due to a localized lattice perturbation. There is the local disturbance due to large mass difference [Q(*Si-As*) = 2.67]. Moreover, the vacancy at the center of As_4V leads to an additional effect. As demonstrated in previous studies [158,159], the missing mass and linkages due to vacancies also intrigue the resonant scattering of phonons. Therefore, for

As_4V, resonance scatterings are intensified, and occur for lower frequency phonon modes.

3.4.4. Thermal Conductivity of SiGe Alloys Doped with As and As_4V

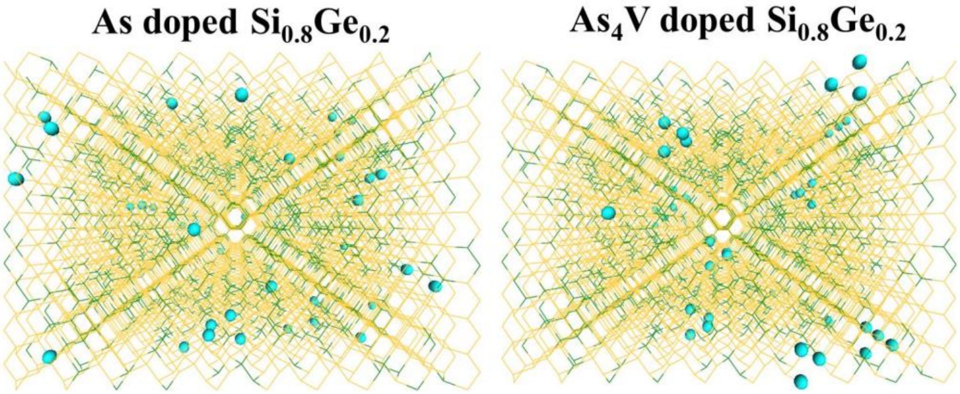

Figure 3.15: Schematic of As or As_4V doped SiGe alloys. Wire frame represents SiGe lattice (light gold = Si and green = Ge), and spheres represent As atoms.

We investigated the effect of As or As_4V doping on heat transport in SiGe alloys. For a doping level of $n_{As} = 4.875\times10^{20}$ atoms/cm^3, the thermal conductivities of $Si_{1-x}Ge_x$ were calculated at $x = 0.05$, 0.1, and 0.2. For both cases, As doping induced a further reduction in κ. Compared to the As-doped case, the introduction of As_4V complexes leads to a considerably larger reduction in the κ of $Si_{1-x}Ge_x$, as shown in Fig. 3.16. It is worth to note that at $x = 0.2$, the effect of As doping is negligible; the reduction of κ is only 3.65 %, compared to undoped $Si_{0.8}Ge_{0.2}$. This is because the doping-induced reduction of κ is mainly due to phonon scattering by the large mass difference between As and Si [148].

However, the mass-disorder effect is sufficiently saturated at $x = 0.2$ [35,57] by the mass differences between Si and Ge. Therefore, κ changes insignificantly with the 1 % additional introduction of As which has a quite similar mass to Ge. However, our calculations indicate that effect of As_4V is still significant regardless of the saturated mass scattering; the κ value is reduced by 16.34 %. This is because the As_4V induced reduction of κ is attributed to not only the mass disorder-induced scattering in the high frequency region, but also the suppression of low frequency modes due to the existence of Si vacancies.

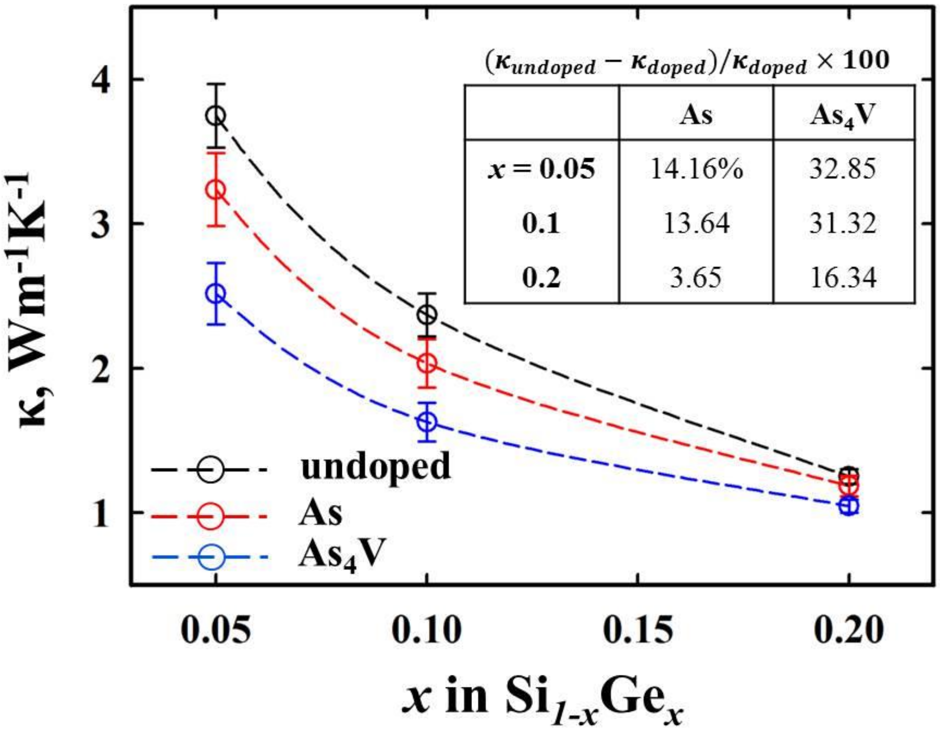

	As	As_4V
$x = 0.05$	14.16%	32.85
0.1	13.64	31.32
0.2	3.65	16.34

Figure 3.16: Calculated thermal conductivities (κ) for undoped, As, and As_4V doped $Si_{1-x}Ge_x$ as a function of composition ratio x. The inset summarizes the percentage reduction of κ in As- or As_4V doped $Si_{1-x}Ge_x$ compared to undoped cases for each composition ratio x.

Chapter 4 Alloying Effects on Heat Transport in Silicon-Germanium (SiGe) Alloys

4.1 Introduction

Since the 1960s, SiGe alloys have received much attention as one of the promising candidates for thermoelectric (TE) energy conversion[160]. It is now well accepted that the scattering of phonons due to the mass difference between Si and Ge is primarily responsible for the relatively high *ZT* of SiGe by suppressing κ, as compared to pure Si and Ge[57,147]. According to earlier experiments [161-164], the κ of undoped (or lightly doped) $Si_{1-x}Ge_x$ would be as low as 5-10 $Wm^{-1}K^{-1}$ at 300 K when $x = 0.2\text{-}0.3$, substantially less than 156.38 (60) $Wm^{-1}K^{-1}$ [84, 165] in Si (Ge).

In order to further reduce the κ of SiGe beyond the so-called alloy limit, several attempts [166-170] have been made by introducing extrinsic mechanisms of phonon scattering with point-like defects, chemical impurities, and/or grain boundaries. For instance, nanostructured *p*-type $Si_{0.8}Ge_{0.2}$[169-171] (produced by high-pressure sintering of nanopowders) exhibits very low κ (≈ 2-3 $Wm^{-1}K^{-1}$), resulting in a high *ZT* value approaching to 1 at 900-950 ^{o}C; the substantial reduction of κ has been thought be largely due to increased phonon scattering by nanograins. In addition, previous experimental work showed that the κ of alloys can be reduced by embedding nanoparticles[171-173], perhaps due to the interplay between alloy scattering and scattering by embedded nanoparticles. A recent MD study also predicted a drastic reduction in κ when Ge nanoparticles (with diameters of around 1.4-1.6 nm) were embedded in a crystalline Si matrix, as compared to the corresponding random SiGe alloy[174]. However, to better understand the role played by extrinsic mechanisms and effectively improve *ZT*, it is important to have a fundamental understanding about intrinsic alloy scattering mechanisms preferentially.

While various theoretical and computational methods have been employed to investigate heat transport in SiGe alloys [57,70,175], the large variation of predicted thermal conductivities depending on the method brings up the necessity to assess the liability of computational conditions; for example, predicted κ of $Si_{0.8}Ge_{0.2}$ is in the range of about 2 and 10 $Wm^{-1}K^{-1}$ at 300K. Besides other conditions, for successful theoretical and computational studies, model systems or simulation cells should represent the key features of real systems, in order to obtain right physics and fundamental understanding. Especially, in calculating the κ of disordered systems such as alloys, a unit cell size should be large enough to capture phonon-alloy scattering due to structural irregularity. Therefore, it is important to examine how large a unit cell should be, in order to correctly predict the κ of SiGe alloys.

While it has been well known that the strength of alloy scattering in a random alloy is determined by mass differences among constituent atoms and overall alloying compositions, a few previous experimental studies [132,176,177] have shown that a fraction of Si and Ge atoms may remain locally segregated in mechanically alloyed SiGe samples; that is, high-energy ball-milling of Si and Ge chunks may not always lead to a random distribution of Si and Ge atoms. A key question is whether alloy segregation may perhaps affect alloy scattering and subsequently alter noticeably κ.

Furthermore, group-IV (Si, Ge) semiconductor materials alloyed with Sn have received great attention for energy applications including photovoltaics and thermoelectrics, because of the possibility that the alloying of Sn with Si and Ge may allow for desirable structural, electronic, and thermal properties such as fully tunable band gaps [178-180] and ultra-low thermal conductivities.

In this chapter, we present a classical MD study of thermal transport in Si-based alloys. First, we present the dependence of predicted κ on the supercell size employed in MD simulations. The supercell size required to obtain a fully converged κ value is discussed. Next, we perform a classical MD study of thermal transport in bulk SiGe as a function of composition and microsegregation. Especially, we examine the effect of microsegregation by comparing the κ values of $Si_{0.8}Ge_{0.2}$ with and without Ge microsegregation, in order to address the effect of the distribution of alloying elements in determining the κ of alloys. Lastly, we investigate heat transport in ternary SiGeSn alloys using MD simulations with a newly optimized SW potential model. We discuss the possibility of lowering κ below the alloy limit of binary SiGe alloys.

4.2 Supercell Size Effect on Predicting Thermal Conductivity of SiGe

In order to investigate effects of size of repeating unit on calculation of κ of SiGe alloys, supecells at five different sizes were prepared with all <100> orientations for x, y, and z directions. The sizes of units (N in 2^{3N}) are varied from 1 (corresponding to 8 atoms), 2 (64 atoms), 3 (512 atoms), 4 (4096 atoms), to 5 (32768 atoms). Within each unit cell, Si and Ge atoms are randomly distributed at desired composition ratio. Investigated compositions are 12.5, 25, 50, 87.5 % Ge. One unit size along <100> is determined by Vagard's law; the lattice parameter of $Si_{1-x}Ge_x$ (a_{SiGe}) was approximated using linear interpolation between the Si and Ge lattice constants (from DFT-GGA calculations), i.e, $a_{SiGe} = (1–x)a_{Si} + xa_{Ge}$, where a_{Si} = 5.4571 Å and a_{Ge} = 5.7564 Å.

EMD using the LAMMPS code[76] was employed to calculate the κ values of SiGe alloys at 300K. For EMD simulations, we employed a general form of SW potential function with modified parameters using a force-matching method[35] based on DFT calculations. For κ calculations, simulation cells which are denoted here by $Si_{1-x}Ge_x(2^{3N})$ were prepared by expanding NxNxN supercell repeatedly to x, y, z directions, as shown in Fig 4.1. For all systems, the total size of simulation cell is set same to be 16x16x16 $unit^3$ (corresponding to 32768 atoms). This is for removing effects of simulation cell size on κ and clearly comparing effects by variation of size of repeating units among different samples, because EMD calculation has finite size effect when the simulation cell is not large enough. In simulations, the periodic boundary condition is applied in all three directions and each MD step is set as 0.5 fs. For κ calculations, first, canonical ensemble MD with Nose-Hoover thermostat for # steps to equilibrate the whole system at 300K. Then, microcanonical ensemble (NVE) MD runs for another 4×10^6 steps (2 ns). For quantum correction on MD results, the T_D for $Si_{1-x}Ge_x$ is approximated by $T_D(Si_{1-x}Ge_x) = (1–x)T_D(Si) + xT_D(Ge)$, where $T_D(Si)$ = 645 K and $T_D(Ge)$ = 374 K.

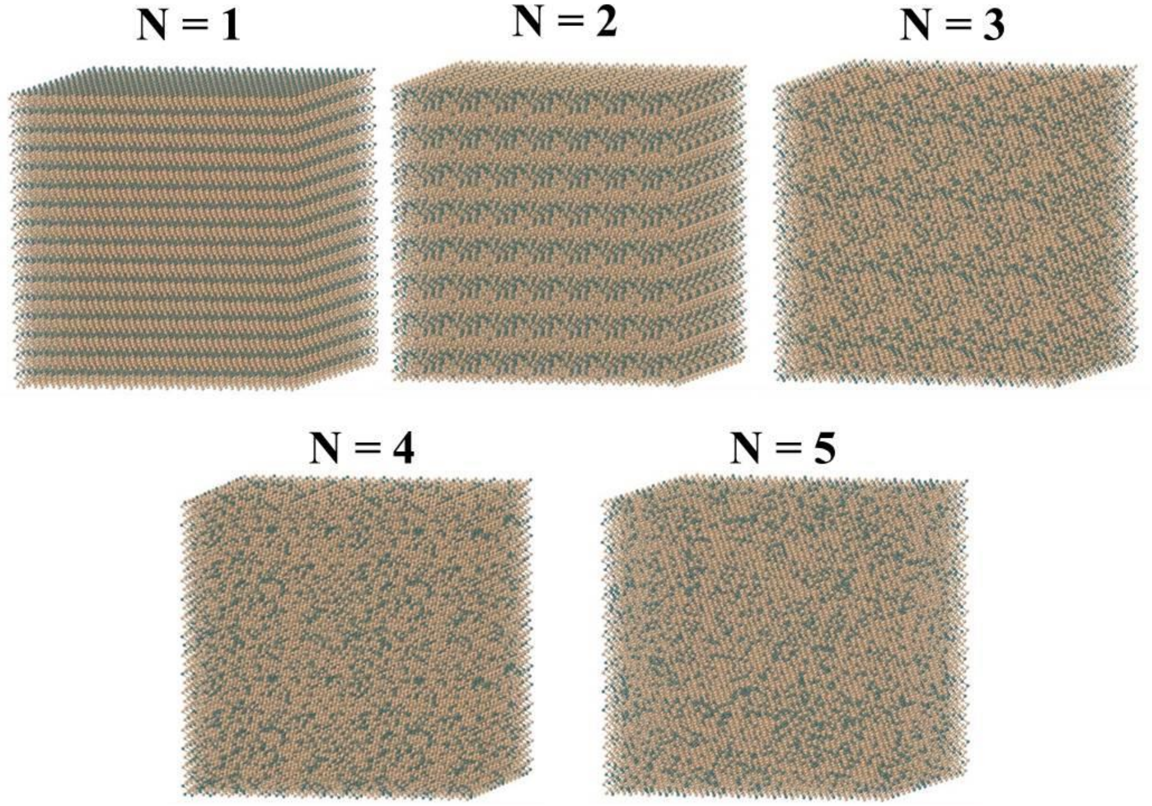

Figure 4.1: Representative structures of SiGe alloys with three dimensional periodic arrangements of small supercells at Ge contents = 25%; the number of atoms in all structures is 32768; supercell size N (in 2^{3N}) is from 1, 2, 3, 4 to 5. For different alloy compositions, lattice constants were adjusted according to the Vegard's law.

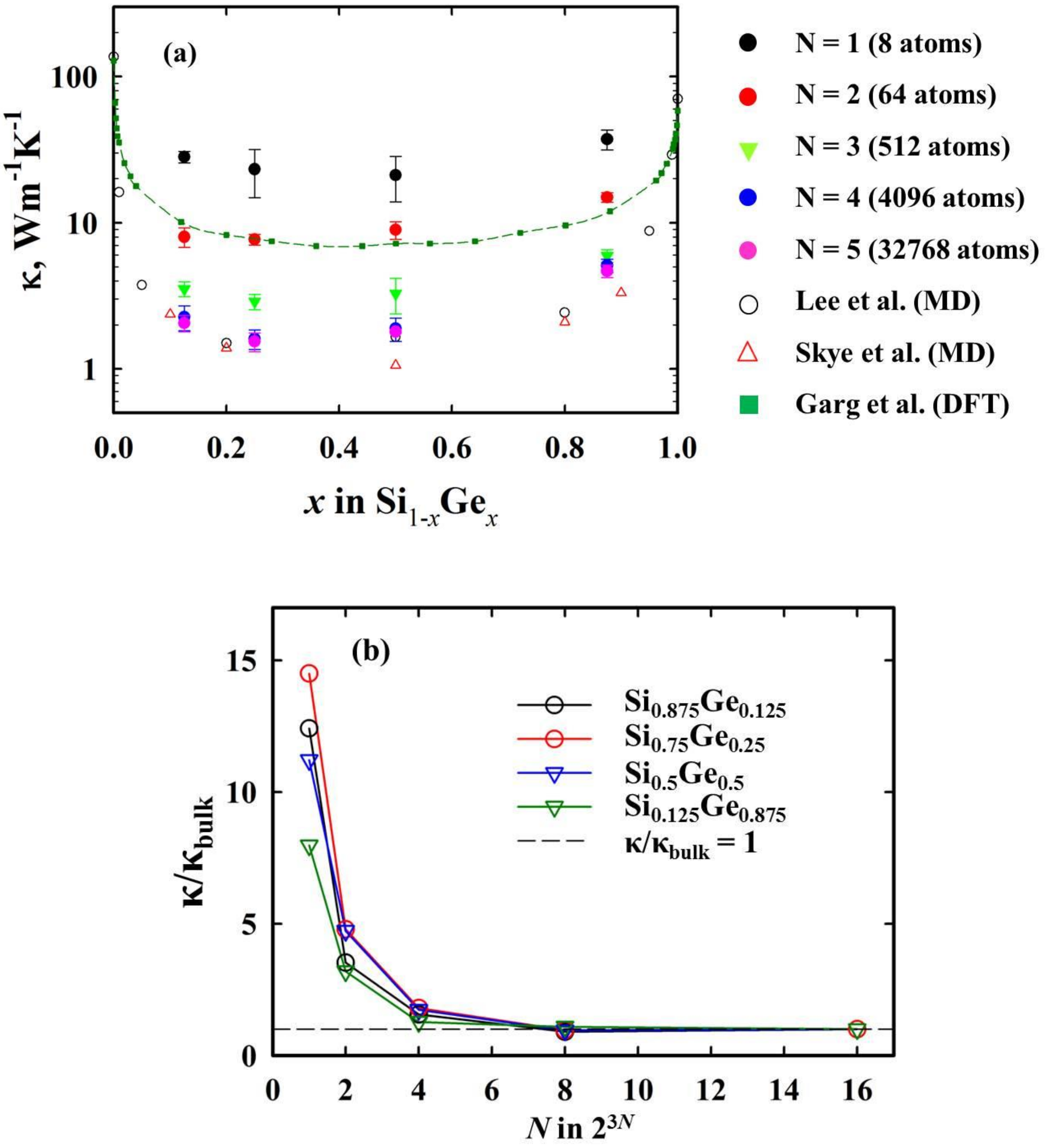

Figure 4.2: (a) Calculated thermal conductivities (κ) of $Si_{1-x}Ge_x$ (x = 0.125, 0.25, 0.5, and 0.875) for supercell size N = 1,2,3,4, and 5 (N in 2^{3N}). Open black circles[35] and red triangles[70] represent previous NEMD results, and filled green squares correspond to previous DFT results[57]. (b) Normalized thermal conductivities (κ/κ_{bulk}) of $Si_{1-x}Ge_x$ (x = 0.125, 0.25, 0.5, and 0.875) as a function of supercell size N = 1,2,3,4, and 5 (N in 2^{3N}). Black dashed line indicates $\kappa = \kappa_{bulk}$.

Figure 4.2 (a) summarizes the variations of κ with supercell size (N in 2^{3N}) for $Si_{1-x}Ge_x$ (x = 0.125, 0.25, 0.5, and 0.875), obtained from our EMD simulations; all the κ values were quantum corrected. As shown in Figure 4.2 (b), for each case, the κ value decreases rapidly with N and converge when $N \geq 4$ (corresponding to 4096 atoms). At x = 0.25, for instance, the κ (= 23.26 $Wm^{-1}K^{-1}$) at $N = 1$ is predicted to be about 15 times greater than the converged value of 1.53 $Wm^{-1}K^{-1}$ at $N = 4$.

Figure 4.2 (a) also shows that the converged κ values are nearly identical to those from our recent NEMD simulations [35], suggesting that the prediction of κ is rather insensitive to the choice of MD technique; (note that our NEMD simulations employed rectangular simulations cells containing 16000-64000 atoms which should be large enough for convergence). Both EMD and NEMD results well capture existing experimental observations in that i) for $x < 0.2$ (or $x > 0.8$), the κ rapidly drops as the Ge (or Si) content increases, ii) for x = 0.2-0.8, the κ shows insignificant variation with x, and iii) the minimum value of κ occurs around $x = 0.2$.

In Fig 4.2 (a), one interesting aspect is observed in comparison of our calculations with the results from density functional theory (DFT) based Boltzmann transport equation-relaxation time approximation (BTE-RTA) [57, 58]. For all compositions, κ values from BTE-RTA are relatively large compared to converged κ values in this work and previous NEMD studies. The values from BTE-RTA are quite similar to κ of $Si_{1-x}Ge_x(2^3)$ using 64 atoms supercell. For example, at $x = 0.5$, κ from BTE-RTA is about 7 $Wm^{-1}K^{-1}$ which is consistent κ = 8.93±1.22 $Wm^{-1}K^{-1}$ of $Si_{0.5}Ge_{0.5}(2^3)$. In BTE-RTA approach, phonon properties for estimation of thermal conductivity are obtained from

DFT calculations using supercells in DFT calculable sizes (normally, at most one or two hundreds). Our results might seem to addresses the possibility that phonon properties from DFT underestimate alloy scattering effect due to small supercell size.

Moreover, it would be worthwhile to note that the EMD results with $N = 2$ (corresponding to 64 atoms) appears to be in good agreement with that of recent first-principles calculations combined with the Boltzmann transport equation (BTE) [57]. In this approach, all the parameters necessary to compute κ were derived from the density-functional perturbation theory. Among others, a critical parameter is the phonon relaxation time which can be obtained using a combination of virtual crystal approximation (VCA) and supercell approach. While a 2-atom supercell (i.e., primitive unit cell) tends to be sufficient for pure Si [53, 57] or Ge [57], it has been found to be too small for extracting the accurate phonon relaxation time of SiGe alloys because of its inability to represent the random (irregular) atomic arrangement (i.e., mass disorder) [57].

The aforementioned first principles calculations employed a relatively large supercell with about 100 Si and Ge atoms. However, the significant deviation in κ from the converged EMD results ($N \geq 4$) may suggest that the supercell size would not yet be large enough to fully capture the effect of SiGe alloy disorder, warranting a further investigation of the convergence with respect to the supercell size.

4.3 Composition Effect on Thermal Conductivity of SiGe Alloys

For NEMD simulations, the simulation box was constructed according to the composite cell scheme; all layers have the same composition (Si:Ge ratio). Periodic boundary conditions were imposed in the x, y, and z directions, while heat conduction was allowed to occur only in the z direction. The cross-section of the rectangular box consists of 10×10 units (corresponding to 400 atoms). The S_H/S_C and B layer thicknesses were set at respective L_S and L_B values corresponding to one (or 400 atoms) and ten (or 4000 atoms) units, respectively, in the axial <100> direction, while L_I was varied depending on the total simulation cell length (L_{tot}), while L_I was varied from 40, 80, 120 to 160 units [corresponding to 16000, 32000, 64000, and 128000 atoms] depending on the total simulation cell length (L_{tot}). Following Vegard's law, the lattice parameter of $Si_{1-x}Ge_x$ (a_{SiGe}) was approximated using linear interpolation between the Si and Ge lattice constants (from DFT-GGA calculations), i.e, $a_{SiGe} = (1–x)a_{Si} + xa_{Ge}$, where a_{Si} = 5.4571 Å and a_{Ge} = 5.7564 Å.

The heat flux was imposed in the z direction by adding (subtracting) nontranslational kinetic energy to a group of atoms in the heat source (sink) layer. The κ of bulk $Si_{1-x}Ge_x$ was obtained by extrapolating finite-size results to infinite size; all κ values reported hereafter are after quantum corrections, unless stated otherwise. For quantum correction, the T_D for $Si_{1-x}Ge_x$ is approximated by $T_D(Si_{1-x}Ge_x) = (1–x)T_D(Si) + xT_D(Ge)$[184], where $T_D(Si)$ = 645 K and $T_D(Ge)$ = 374 K. For each of the $Si_{1-x}Ge_x$ systems considered, five independent NEMD simulations were performed with different atomic arrangements and initial velocity distributions. All NEMD simulations were performed using LAMMPS with a time step of 1 *fs*.

For NEMD simulations, we employed a general form of SW potential function with the potential parameters modified using a force-matching method[71] based on density functional theory (DFT) calculations. In this regard, the DFT force data were obtained by displacing one selected atom in the *x*, *y*, and *z* directions by 0.2 Å; the magnitude of the displacement was determined from test calculations with different values greater than the mean atomic displacement of about 0.147 Å [181] (0.077 Å [28]) in Ge (Si) at room temperature. The restoring forces acting on the displaced atom and its four first- and twelve second-nearest neighbors were considered to be matched in the SW parameter adjustments. All DFT calculations were performed within the GGA-PW91[89], as implemented in the VASP[90]. We used Vanderbilt-type ultrasoft pseudopotentials[91] to represent the interaction between core and valence electrons, and a planewave basis set with a kinetic energy cutoff of 160 eV. We used a 64-atom cubic supercell and a $(2\times2\times2)$ Monkhorst-Pack grid of *k* points for the Brillouin zone sampling.

Table 4.1 summarizes the modified SW parameters obtained from the force matching approach based on DFT-GGA [SW(GGA)]. Figure 4.3 shows the comparisons of the restoring forces from the SW(GGA) and DFT calculations for different $Si_{1-x}Ge_x$ samples ($x = 0.25$, 0.5, and 0.75); note that the SW(GGA) and DFT results are in excellent agreement, while the forces from original SW [SW(ORG)] are consistently overestimated.

Table 4.1: Stillinger Weber (SW) parameters modified based on the interatomic forces from first principles calculations for the study of thermal transport in Si, Ge, and SiGe.

	σ	**ε (eV)**	**λ**	***a***	***γ***	
Si	2.1051937	1.41992	29.5303	1.8	1.2	A = 7.049556277
Ge	2.221545	1.30665	24.6348	1.8	1.2	B = 0.6022245584
SiGe	2.141453	1.459299	31.0776	1.843	1.3428	p = 4.0 q = 0.0

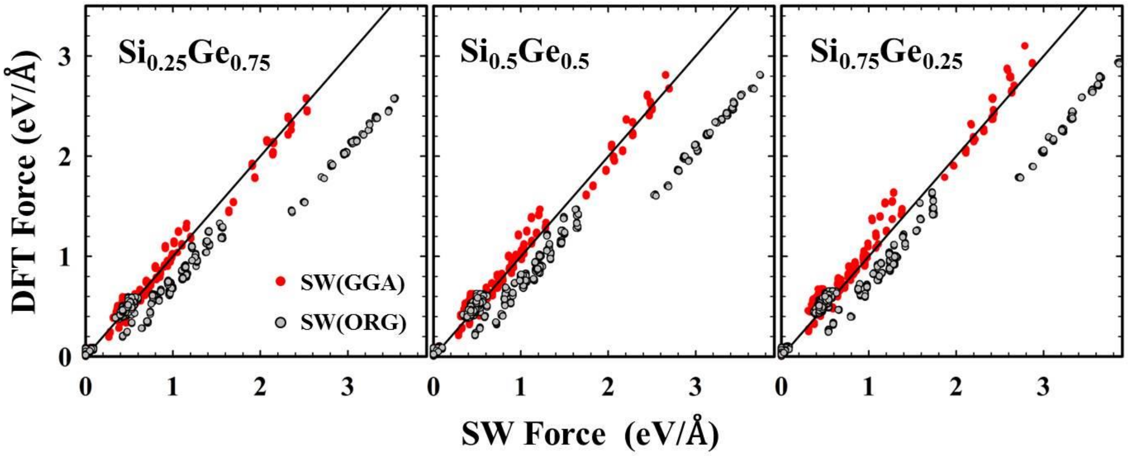

Figure 4.3: Parity plots showing discrepancies between DFT and SW predictions for the restoring forces acting on the displaced atom and its first- and second-nearest neighbors in three different SiGe alloys as indicated.

With the modified SW parameter, we calculated the κ of bulk $Si_{1-x}Ge_x$ as a function of x; here, Si and Ge atoms were assumed to be *randomly* distributed. As presented in Fig. 4.4, the κ values of pure Si and Ge are predicted to be 136.65 ± 9.15 $Wm^{-1}K^{-1}$ and 70.23 ± 7.32 $Wm^{-1}K^{-1}$ at 300K, respectively, close to the corresponding experimental values of 156.38 $Wm^{-1}K^{-1}$ [165] and 60 $Wm^{-1}K^{-1}$ [85]; by contrast, the original SW(ORI) parameter sets yield much higher κ values (243.99 ± 19.75 $Wm^{-1}K^{-1}$ for Si and 152.25 ± 17.23 $Wm^{-1}K^{-1}$ for Ge).

For $x < 0.2$ or $x > 0.8$, the κ of the host (Si or Ge) matrix rapidly drops as the heteroatom (Ge or Si) content (n_i) increases. For $x = 0.2$-0.8, the κ of $Si_{1-x}Ge_x$ shows no significant variation with x. Our simulations predict the minimum κ to be 1-2 $Wm^{-1}K^{-1}$ (corresponding to 0.5-1 mK/W of thermal resistance) around $x = 0.2$.

The reduction of κ with n_i can be well described by an inverse power law relationship,$\kappa \propto n_i^{-1}$; the best fits are given when α = 0.83094 and 0.99827 for $x < 0.2$ and $x > 0.8$, respectively. The different values of α clarifies that the introduction of heavy impurities in a light host will cause a greater reduction in κ than the case of light impurities in a heavy host. This is also well supported by the theoretical model suggested by Abeles[147]; that is, the strength of alloy scattering (Γ) due to the mass difference between alloying elements is given by: $\Gamma = \sum_i x_i \left(\frac{M_i - M}{M} \right)^2$, where x_i and M_i are the fractional concentration and the atomic weight of element i, respectively, and M is the atomic weight of the alloy ($M = \sum_i x_i M_i$). According to the model, for instance, the scattering strengths are approximated to be 0.024098 in $Si_{0.99}Ge_{0.01}$ (x_{Si} = 0.99) and 0.003768 in $Si_{0.01}Ge_{0.99}$ (x_{Si} = 0.01); that is, the scattering strength of Ge in the lighter Si lattice is approximately 6 times greater than that of Si in the heavier Ge lattice although the heteroatom contents are identical at 1 at.%.

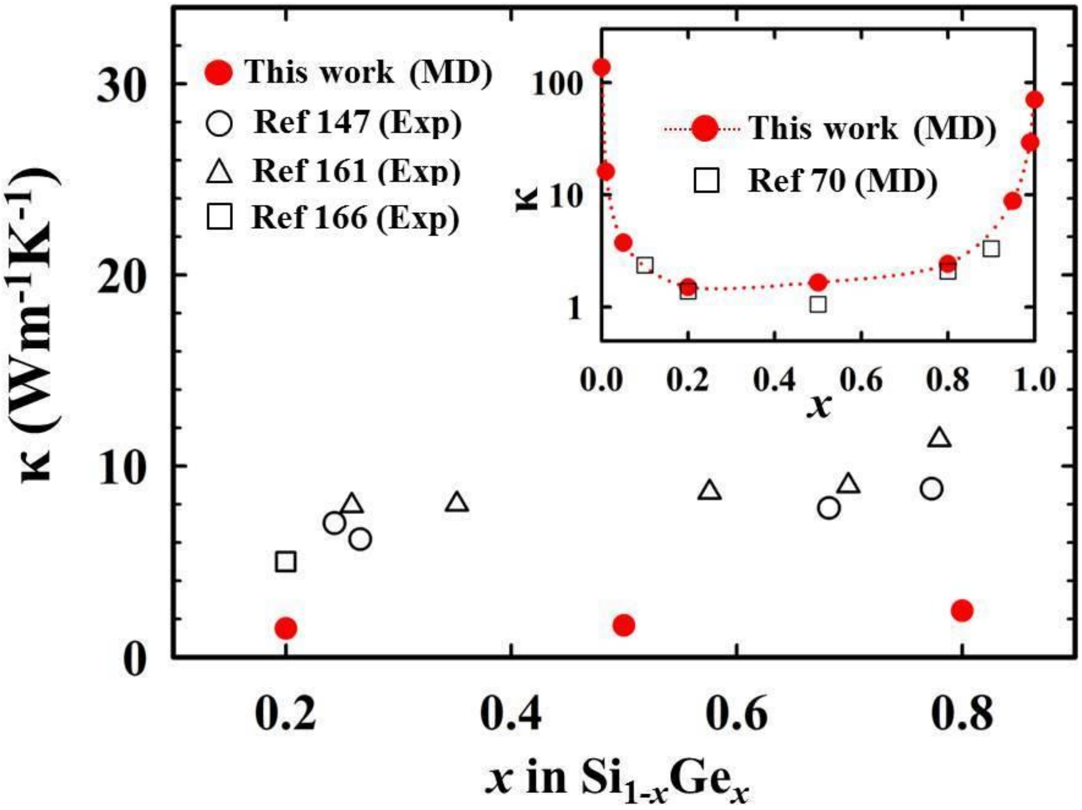

Figure 4.4: Predicted variation of the thermal conductivity (κ) of $Si_{1-x}Ge_x$ at 300K. Solid red (black) circles show the κ values from our NEMD simulations, while open circles, triangles, and squares indicate the experimental values of Abeles [147], Stohr and Klemm [161], and Vining [166], respectively. The inset shows a comparison of κ with previous MD results [70].

4.4 Microsegregation Effect on Thermal Conductivity of SiGe Alloys

The simulated trend of κ with *x* is overall consistent with existing experimental observations. However, the predicted minimum κ is substantially smaller than the experimentally reported values of 5-10 $Wm^{-1}K^{-1}$ at $x \approx 0.2$. A couple of likely reasons have been suggested for the discrepancy between the classical MD and experimental results, including possible exaggeration of point defect scattering[70] and insufficient convergence due to relatively small simulation cells[175]. In addition, as mentioned in the introduction, the microsegregation effect may play a certain role in causing the experimental κ values to be larger than the classical MD results; note that previous MD simulations mostly assumed random mixing of Si and Ge atoms. In this section, we examine the dependence of κ on the local segregation of alloying elements.

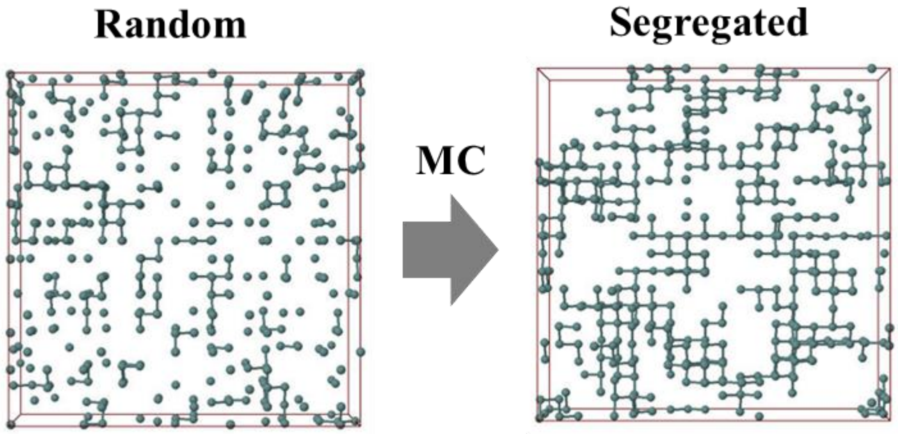

Figure 4.5: Schematic cross-sectional views of Ge atoms in $Si_{0.8}Ge_{0.2}$; (left) randomly distributed, (right) segregated. Ge segregation was simulated using a Monte Carlo (MC) method with a relatively reduced Si-Ge bond energy with respect to Si-Si and Ge-Ge bond energies. For clarity, only a part of each $Si_{0.8}Ge_{0.2}$ simulation domain is shown here.

Table 4.2: Predicted thermal conductivity (κ) values at 300K for $Si_{0.8}Ge_{0.2}$ with different degrees of Ge segregation; the segregated $Si_{0.8}Ge_{0.2}$ samples were obtained using Monte Carlo simulations (see Fig. 4.5). α_i is the Cowley's short range order parameter at the i^{th} neighbor shell.

κ ($Wm^{-1}K^{-1}$)	α_1	α_2	α_3
2.14	0.381	0.079	-0.012
2.11	0.376	0.074	-0.018
2.05	0.360	0.071	-0.019
1.99	0.354	0.060	-0.022
1.85	0.291	0.045	-0.021
1.78	0.272	0.033	-0.017
1.56	0.235	-0.010	-0.014

We examined the variation of κ in $Si_{0.8}Ge_{0.2}$ by changing the extent of Ge segregation. As illustrated in Fig. 4.5, the segregated $Si_{0.8}Ge_{0.2}$ samples were generated using Monte Carlo (MC) simulations with a relatively reduced Si-Ge bond energy with respect to Si-Si and Ge-Ge bond energies. The extent of segregation can be quantified using the Cowley short range order parameter[182], defined by $\alpha_i = 1 - p_i/x_{Si}$, where the subscript i represents the i^{th} neighbor shell from a selected Ge atom, p_i is the probability of having a Si atom in the i^{th} shell, and x_{Si} is the mole fraction of Si. The parameter α_i ranges from 1 to $1 - x_{Si}^{-1}$; $\alpha_i > 0$ indicates that Ge has a tendency to segregate while $\alpha_i = 0$ (i.e., $p_i = x_{Si}$) means a completely random distribution. As summarized in Table 4.2, as Ge atoms undergo segregation, α_1 and α_2 gradually increase while $\alpha_2 << \alpha_1$ and $\alpha_3 \approx 0$. Our calculations predict the κ of $Si_{0.8}Ge_{0.2}$ to monotonically increase with α_1, and κ = 2.14 $Wm^{-1}K^{-1}$ at $\alpha_1 = 0.381$ is about 70 % larger than the case of random mixing (= 1.25 $Wm^{-1}K^{-1}$). Although the simple structural model may not explicitly represent the complex potential inhomogeneity of SiGe alloys, the results unequivocally suggest that the local segregation of alloying elements can play an important role in determining κ.

To further investigate the microsegregation effect, we prepared several $Si_{0.8}Ge_{0.2}$ samples by embedding spherical Ge particles of different sizes (ranging from 5 to 293 atoms) in the Si matrix. As illustrated in Fig. 4.6, embedded Ge particles were randomly positioned but not allowed to overlap each other. Figure 4.7 shows the variation of κ for the $Si_{0.8}Ge_{0.2}$ samples as a function of Ge particle diameter (D_e); here, D_e is approximated by $(6N_{Ge}V_{Ge}/\pi)^{1/3}$, where N_{Ge} is the number of Ge atoms in the particle and V_{Ge} is the volume per atom for Ge (= 0.0238 nm^3 from our DFT-GGA calculation). The κ is predicted to monotonically increase with D_e; note that κ = 4.18 $Wm^{-1}K^{-1}$ at D_e = 2.37 nm is about 3.3 times greater than κ = 1.25 $Wm^{-1}K^{-1}$ for the random alloy. The results clearly demonstrate that the κ of SiGe alloys can be sensitive to the local segregation of Si and Ge atoms.

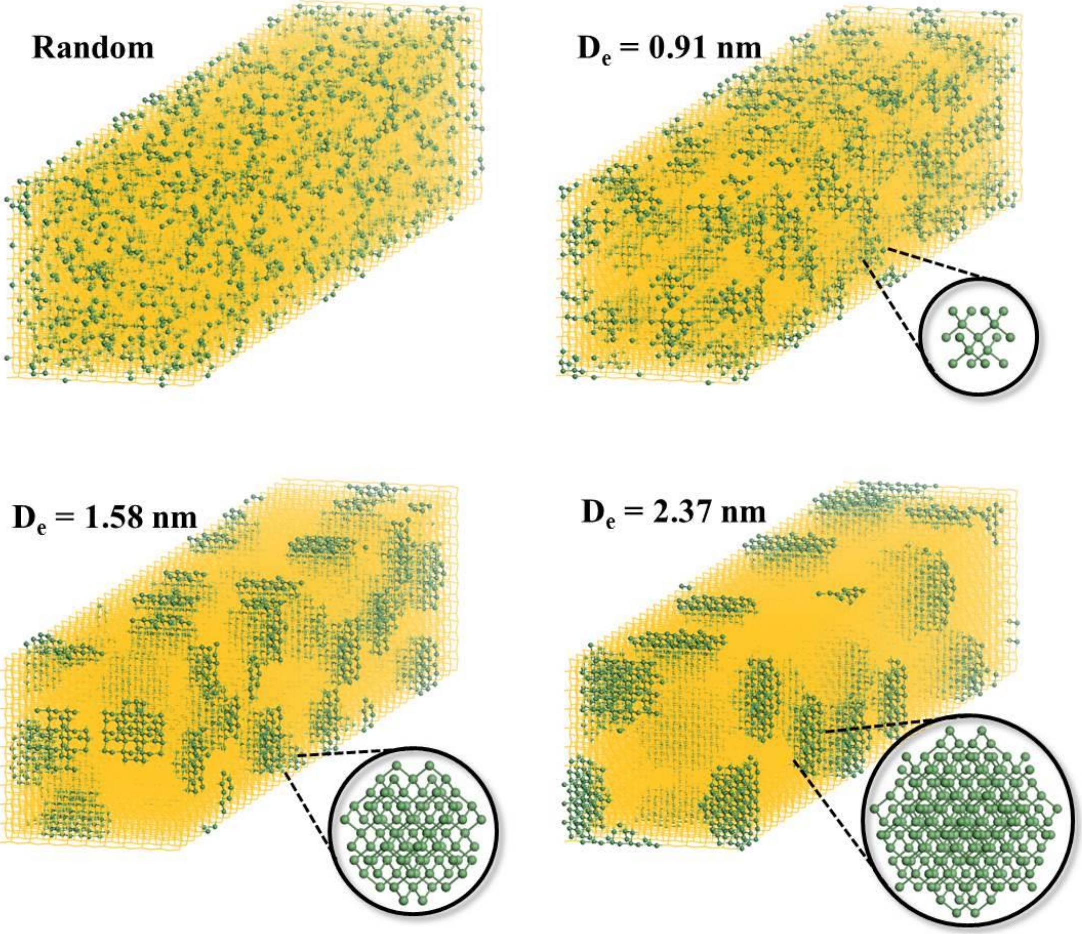

Figure 4.6: The various $Si_{0.8}Ge_{0.2}$ configurations show a random distribution of Si and Ge atoms (Random) and embedded Ge particles with different diameters (D_e = 0.91, 1.58, and 2.37 nm) in the Si matrix. Green (black) balls and yellow lattices represent Ge and Si atoms, respectively.

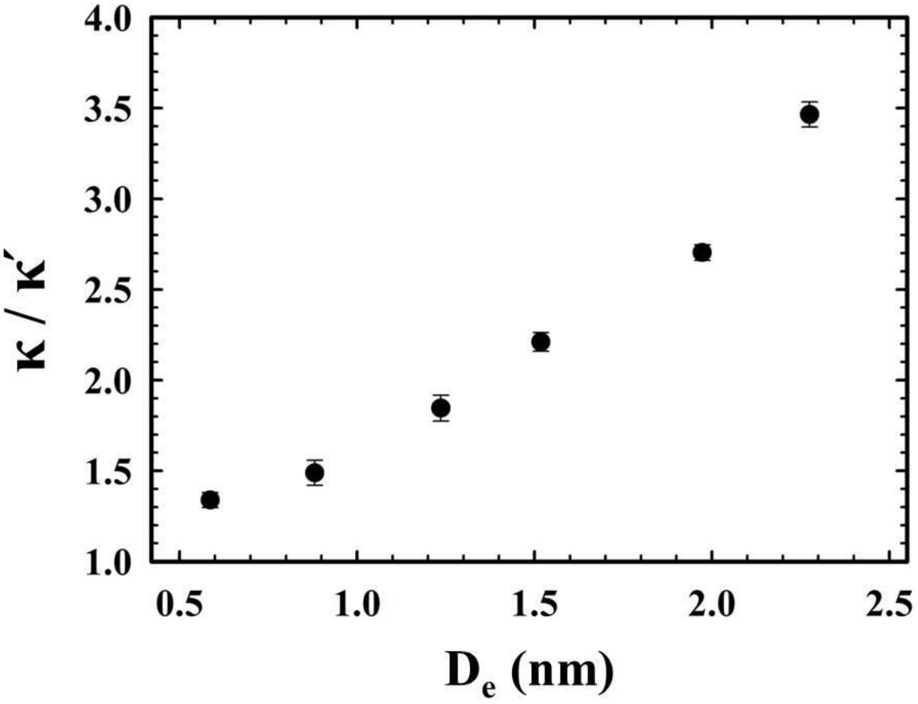

Figure 4.7: Predicted variation of the relative thermal conductivity with respect to the random alloy ($\kappa/\kappa^{/}$) as a function of the diameter (D_e) of Ge particles embedded in $Si_{0.8}Ge_{0.2}$ (see Fig. 4.6); note that the predicted $\kappa^{/}$ for the randomly distributed $Si_{0.8}Ge_{0.2}$ sample is about 1.25 $Wm^{-1}K^{-1}$.

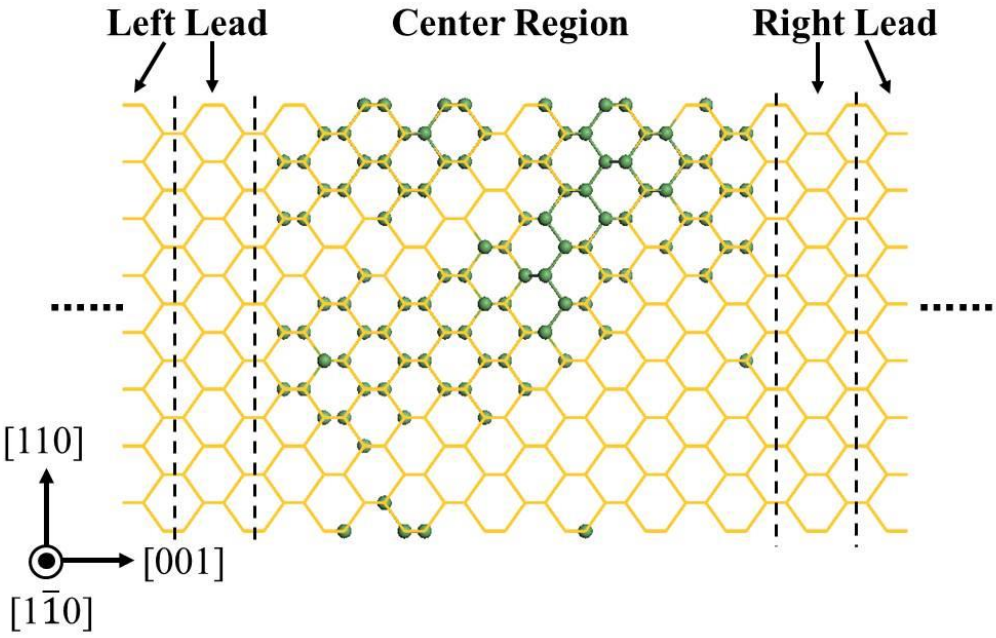

Figure 4.8: Schematic diagram showing the domain of our nonequilibrium green's function (NEGF) simulation. Green balls and yellow lines represent Ge atoms and the Si lattice, represented. The lattice constant of each lead is set at 5.5169 Å.

To better understand the role of microsegregation, we examined transmission characteristics of phonons in different $Si_{0.8}Ge_{0.2}$ structures using the nonequilibrium Green's function (NEGF) approach[152,153]. Here, we ignored nonlinear phonon-phonon scatterings, as our primary concern was to understand the dependence of alloy scattering on the local segregation of alloying elements. Here, the dynamic matrices for the transmission coefficient calculations were obtained from the second derivative of the SW(GGA) potential energy surface with a displacement of 0.02 Å. Within the NEGF framework, as illustrated in Fig. 4.8, each calculation system consists of a central scattering alloy region and two semi-infinite Si leads; the axial lengths of the scattering region and each lead were set to 33.13 Å and 5.52 Å, respectively. The $Si_{0.8}Ge_{0.2}$ alloy in the scattering region has randomly distributed Ge atoms or Ge particles (with D_e = 0.91, 1.58, or 2.37 nm corresponding to 17, 87, or 293 Ge atoms, respectively).

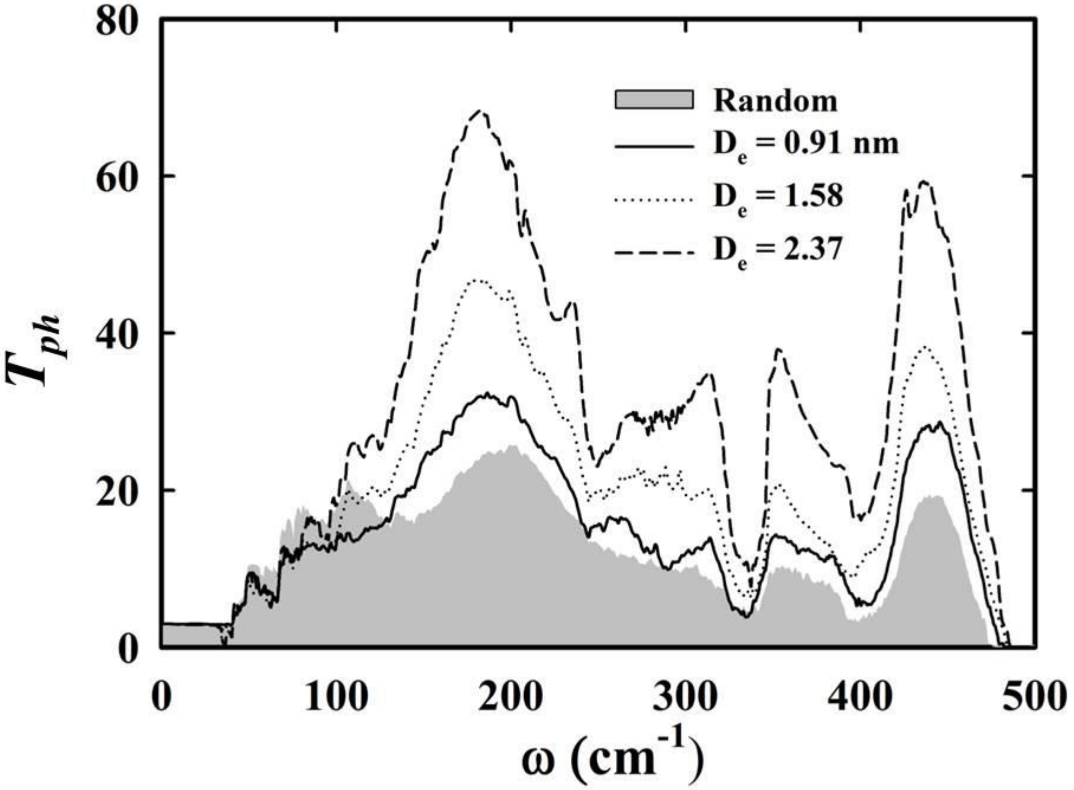

Figure 4.9: Frequency-dependent phonon transmission coefficients (T_{ph}) calculated for Ge particle-embedded $Si_{0.8}Ge_{0.2}$ with comparison to the random alloy case where Si and Ge atoms are homogeneously distributed.

Figure 4.9 shows calculated frequency-dependent phonon transmission coefficients for the considered $Si_{0.8}Ge_{0.2}$ systems. With increasing the size of Ge particles (or the degree of microsegregation), the transmission of phonons is found to increase rapidly, except for the low frequency regime ($\omega < 130$ cm^{-1}). Given that mass disorder is mainly responsible for the reduction of κ in the SiGe alloy, single and paired

Ge atoms may act mainly as scattering centers when they are atomically dispersed. On the other hand, when Ge atoms remain locally segregated, scattering by the mass difference would occur at Ge particle-Si matrix interfaces, and also Ge particles may provide additional scattering centers. Therefore, such Ge segregation will reduce the number of scattering centers, thereby increasing phonon transmission, compared to when Ge atoms are homogeneously distributed in the $Si_{0.8}Ge_{0.2}$ matrix. It is also worth noting that the transmission coefficient appears to be rather insensitive to the extent of microsegreation when ω is below 100 cm^{-1}. The transport of such low-frequency (long-wavelength) phonons may undergo scattering mainly due to Ge particles; in this case, phonon transmission can be effectively blocked if the Ge particle concentration is large enough, and thus it becomes no longer a strong function of particle size [65].

Our study clearly demonstrates that the local segregation (microsegregation) of alloying elements, along with composition, can be a critical factor in determining the κ of alloys; that is, the magnitude of alloy scattering can be sensitive to the homogeneity in distribution of alloying elements. We speculate that the strong microsegregation effect could be one of the possible reasons, perhaps along with structural irregularities such as grain boundaries[167-170], for the wide distribution of the experimentally observed κ values of SiGe; for instance, the κ of $Si_{0.8}Ge_{0.2}$ has been reported to range from 2.5 to 10 $Wm^{-1}K^{-1}$. Note that the experimental samples were mostly obtained via mechanical alloying (ball milling) of Si and Ge chunks. Given that, Si and Ge may not always be fully mixed at the atomic scale, and moreover the local segregation, if any, would strongly depend on sample preparation conditions; if so, this could cause a significant variation in κ from sample to sample. Furthermore, the increase of κ with microsegregation may suggest that the minimum κ would be achieved when Si and Ge atoms are randomly distributed; that is, κ suppression due to alloy scattering could be maximized in the random SiGe alloy. This can be another possible reason why the experimental values of κ are consistently larger than those from classical MD simulations (that assume a random distribution of Si and Ge atoms).

4.5 Heat Transport in Si-Ge-Sn Ternary Alloys

For NEMD simulations, the rectangular shaped-simulation box was prepared with the composite cell scheme; all layers have the same composition (Si:Ge:Sn ratio). Periodic boundary conditions were imposed in the *all* directions. The cross-section of the rectangular box consists of 10×10 units (corresponding to 400 atoms). The S_H/S_C and B layer thicknesses were set at respective L_S and L_B values corresponding to one (or 400 atoms) and ten (or 4000 atoms) units, respectively, in the axial <100> direction, while L_I was varied depending on the total simulation cell length (L_{tot}). The heat flux was imposed in the *z* direction by adding (subtracting) nontranslational kinetic energy to a group of atoms in the heat source (sink) layer.

The κ of bulk SiGeSn was obtained by extrapolating finite-size results to infinite size; all κ values reported hereafter are after quantum corrections, unless stated otherwise. For each systems considered, five independent NEMD simulations were performed with different atomic arrangements and initial velocity distributions. All NEMD simulations were performed using LAMMPS [76] with a time step of 1 *fs*.

4.5.1 Force-Field Optimization for SiGeSn Ternary Alloys

For NEMD simulations, we optimized the SW potential parameters using a force-matching method[71] based on DFT calculations. For SiGeSn ternary alloy systems, six different two-body and 18 three-body interactions exist. For interactions including only Si and Ge atoms, we adopted the potential parameters re-optimized in our previous studies [35,70]. The potential parameters for the remaining interactions were newly obtained in this work. For optimizing the potential parameters, the training sets of force data were prepared using DFT calculations. We used a 64-atom cubic supercell and a $(2\times2\times2)$ Monkhorst-Pack grid of k points for the Brillouin zone sampling. While all 64 atoms are Sn for Sn-Sn system, for two- and three-body interactions for Si-Sn or Ge-Sn, one atom in each supercell was replaced with Sn atom in the Si or Ge matrix, respectively. In this regard, the DFT force data were obtained by displacing one selected atom in the x, y, and z directions by 0.2 Å; the magnitude of the displacement was determined from test calculations with different values greater than the mean atomic displacement of about 0.178[181], 0.147[181], or 0.077 Å [28] in Sn, Ge, or Si at room temperature. The restoring forces acting on the displaced atom and its four first- and twelve second-nearest neighbors were considered to be matched in the SW parameter adjustments. All DFT calculations were performed within the GGA-PW91[89], as implemented in the VASP[90]. We used Vanderbilt-type ultrasoft pseudopotentials[91] to represent the interaction between core and valence electrons, and a planewave basis set with a kinetic energy cutoff of 200 eV.

Table 4.3: Stillinger Weber (SW) parameters modified based on the interatomic forces from first principles calculations for the study of thermal transport in Sn, SiSn, and GeSn.

	σ	ε (eV)	λ	a	$\boldsymbol{\gamma}$	
Sn	2.5681	1.2351	19.0031	1.8	1.2	A = 7.049556277
SiSn	2.2617	1.6435	8.7433	1.9172	1.1	B = 0.6022245584
GeSn	2.3313	1.5592	11.9601	1.8894	1.1	p = 4.0 q = 0.0

Table 4.3 summarizes the modified SW parameters obtained from the force matching approach. Figure 4.10 shows the comparisons of the restoring forces from the SW and DFT calculations for Sn, SiSn, and GeSn samples; the SW Forces and DFT results are in excellent agreement. It is worth to comment that three-body interaction parameter λ for pairs not listed in this table was obtained using the mixing rule ($\lambda_{ijk} = \sqrt{\lambda_{iji}\lambda_{kjk}}$), instead of performing the time consuming optimization procedure for all possible three-body pairs, where *i*,*j*,*k* is Si,Ge, or Sn and *j* is the center atom of three-body pair. Because the mass difference effect is a dominant factor for phonon scattering in alloy systems, applying the mixing rule for the three-body hetero pairs (i.e. $i \neq k$) might work reasonably in estimating heat transport, as shown in the previous study for Si-Ge alloys [35]. We will check the validity of this approximation in the discussion part.

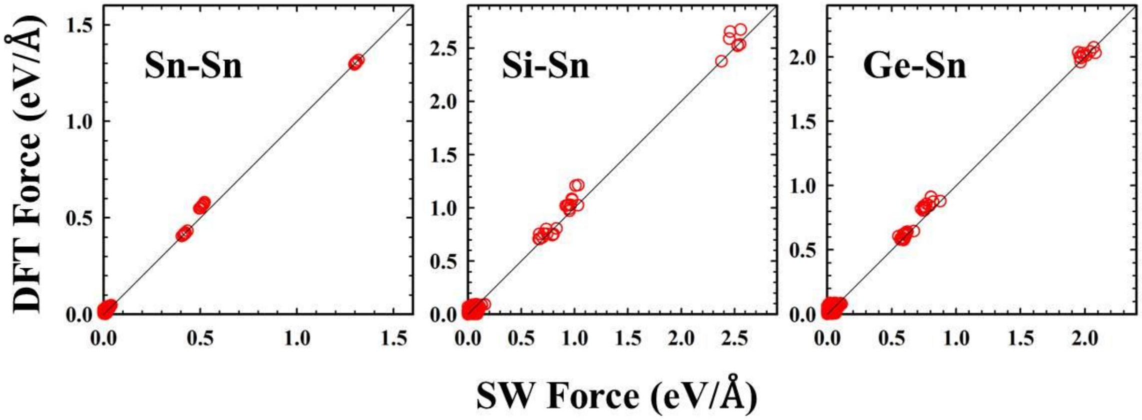

Figure 4.10: Parity plots showing discrepancies between DFT and SW predictions for the restoring forces acting on the displaced atom and its first- and second-nearest neighbors in Sn, SiSn, or GeSn as indicated.

Before investing heat transport in the SiGeSn alloy, we checked the capability of the modified potential for Sn in estimating its κ, while the κ values of pure Si and Ge using the re-optimized potentials were predicted to be close to the corresponding experimental values [35,70]. For NEMD calculations, the cross-sectional area of each simulation domain is 4.7054×4.7054 nm^2, and the total axial length of the rectangular domain varies from L_{tot} = 53.2354, 79.8531, 106.471, 133.088, 159.706, to 212.942 nm (corresponding to 80, 120, 160, 200, 240, and 320 slabs, respectively). As shown in Fig. 4.11, we calculated the bulk thermal conductivities of *c*-Sn by extrapolating calculated ($1/L_z$, $1/\kappa$) values to $1/L_z = 0$. At 300 K, the calculated κ values of 62.65 ±4.52 Wm^{-1}K^{-1} is in good agreement with the experimental value of 66.8 Wm^{-1}K^{-1} [85]; note that quantum correction is not applied because Debye temperature of Sn = 200 K [85] < 300 K).

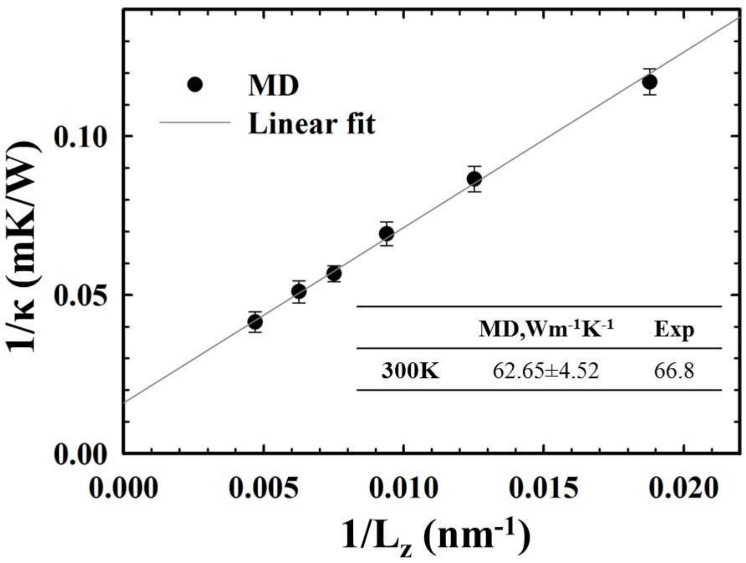

Figure 4.11: Thermal resistivity (1/κ) for c-Sn as a simulation cell length at 300 K; the linear line indicates the best-fit linear regression. Here, L_z is the distance between the heat source and heat sink centers, which is half of the total simulation domain length.

4.5.2 Prediction of the Thermal Conductivity of SiGeSn Alloys

With the modified SW parameter set, we calculated the κ of bulk SiGeSn at 300K. Here, we investigated bulk SiGeSn within the experimentally viable composition range [183-189]; here, we focused on $Si_{0.2-x}Ge_{0.8}Sn_x$ where $x \leq 0.2$. For NEMD calculations, Si, Ge, and Sn atoms were assumed to be *randomly* distributed. The lattice parameter of $Si_{0.2-x}Ge_{0.8}Sn_x$ (a_{SiGeSn}) was approximated using the Vegard's law with the bowing correction, by using quadratic interpolation of the lattice constants of Si, Ge, and Sn (from DFT-GGA calculations), i.e, for $Si_xGe_{1-x-y}Sn_y$, $a_{SiGeSn} = a_{Ge} + \Delta_{SiGe} \times x + \theta_{SiGe} \times x(1-x) + \Delta_{SnGe} \times y + \theta_{GeSn} \times y(1-y)$, where a_{Si} = 5.4571 Å, a_{Ge} = 5.7564 Å, and a_{Sn} = 6.657 Å are the lattice constants of Si, Ge, and Sn, respectively, and Δ_{SiGe} (Δ_{SnGe}) are $a_{Si} - a_{Ge}$ ($a_{Sn} -$

a_{Ge}), respectively. The bowing parameter for the lattice constant of Si_xGe_{1-x}, θ_{SiGe}, is -0.026 and that of $Ge_{1-y}Sn_y$, θ_{GeSn}, is 0.166. [190]. For the quantum correction, the T_D for $Si_xGe_{1-x-y}Sn_y$ is approximated by a simple interpolation formula [191].

Figure 4.12 shows the predicted thermal conductivities of $Si_{0.2-x}Ge_{0.8}Sn_x$ as a function of x. The κ of the ternary alloy is predicted to be reduced as the Sn content increases in the binary $Si_{0.2}Ge_{0.8}$ matrix ($x = 0$) or the Si content increases in the binary $Ge_{0.8}Sn_{0.2}$ matrix ($x = 0.2$). According our calculations, the predicted minimum κ of $Si_{0.2-x}Ge_{0.8}Sn_x$ occurs around $x = 0.1$; the minimum κ = 1.791 $Wm^{-1}K^{-1}$, which is about 38% and 40% lower compared to the $Si_{0.2}Ge_{0.8}$ and $Ge_{0.8}Sn_{0.2}$ cases.

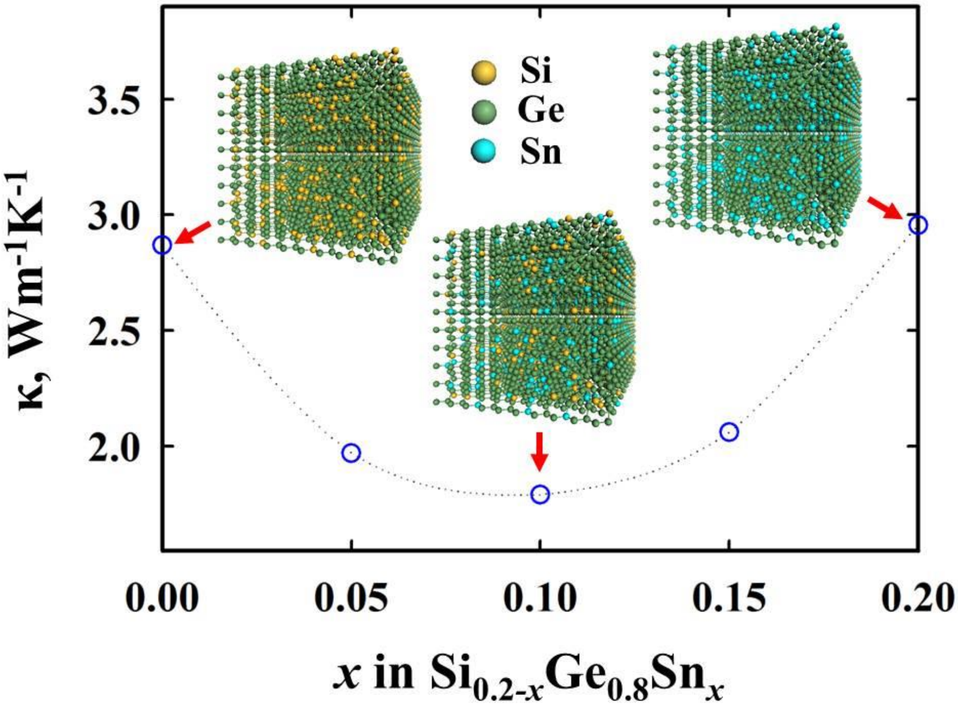

Figure 4.12: Predicted thermal conductivities (κ) of $Si_{0.2-x}Ge_{0.8}Sn_x$ alloys at 300K as a function of Sn content x.

It has been well known that the large mass difference between Si and Ge atom is the main mechanism in suppressing heat transport in the SiGe alloy [35,57]. With the knowledge about the dominant effect of mass disorder on the κ of alloys, in order to investigate how dominant the mass disorder effect is in reducing the κ of SiGeSn, we investigated the relative contribution of the mass disorder effect by assuming that Si and Sn atoms have the same radius and force constants as Ge, but they have their own masses (m_{Si} = 28.08, m_{Ge} = 72.04, and m_{Sn} = 118.71). Considering the predicted κ (= 70.23 $Wm^{-1}K^{-1}$[35]) of Ge as a reference, the extent of κ reduction [$\Delta\kappa$ (mass) = $\kappa_{Ge} - \kappa$(mass)] due to mass disorder is predicted to be 66.83, 68.03, 68.21, 67.98, or 66.82 $Wm^{-1}K^{-1}$, which is about 99% of the total reduction [$\Delta\kappa = \kappa_{Ge} - \kappa_{Si0.2-xGe0.8Snx}$] of 67.36, 68.25, 68.43, 68.16, or 67.27 $Wm^{-1}K^{-1}$, at x = 0, 0.05, 0.1, 0.15, and 0.2, respectively. These results suggest that the mass disorder effect is primarily responsible for κ suppression in the ternary alloy system. The dominant mass disorder effect may confirm the validity of applying the mixing rule for the hetero three-body interactions.

The reduction of κ for SiGeSn can be explained with the increased mass disorder effect, compared to those for binary SiGe and GeSn alloys. For the SiGe (or GeSn) alloy case, only the mass difference $|\Delta m_{Si-Ge}|$ = 44.53 (or $|\Delta m_{Sn-Ge}|$ = 46.1) between Si and Ge (or Ge and Sn) exists. However, in the SiGeSn alloy, the degree of mass disorder increases, i.e, both $|\Delta m_{Si-Ge}|$ and $|\Delta m_{Sn-Ge}|$ need to be taken into account. Furthermore, additional even larger mass disorder ($|\Delta m_{Si-Ge}|$ = 90.63) due to Si-Sn plays a important role in enhancing phonon scatterings.

Similar values of mass differences $|\Delta m_{Si\text{-}Ge}|$ and $|\Delta m_{Sn\text{-}Ge}|$ might explain why the minimum κ value of $Si_{0.2\text{-}x}Ge_{0.8}Sn_x$ occurs when the Si and Sn contents are comparable.

It is noteworthy that the SiGe alloy has a lower κ value than the GeSn alloy, while they have similar mass differences in magnitude. The strength of alloy scattering (Γ) due to the mass difference between alloying elements is given by: $\Gamma = \sum_i x_i \left(\frac{M_i - M}{M} \right)^2$, where x_i and M_i are the fractional concentration and the atomic weight of element i, respectively, and M is the atomic weight of the alloy ($M = \sum_i x_i M_i$). According to the model, the scattering strengths are approximated to be 0.07818 in $Si_{0.2}Ge_{0.8}$ ($x_{Si} = 0.2$) and 0.05078 in $Ge_{0.8}Sn_{0.2}$ ($x_{Sn} = 0.2$); that is, the scattering strength of heavier Sn in the lighter Ge lattice is approximately 50% greater than that of lighter Si in the Ge lattice although the heteroatom contents are identical[35].

In order to better understand the effect of alloying with Sn in the reduction of κ, we analyzed localization of the eigenmodes of vibration for the alloy systems. The eigenmodes of the system and their frequencies are obtained by direct diagonalization of the dynamical matrix, computed from finite differenes of the atomic forces. The mode localization can be qualitatively assessed by the participation ratio (p_{ph}) which is defined for eigenmode i as[105,106] $p_{ph}^{-1} = N \sum_j \left(\sum_\alpha \varepsilon_{j\alpha,i}^{*} \varepsilon_{j\alpha,i} \right)^2$, where N_T is the total number of atoms and $\varepsilon_{j\alpha,i}$ is the eigenvector corresponding to i. Indicating the fraction of atoms participating in a given normal mode of vibration, the value of p_{ph} always lies between 1 and $1/N_T$; that is, $p_{ph} = 1$ if all N_T atoms vibrate with equal amplitude while $p_{ph} = 1/N_T$ for a mode involving only one atom.

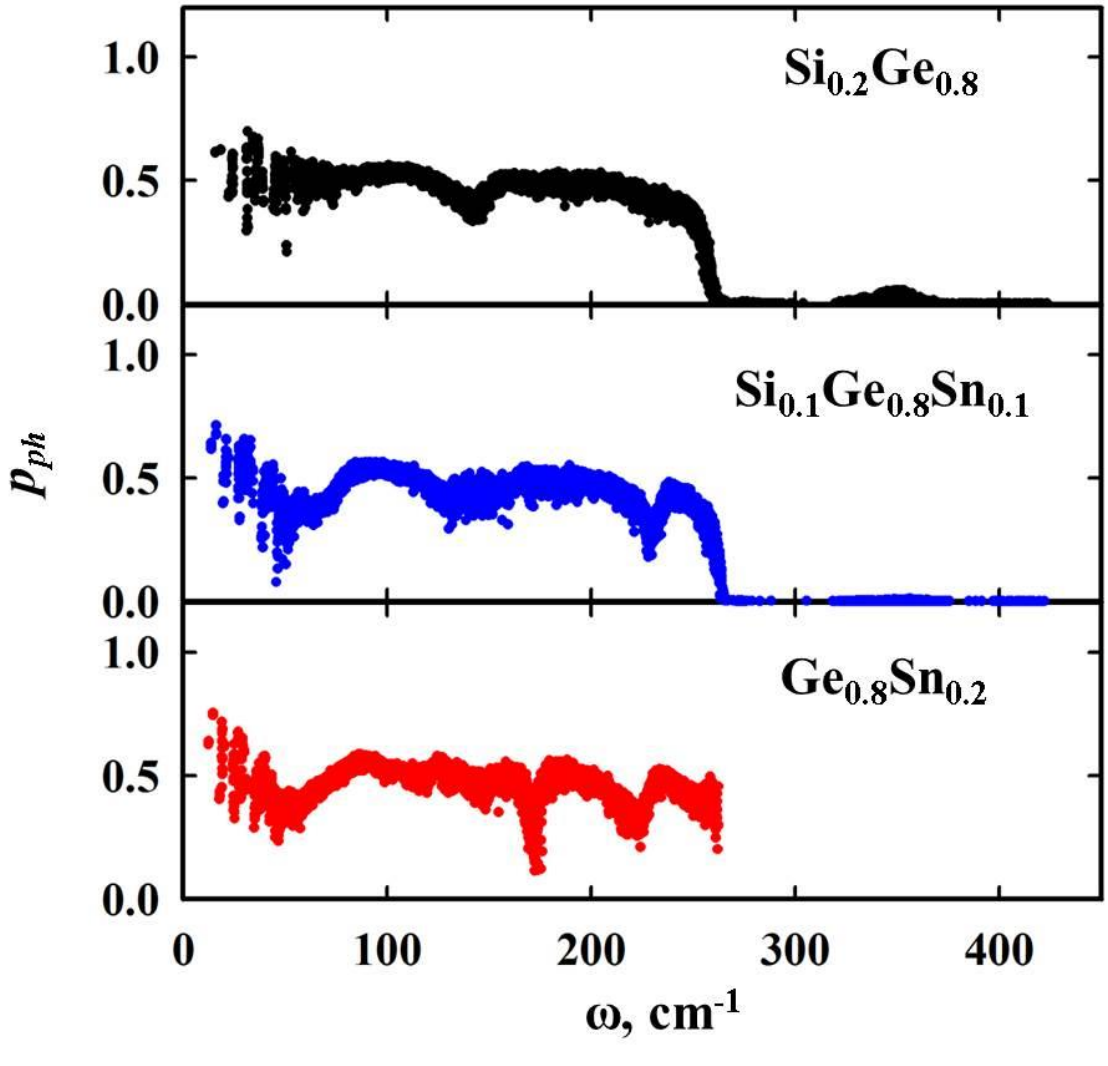

Figure 4.13: Phonon participation ratio (p_{ph}) for $Si_{0.2}Ge_{0.8}$, $Si_{0.1}Ge_{0.8}Sn_{0.1}$, and $Ge_{0.8}Sn_{0.2}$ alloys.

In Fig 4.13, p_{ph} for $Si_{0.2}Ge_{0.8}$, $Si_{0.1}Ge_{0.8}Sn_{0.1}$, and $Ge_{0.8}Sn_{0.2}$ are shown. Compared to p_{ph} for $Si_{0.2}Ge_{0.8}$, existence of heavier Sn significantly suppresses the p_{ph} of longer range modes below 100 cm^{-1} in $Si_{0.1}Ge_{0.8}Sn_{0.1}$. In addition, the p_{ph} around 150 cm^{-1} and over 300 cm^{-1} is more reduced, and the localization of phonon modes at about 230 cm^{-1} (corresponding to Ge-Sn vibrations) occurs, because of the additional mass disorder effect by Si-Sn, and Ge-Sn. Compared to p_{ph} for $Ge_{0.8}Sn_{0.2}$, alloying with lighter Si causes significantly localized phonon modes over 300 cm^{-1} due to the mass disorder effects Si-Ge and Si-Sn. Overall, it is clearly shown that the p_{ph} for $Si_{0.1}Ge_{0.8}Sn_{0.1}$ shows the characteristics integrating the p_{ph} for the $Si_{0.2}Ge_{0.8}$ and $Ge_{0.8}Sn_{0.2}$ alloys.

Next, building on the knowledge that the κ of SiGeSn might have the minimum value at a given Ge content when Si and Sn have the same contents, we investigated how κ is changed by increasing the Si and Sn amounts more even out of the currently experimentally feasible composition range. We calculated the κ of $Si_xGe_{1-2x}Sn_x$ as a function of x in the range of $0.1 < x < 0.5$. Predicted κ values are summarized in Table 4.4, together with alloy scattering strengths ($\Gamma = \sum_i x_i \left(\frac{M_i - M}{M} \right)^2$) for each composition.

Our calculations predict the κ of $Si_xGe_{1-2x}Sn_x$ to decrease monotonically with x as a result of the increase of Γ, suggesting enhancement of mass disorder induced-scattering of phonons. For example, when the Si, Ge, Sn contents are identical (x = 1/3), κ is about three times smaller than that of $Si_{0.1}Ge_{0.8}Sn_{0.1}$ because of a larger number of hetero-atom pairs. However, interestingly, when x is increased more than 1/3, the κ of $Si_xGe_{1-2x}Sn_x$ decreases more and is predicted to be minimum for $Si_{0.5}Sn_{0.5}$ (x = 0.5) even though only the mass difference between Si and Sn exists. This result may be attributed to the stronger mass disorder between Si and Sn ($|\Delta m_{Si\text{-}Ge}| = 90.63$) than $|\Delta m_{Si\text{-}Ge}| = 44.53$ and $|\Delta m_{Sn\text{-}Ge}| = 46.1$, as shown in Table 4.4; the strength of alloy scattering Γ is predicted to be the strongest in $Si_{0.5}Sn_{0.5}$.

Table 4.4: Calculated thermal conductivities (κ) of $Si_xGe_{1-2x}Sn_x$ alloys with alloy scattering strength $\Gamma = \sum_i x_i \left(\frac{M_i - M}{M} \right)^2$ where x_i is composition ratio for component i, M_i is mass for component i, and M is the total mass of alloys.

$Si_xGe_{1-2x}Sn_x$	κ ($Wm^{-1}K^{-1}$)	$\Gamma = \sum x_i (\frac{M_i - M}{M})^2$
0.1	1.7913±0.2415	0.0786
0.2	1.0494±0.1351	0.156
1/3	0.5452±0.0837	0.2574
0.4	0.5021±0.0977	0.3073
0.5	0.4266±#0.0684	0.3812

Chapter 5 Heat transport in Silicon-based Nanostructures

5.1 Introduction

Si-based materials as a candidate for TE applications have been extensively investigated. To develop high performance TE materials, much research has been directed towards finding ways to reduce the κ of Si-based materials by enhancing phonon scattering. One promising approach is nanostructuring.

Making Si-based materials into nanowires is one approach. SiNWs have κ about one or two orders of magnitude smaller than bulk Si [68, 192-195] due to the strong surface inelastic scattering of phonons. Hence, the ZT values of SiNWs could be enhanced close to 0.5~1 at room temperature [192,193], compared to the ZT of 0.01 ~ 0.06 in bulk Si [116,196]. Because SiNWs are not yet efficient enough to be commercially competitive, it is a continuing challenge to reduce the κ of NW further in order to achieve higher TE performance. One possible way to achieve this is to increase phonon scattering at surfaces by modifying NWs' surface structures; for instance, a significant reduction in κ was observed in NWs when their surfaces are amorphorized [68], faceted[197], corrugated [198], and chemically functionalized or branched [199]. The recent study by Hochbaum et al. [192] suggested that the surface structure and roughness, in particular, may also be a significant factor in determining the κ of SiNWs. Much lower values of κ were measured for electrolessly etched (EE) wires [192] with the same diameter as those studied in Ref. [200]. Also, the differences between the conductivities of EE wires obtained under different preparation conditions were reported [201]. Several models and simulations [68, 202-207] have provided a general consensus that the surface structure may influence the κ of wires. While the important role played by surface roughness has been identified by several models, disagreement on whether the surface roughness alone may explain recent experiments opens up the necessity of further investigation about factors affecting the κ of SiNWs. Another promising approach to reduce the κ of SiNWs is making core-shell type NWs. Recently, several theoretical [208-211] and experimental [212,213] studies have reported the significantly reduced κ of core-shell NWs due to phonon scattering at the interface.

SiGe alloys have received much attention as one of the promising candidates for thermoelectric (TE) energy conversion, due to their low κ, as compared to pure Si and Ge. One possible way to reduce further the κ of NWs in order to achieve higher TE performance is making SiGe alloys into NWs. Recently, it has been demonstrated that SiGeNWs exhibit much improved TE performance due to their lower κ compared to bulk SiGe. Previous experiments [214-217] reported that the κ decreases up to about 1~2.5 $Wm^{-1}K^{-1}$ as the Ge concentration increases. Recent theoretical studies [218,219] have demonstrated that these low κ values of $Si_{1-x}Ge_x$ NWs can lead to an improved ZT value. Although several theoretical studies [219,220] have been reported about the origin of the significant reduction of κ and the diameter and composition dependences of the κ of in $Si_{1-x}Ge_x$ NWs, it is not yet fully clarified the relative effects of surface and alloying-induced phonon scattering on thermal transport in $Si_{1-x}Ge_x$ NWs.

While previous studies have presumed single-crystalline structures, most nanomaterials may contain grains in practice. When grains meet, grain boundaries are formed and the material is described as polycrystalline. The issues of grain size and boundaries are very important in the study of heat transport since the grain boundaries can scatter energy carriers and impede thermal transport. However, very little work has been done on the thermal transport properties of polycrystalline materials, and even their structural properties still remain poorly understood.

In this chapter, we present a systematic theoretical analysis of thermal transport in various Si-based nanostructures. First, we report atomistic simulations of heat transport in SiNWs, focusing on the effect of surface structure, composition by designing NW samples with tailored morphologies. Next, we propose a new concept of core-shell NWs utilizing the SiGe alloy, and investigate the effect of SiGe alloy shell on thermal transport in core-shell NWs. Also, we present the relative effect of alloying and surface phonon scattering on the reduction of κ using NEMD with the SW[25] potential model. Lastly, we report a new method to generate polycrystalline Si/SiGe structures by modifying our in-house Monte Carlo code, and investigate the effect of grain boundaries on κ.

5.2 Thermal Conductivity of Oxide-Sheathed Silicon Nanowires

We have performed NEMD simulations to predict the κ of oxide-sheathed Si NWs. We used the SW potential for describing the interactions for Si-Si, Si-O[221], O-O[221], and Si-H[222]. We have focused our investigation on three SiNW orientations:

<100>, <110>, and <111>, guided by the results of previous theoretical studies [223,224] and reports of commonly synthesized SiNWs[225,226]. For reference, hydrogen-terminated SiNWs (*H*-SiNWs) were constructed by extracting sections of bulk *c*-Si with a DFT-optimized lattice constant of 5.460 Å followed by manual termination of surface dangling bonds with –H. Oxidized SiNWs ($a\text{-}SiO_x$-SiNWs) were generated using a procedure based on continuous random network model-based Metropolis Monte Carlo (CRN-MMC) simulations with the Keating-like potential optimized with the aid of density functional theory (DFT) calculations [227]. Starting from the same c-Si cores as previous described, O atoms strategically were inserted between surface Si-Si bonds. Then, the oxide sheath layers were amorphorized. Figure 5.1 illustrates all $a\text{-}SiO_x$-SiNWs and *H*-SiNWs used in our calculations. In Table 5.1, structural information about each SiNW is summarized. Diameter for $a\text{-}SiO_x$-SiNW and *H*-SiNW was determined from the volume (V) and length (L) regarding NW as a cylindrical shape. The volume (V) is given by $V = V_{Si}\times(N_{Si} - N_O/2) + V_{SiO2}\times N_O/2$, where N_{Si} and N_O denote the number of Si and O atoms, respectively, and V_{Si} and V_{SiO2} represent the unit volume of *a*-SiO_2 and *a*-SiO_2, respectively. V_{Si} and V_{SiO2} are extracted from the corresponding densities of 2.28 g/cm^3 [228] and 2.2 g/cm^3 [229], respectively.

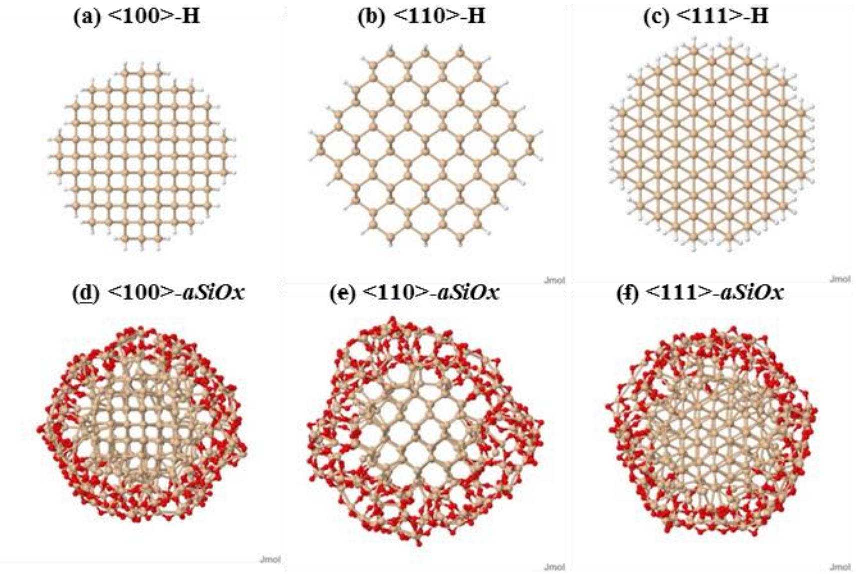

Figure 5.1: Configurational cross sections for each SiNW orientation in both H-passivated(a-c) and corresponding oxidized(d-f)states.

Table 5.1: Structural information of SiNWs. N, N_{Si}, N_O, or N_H denotes the number of total atom, Si, O, or H, respectively. D and L represents diameter and length of nanowires.

SiNW	N	N_{Si}	N_O	N_H	D(nm)	L(nm)
<100>-*H*	17024	11392		5632	1.7887	69.8201
<110>-*H*	13824	10240		3584	2.1112	49.3705
<111>-*H*	15104	10880		4224	1.9434	60.4656
<100>-*a-SiO$_x$*	20864	11392	9472		2.6018	66.0188
<110>-*a-SiO$_x$*	21248	10240	11008		2.9848	49.3705
<111>-*a-SiO$_x$*	19904	10880	9024		2.6741	59.6401

Table 5.2: Thermal conductivities of SiNWs in H-passivated (-H) or oxidized (-*a*-SiO_x) states for three orientation <100>, <110>, and <111>.

	<100>-NW	<110>-NW	<111>-NW
-H	4.224 ± 0.422 $Wm^{-1}K^{-1}$	11.098 ± 1.054 $Wm^{-1}K^{-1}$	5.774 ± 0.341 $Wm^{-1}K^{-1}$
-*a*-SiO_x	1.306 ± 0.088 $Wm^{-1}K^{-1}$	1.372 ± 0.063 $Wm^{-1}K^{-1}$	1.561 ± 0.092 $Wm^{-1}K^{-1}$

First, we studied the effects of –*a-SiO*$_x$ surface layer on the κ of SiNWs with comparison to the results of *H*-SiNWs. For κ calculations, we prepared NEMD simulation cells by repeatedly expanding previously generated NW structures along the axial direction. The calculation results are summarized in Table 5.2. For all orientations, the –*a-SiO*$_x$ passivation significantly reduces the κ of NWs compared to the –*H* terminated case; the reductions are 87.6, 69.1, and 72.9% for the <110>, <100>, <111> orientations, respectively.

To better understand the oxidation effect, we investigated the phonon density of states (PDOS) for NWs examined. The PDOS was calculated using the harmonic approach in which the hessian matrix elements were obtained by numerical differences of the analytical gradients, with a displacement of 0.02 Å for each atomic cartesian coordinate. With diagonalization of the hessian matrix, we obtained eigenvalues for lattice vibrational modes. We employed a local smoothing technique using polynomial regression and weights computed from the Gaussian density function.

Figure 5.2 shows PDOS for all four SiNW orientations that are illustrated in Figure 5.1. For the PDOS of bulk *c*-Si, there are characteristic sharp peaks around 200, 350, 450, and 520 cm^{-1}. Although each population of these peaks from c-Si is changed in *H*-SiNWs, the PDOS still has *c*-Si like characteristic. For *H*-SiNWs, an additional peak around 1700 cm^{-1} is observed, which can be attributed to the motion of Si-H bonds; note that phonon modes of this peak don't participate in the main scattering mechanisms of phonons due to their large frequency gap and extremely short wavelength.

Unlike the *H*-termination case, when NW surfaces are oxidized, the distinguished peaks originating from *c*-Si are reduced, and the PDOS for core *c*-Si becomes evenly distributed in the region below 600 cm^{-1}. This change is because the growth of the *a*-SiO_x surface layer creates strain in the *c-Si* NW core and disorder; the *c-Si/a*-SiO_x interface can be viewed as incipient amorphization of the *c-Si* core.[230] There also exist broad peaks above 700 cm^{-1} due to the oxidized surface layer.

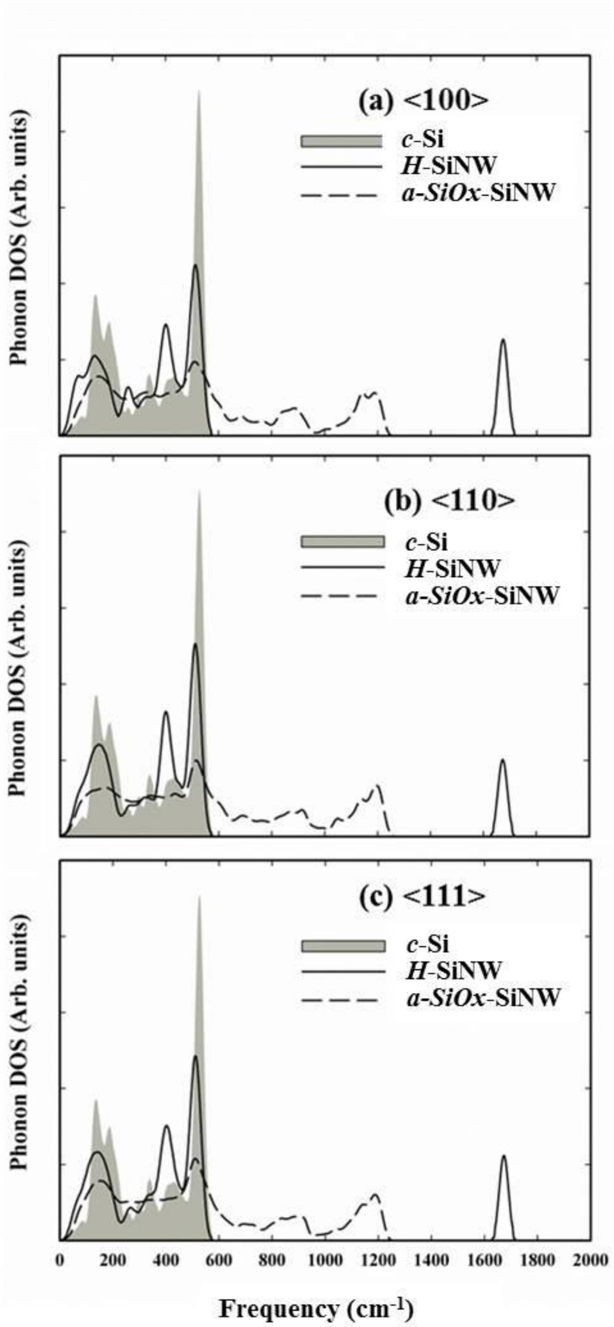

Figure 5.2: Phonon density of state (DOS) for SiNW in H-passivated (*H*-SiNW) or oxidized (*a-SiO$_x$*-SiNW) states, in comparison that of bulk c-Si, for (a) <100>, (b) <110>, and <111> orientations.

Interestingly, we observed that the orientation dependence of κ in *a-SiO$_x$*-SiNWs becomes insignificant compared to in the case of *H*-SiNWs. In our calculations, as shown in Table 5.2., <110>-*H*-SiNW has significantly larger κ than <100> and <111> NW, which is consistent with previous theoretical observations stating that the thermal conductance shows strong anisotropicity, i.e., the <110> direction shows 50% and 75% larger conductance than the <100> and <111> directions [231]. However, *a-SiO$_x$*-SiNWs exhibit no significant orientation dependence of κ.

To investigate this difference, we examined the transmission characteristics of phonons using the NEGF approach[105,106]. As shown in Figure 5.3(a), <110>-*H*-SiNWs has a significantly larger transmission at most frequencies, while <100>- and <111>-*H*-SiNWs have approximately the same transmission. However, from the results in Fig 5.3(b), we can observe that transmissions at most frequencies become nearly identical in the case of *a-SiO$_2$*-SiNWs.

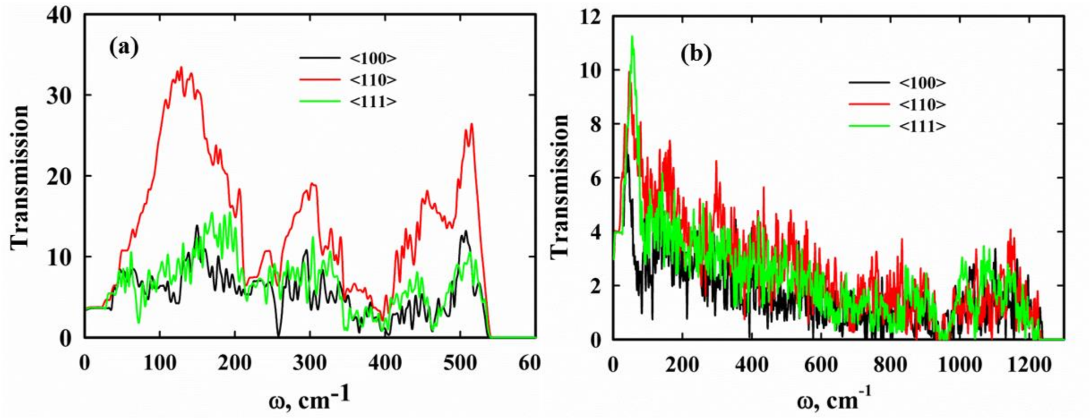

Figure 5.3: Frequency-dependent transmission functions for (a) –H terminated NWs and (b) –*a*-SiO$_x$ NWs with different orientations calculated using the non-equilibrium green function formalism (NEGF).

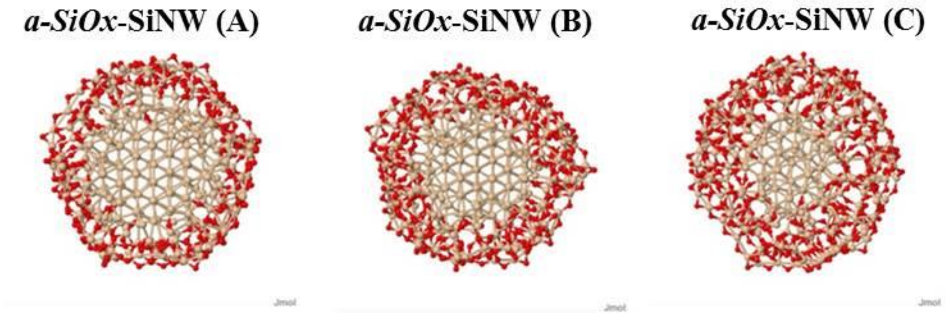

Figure 5.4: Configurational cross sections for *a-SiO$_x$*-SiNW with different thickness of oxide sheath. All NWs are in <111> orientations. N_{Si} : N_O is 10880:9024, 10880:11328, or 10880:13632 for *a-SiO$_x$*-SiNW(A), *a-SiO$_x$*-SiNW(B), or *a-SiO$_x$*-SiNW(C), respectively.

Next, we attempted to examine the variations of κ in *a-SiO$_x$*-SiNWs with oxide sheath thickness. Using the procedures employed in the previous sections, we prepared unit structures for *a-SiO$_x$*-SiNWs with different oxide thicknesses by increasing the number of oxygen atoms inserted. The structures considered are shown in Figure 5.4.

For NEMD calculations, unit structures were expanded along the axial direction. Our NEMD calculations predict that the κ of *a-SiO$_x$*-SiNWs monotonically decreases as the oxide sheath thickness increases; 1.674±0.052, 1.451±0.034, and 1.312±0.027 $Wm^{-1}K^{-1}$ for *a-SiO$_x$*-SiNWs(A), *a-SiO$_x$*-SiNWs(B), and *a-SiO$_x$*-SiNWs(C), respectively. This result suggests that an increase in oxidation may further reduce the κ of *a-SiO$_x$*-SiNWs. From PDOS in Figure 5.5, further SiNW oxidation indeed makes the PDOS for the *c*-Si core broader and more evenly-distributed, leading to stronger phonon scattering. Also, the peak around 1200 cm^{-1} for the oxidized layer near surface and the peaks around

700~800 cm^{-1} for the oxidized layer near interface become prominent, which suggests existence of stronger surface and interface phonon scattering.

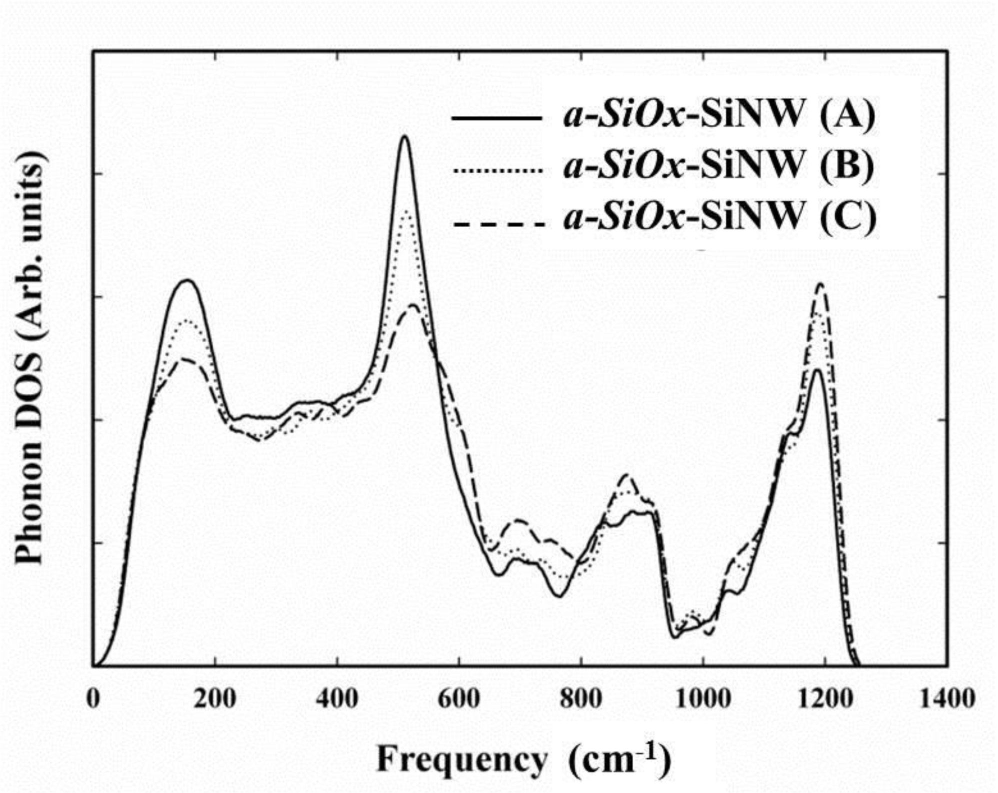

Figure 5.5: Phonon density of states (DOS) for $a\text{-}SiO_x$-SiNW(A), $a\text{-}SiO_x$-SiNW(B), or $a\text{-}SiO_x$-SiNW(C).

The suppression of κ due to surface oxidation can be attributed to a combination of diminished transcalent *c*-Si part (area effect), passivation of surface phonon modes in *c*-Si NW (surface passivation effect), and increased strain of core part (strained core effect). We discuss the relative contributions of these three effects to the κ suppression in $a\text{-}SiO_x$-SiNWs. In order to decouple three factors, we prepared several model samples and calculated their κ values using NEMD.

Provided that the surface passivation and strained core effects are negligible, the κ of <111>–*a-SiO$_x$*-SiNWs can be approximated as an effective thermal conductivity (κ_{eff}) according to the following relation; $\kappa_{eff} = \frac{S_{a-SiOx}}{S_{total}} \times \kappa_{a-SiOx\,NW} + \frac{S_{Si}}{S_{total}} \times \kappa_{Si\,NW}$ where $S_{a\text{-SiOx}}$, S_{Si}, and S_{total} represent the cross-sectional areas of a-SiO$_x$ shell, Si core, and entire NW, respectively. $\kappa_{a\text{-SiOx NW}}$ denotes the κ of a-SiO$_2$ NWs, which is predicted to be 1.454 ± 0.185 Wm^{-1}K^{-1} at D = 3.133 nm from our NEMD calculations. $\kappa_{\text{Si NW}}$ denotes the κ of Si NWs (NW(A)_Core, NW(B)_Core, or NW(C)_Core) with the samediameters as the core parts of <111>–*a-SiO$_x$*-SiNWs(A), SiNWs(B), or SiNWs(C), respectively. For the κ calculations, surface Si atoms were terminated with H atoms, as shown in Fig 5.6. Our NEMD simulations predict the κof NW(A)_Core, NW(B)_Core, and NW(C)_Core to be 6.483± 0.785, 5.595± 0.653, and 7.422 ± 0.973 Wm^{-1}K^{-1}, respectively.

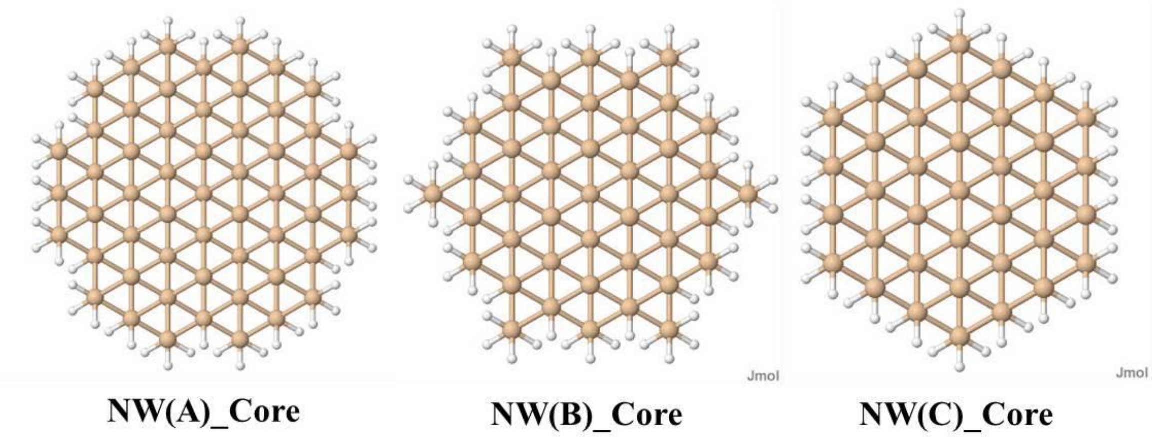

Figure 5.6: Configurational cross sections for H-SiNW (NW(A)_Core, NW(B)_Core, or NW(C)_Core) which corresponds to core part in *a-SiO$_x$*-SiNW(A), *a-SiO$_x$*-SiNW(B), or *a-SiO$_x$*-SiNW(C), respectively.

Also, in order to exclude the strained core effect, we prepared <111>–*a-SiO$_x$*-SiNWs(NW_A, NW_B, or NW_C) with strain free cores, as shown in Fig 5.7. Each NW has the same fraction of Si/O atoms as <111>–*a-SiO$_x$*-SiNWs(A), SiNWs(B), or SiNWs(C), respectively.

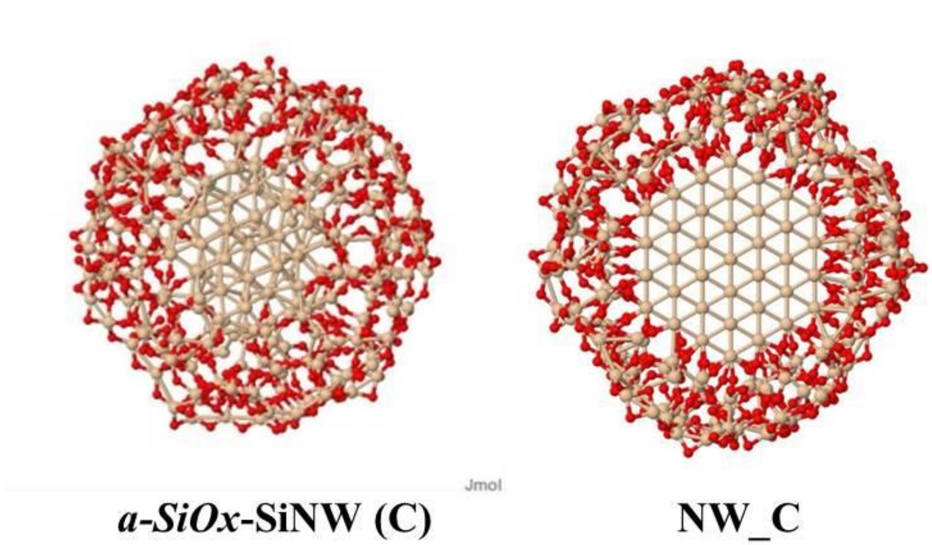

a-SiOx-SiNW (C)   **NW_C**

Figure 5.7: Configurational cross sections for *a-SiO$_x$*-SiNW(C) and a model NW which has the unstained core part. Both NWs have the same ratio of N_{Si} : N_O = 10880:13632.

Our calculation results are summarized in Table 5.3. We find that the area effect due to the diminished c-Si part is the main factor for the reduction of κ in *a-SiO$_x$*-SiNWs, compared to *H*-SiNWs; this effect accounts for about 70~80 % of the total reduction in surface passivated NWs compared to *H*-SiNWs. In addition, about 10~20 % of the total reduction is attributed to suppression of surface phonons modes of *H*-SiNW, due to the presence of *a-SiO$_x$* shell. It is noteworthy that the increased strain of the core part due to surface passivation causes an additional (about 10%) reduction in κ.

Table 5.3: Summary of the contributions to reduction in thermal conductivities of *a*-SiO_x-SiNWs. Area effect, surface passivation effect, or stain effect is defined as $\Delta(\kappa_{H\text{-}SiNW} - \kappa_{eff}) / \Delta\kappa_{total}$, $\Delta(\kappa_{eff} - \kappa_{strain\ free}) / \Delta\kappa_{total}$, or $\Delta(\kappa_{strain\ free} - \kappa_{a\text{-}SiOx\text{-}SiNW}) / \Delta\kappa_{total}$, respectively. $\Delta\kappa_{total}$ is $(\kappa_{H\text{-}SiNW} - \kappa_{a\text{-}SiOx\text{-}SiNW})$. $\kappa_{strain\ free}$ corresponds to thermal conductivity of *a-SiO*$_x$-SiNWs having unstrained core part.

	Area effect	Surface passivation effect	Strain effect
a-SiO$_x$-SiNWs(A)	0.707	0.206	0.087
a-SiO$_x$-SiNWs(B)	0.802	0.127	0.071
a-SiO$_x$-SiNWs(C)	0.745	0.191	0.064

5.3 Relative Contribution of Alloy and Boundary Scattering to Thermal Conductivity Reduction in Silicon Germanium Alloy Nanowires (SiGeNW)

To understand the alloying and boundary scattering effects on the κ of SiGeNWs, NEMD simulations were performed using LAMMPS with a time step of 0.5 *fs*. The heat flux was imposed in the *z* direction by adding (subtracting) nontranslational kinetic energy to a group of atoms in the heat source (sink) layer.

To describe atomic interactions, we used a general form of SW potential function[25] with re-adjusted the SW parameters. The κ of NWs was obtained by extrapolating finite-size results to infinite size and all κ values reported hereafter are after quantum corrections, unless stated otherwise. For each of the NW systems considered, five independent NEMD simulations were performed with different atomic arrangements and initial velocity distributions.

For κ calculations, we prepared NWs with different diameters and alloy composition. First, reference SiNWs with round cross section were constructed by extracting sections of bulk *c*-Si with a DFT-optimized lattice constant of 5.4571 Å. SiNWs are oriented along the [100] direction with diameter d = 3.235, 6.415, 9.705, and 12.94 nm. To construct SiGeNWs, Si atoms were randomly replaced with Ge atoms with Ge content = 1, 5, or 20 %. The lattice parameter of each NW was set according to Vergard's law which is a linear interpolation between the lattice constant a_{Si}(= 5.4571 Å) for Si and a_{Ge}(= 5.7587 Å) for germanium from the DFT calculation. All NWs were fully relaxed so as to reconstruct the surface for 1 ns MD run at 300K.

First, in order to check the validity of investigating boundary scattering effect by MD, we investigated dependence of κ of Si NWs on diameters of NWs at 300 K. NWs at four different diameters (3.235, 6.415, 9.705, and 12.94 nm) were employed. Calculated κ values for Si NWs are shown in Fig 5.8, in comparison with experimental data. At diameters investigated, κ is significantly reduced due to strong boundary scattering effect [200]. And as D decreases, κ is more reduced, because boundary scattering effect is inversely proportional to D; from D = 3.235 to D = 12.94 nm, SiNW has κ = 3.867 ~ 11.123 $Wm^{-1}K^{-1}$. At D = 3.235 nm, κ/κ_{Si} is only 0.0283. Our MD results show same trend of dependency on D, with previous experimental data. And MD results are located between previous theoretical predictions; note each model has different boundary scattering lifetime: $\tau_b = D/v$ for Mingo model [232] : $\tau_b = (4D/(3\pi|\cos\theta|))/v$ for McGaughey model [233].

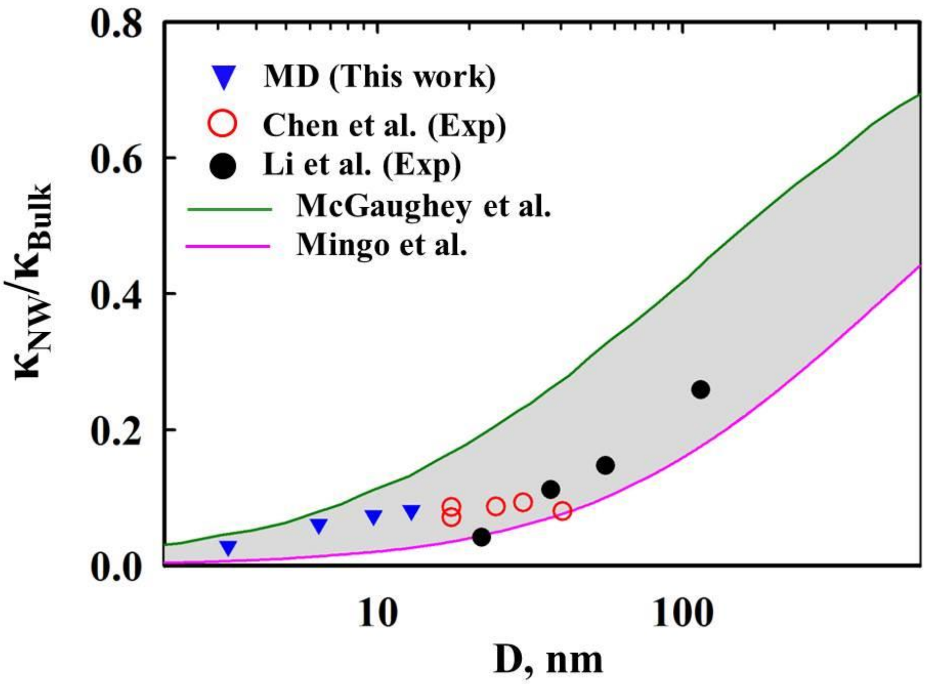

Figure 5.8: Normalized thermal conductivities ($\kappa_{NW}/\kappa_{Bulk}$) as a function of diameter (D) of nanowires. κ_{Bulk} corresponds to the κ of bulk Si from previous MD study (= 136.65 $Wm^{-1}K^{-1}$[71]) or experimental data (= 156.38 $Wm^{-1}K^{-1}$[165]). Inversed blue triangles correspond to our MD calculation results. Open red or filled black circle are previous experimental data[200,234]; note open red circle data was obtained from thermal conductance (G) data with the relation of $\kappa = G \times L/A$ where L is NW length and A is crossectional area. Green and pink lines represent previous theoretical predictions.

Next, we investigated boundary scattering effect in SiGeNWs. For SiGeNWs, the rectangular-shaped simulation domains were employed with a cross section of 10×10 units in the <110> direction and an axial length of 122, 202, 282, and 362 units in the <100> direction. Periodic boundary conditions are imposed in the axial (z) direction which is heat conduction direction. Cells are axially divided into a number of thin shells each of which is one-unit thick corresponding to 400 atoms. The heat source and heat sink layers are one-unit thick. For NW systems, Si and Ge atoms were randomly distributed. Following Vegard's law, the lattice parameter of $Si_{1-x}Ge_x$ (a_{SiGe}) was approximated using linear interpolation between the Si and Ge lattice constants (from DFT-GGA calculations), i.e, $a_{SiGe} = (1-x)a_{Si} + xa_{Ge}$, where a_{Si} = 5.4571 (or 3.8587) Å and a_{Ge} = 5.7564 (or 4.0703) Å along the <100> (or <110>) direction. Subsequently the rectangular-shaped simulation cells were fully relaxed, which is so as to anneal the surface for NWs.

Figure 5.9 shows calculated thermal conductivities of $Si_{1-x}Ge_x$ alloy NWs as a function of Ge content x. Our results show that the thermal conduction in SiGeNW is significantly impeded with increasing the impurity (Si in Ge hosts or Ge in Si hosts) content. κ rapidly decreases as Si and Ge are alloyed, and nearly falls to a valley plateau between 20 ~ 80 % of Ge. Between 20 ~ 80 % of Ge, thermal conductivities of $Si_{1-x}Ge_x$ alloy NWs were estimated to range between 1-2 $Wm^{-1}K^{-1}$. At $x = 0.2$, the lowest κ occurs and it is about one order of magnitude smaller than that of Si NW. This dependence of κ on the impurity content is similar to previous studies[214,217], demonstrating the reduction is attributed to strong alloy scattering.

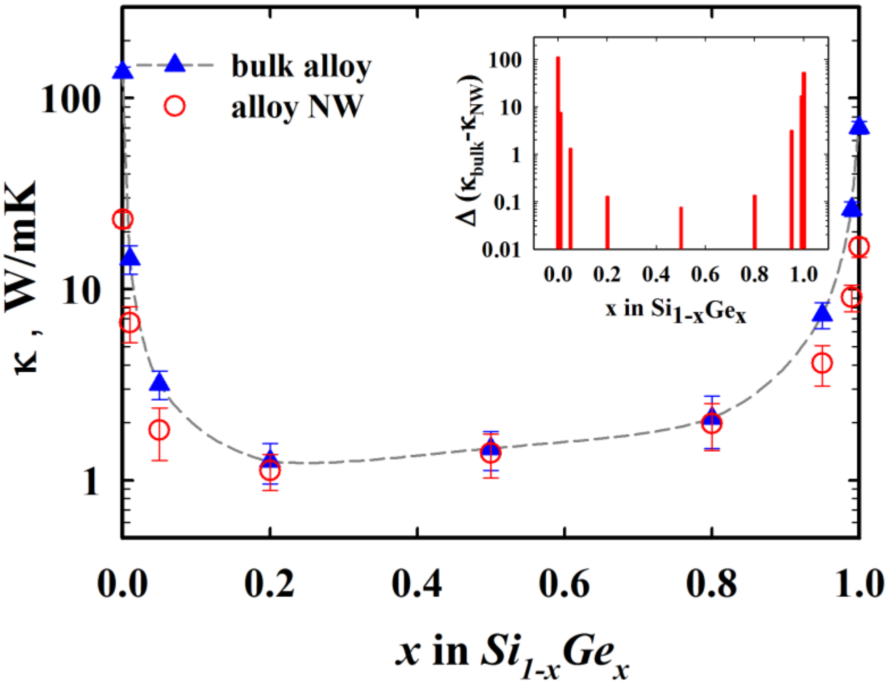

Figure 5.9: Calculated thermal conductivities (κ) of $Si_{1-x}Ge_x$ alloy nanowires and bulk $Si_{1-x}Ge_x$ alloys at 300K. Open red circles show the κ values for alloy NWs from this work, while solid blue triangles indicates the κ values for bulk alloys from our previous NEMD simulations[35]. The inset shows the differences of κ between alloy NW and bulk alloy.

One interesting aspect of our results lies in comparing the κ of SiGeNW and bulk[35] at the same Ge content. As shown in Fig. 5.9, at x = 0 or x = 1 (i.e. pure Si or Ge NW), NWs have about 83% or 76% reduced thermal conductivities compared to the corresponding bulk systems, respectively. However, as the impurity content increases, the bulk vs. NW difference in κ becomes smaller. Especially, for 20 ~ 80 % of Ge, the SiGeNW has the almost same κ value as the bulk crystalline; see the inset that shows the differences of κ ($\Delta\kappa = \kappa_{bulk} - \kappa_{NW}$) between the NW and the bulk systems.

According to Matthiessen's rule, the total phonon scattering rate (τ^{-1}) can be expressed as the sum of alloy (τ_a^{-1}), boundary (τ_b^{-1}), and intrinsic (predominantly phonon-phonon (τ_{p-p}^{-1}) in SiGe) contributions. Hence, the scattering rates for NW is given by $\tau_{NW}^{-1} = \tau_a^{-1} + \tau_b^{-1} + \tau_{p-p}^{-1}$. The magnitude of phonon-phonon scattering is insignificant compared to those of alloy and boundary scatterings in SiGe NW[57,200]. Therefore, our calculations indicate that thermal conduction is significant retarded by mainly alloy scattering when $\tau_a^{-1} \gg \tau_b^{-1}$.

To better understand the relative contribution of the boundary and alloy scattering effects, we examined transmission characteristics of phonons using the NEGF approach[105,106]. Here, we ignore nonlinear phonon-phonon scatterings, as our primary concern was to understand the relative contribution between alloy and boundary scatterings. Here, the dynamic matrices were obtained from the second derivative of the SW(GGA) potential energy surface with a displacement of 0.02 Å. Within the NEGF framework, each calculation system consists of a central scattering region (alloy or pure Si) and two semi-infinite Si leads.

Figure 5.10 shows the calculated phonon transmission coefficients (T_{ph}) for bulk Si, SiNW, bulk $Si_{0.8}Ge_{0.2}$, and $Si_{0.8}Ge_{0.2}$ NW, respectively. For bulk Si, there are some regular steps, indicating that all phonons from the lead can pass through the center region without any scattering. For SiNW, these highly transmitting modes of phonon are strongly suppressed by boundary scattering (significant reduction of T_{ph}) for the entire range of frequencies except for the low frequency regime ($\omega < 100$ cm^{-1}). On the other hand, phonon modes for bulk $Si_{0.8}Ge_{0.2}$ are not transmittable due to strong alloy scattering, compared to the bulk Si case. Therefore, the additional effect of $\mathcal{T}_{ph}$ from NWs is not significant for the most phonon modes, except when $\mathcal{T}_{ph}$ of $Si_{0.8}Ge_{0.2}$ NW below 100 cm^{-1} are shifted to lower frequencies. These result can be also supported by the comparisons of normalized σ; at 300K, $\sigma/A_{\text{bulk Si}} = 1.166 > \sigma/A_{\text{Si NW}} = 0.688$ and $\sigma/A_{\text{bulk Si0.8Ge0.2}} = 0.125 > \sigma/A_{\text{Si0.8Ge0.2 NW}} = 0.104$ $nWK^{-1}nm^{-2}$ where A is cross-sectional area for heat transport direction.

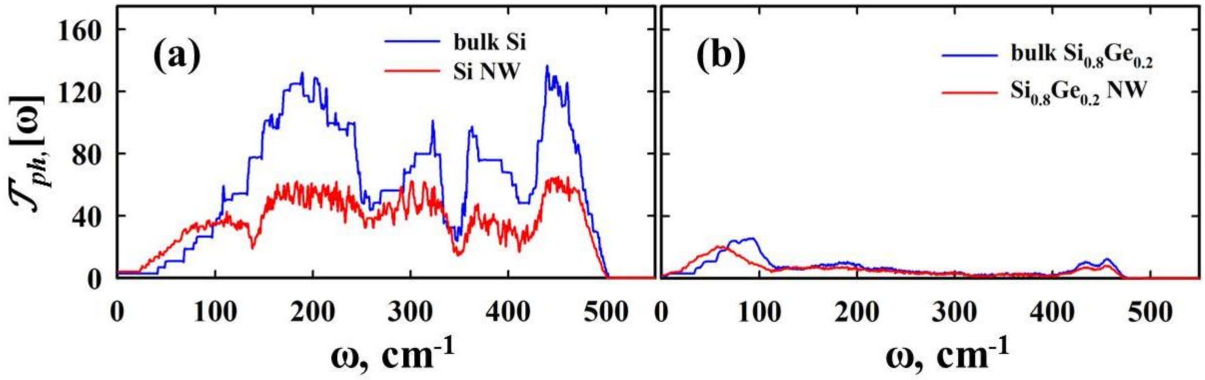

Figure 5.10: Frequency-dependent phonon transmission coefficients ($\mathcal{T}_{ph}$) calculated for (a) bulk Si and Si NW, and (b) bulk $Si_{0.8}Ge_{0.2}$ and $Si_{0.8}Ge_{0.2}$ NW.

5.4 Heat Transport in Core-Shell Nanowires

5.4.1 Alloying Effect in Core and Shell Regions

In order to investigate the effects of SiGe alloy shell and core on the κ of core-shell NWs, we prepared NWs and estimated their κ values, as shown in Fig.5.11. First, reference SiNWs (NW_{Si}) with round cross-section were constructed by extracting sections of bulk *c*-Si with a DFT-optimized lattice constant of 5.4571 Å. SiNWs are oriented along the [100] direction with diameter d = 3.235 and 6.415 nm. To construct core-shell NWs, we divided NW_{Si} into two concentric parts (core and shell parts) along the heat conduction direction. Each part has the same number of atoms. For Si-core/Ge-shell NW($NW_{Si/Ge}$), Si atoms in the shell part was replaced with Ge atoms. The Si-core/SiGe-shell NW ($NW_{Si/SiGe}$) was constructed with a SiGe alloy shell which has a random distribution of Ge atoms. The composition of the SiGe alloy part was chosen to be 20% ($NW_{Si/Si0.8Ge0.2}$) or 40 % Ge ($NW_{Si/Si0.6Ge0.4}$) because previous experimental [164,235,236] and theoretical studies [57,70] have demonstrated that alloy scattering becomes maximum in the composition range. For the SiGe-core/Si-shell NW($NW_{SiGe/Si}$), the core part was replaced with the $Si_{0.8}Ge_{0.2}$ or $Si_{0.6}Ge_{0.4}$ alloy, and surrounded by a Si shell. The lattice parameter of each NW was set according to Vergard's law which is a linear interpolation between the lattice constant a_{Si} (= 5.4571 Å) for Si and a_{Ge} (= 5.7587 Å) for Ge from DFT calculations. All NWs were fully relaxed so as to reconstruct the surface for 1 *ns* MD run at 300K.

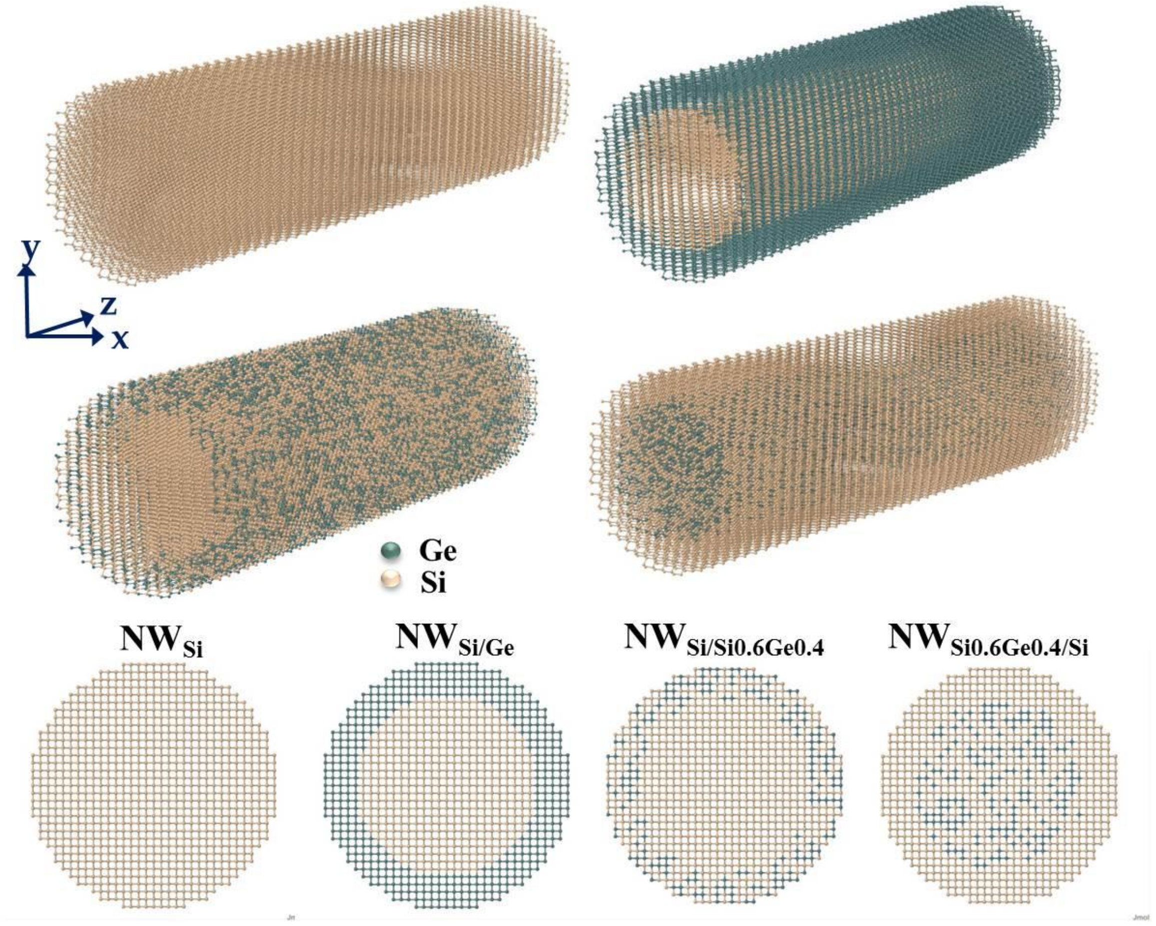

Figure 5.11: Configurations of Si, Si/Ge, Si/SiGe, and SiGe/Si nanowires. Heat conduction occurs along the *z* direction. The core and shell parts have the same number of atoms. For the alloy shells and cores, Ge atoms were randomly distributed at a desired concentration.

For NEMD calculations, we employed a general form of SW potential function with re-optimized parameters[35] for Si-Si, Si-Ge, and Ge-Ge. The simulation cell was divided with several layers including heat source and sink layers. A periodic boundary condition was imposed along the axial (heat flow) direction while fixed boundary conditions were in the cross-sectional directions. We calculated bulk κ values for NW structures at 300K through extrapolation of finite-size results to infinite size. For quantum correction, the Debye temperature was approximated by $T_D(\mathrm{Si}_{1-x}\mathrm{Ge}_x) = (1-x)T_D(\mathrm{Si}) + xT_D(\mathrm{Ge})$, where $T_D(\mathrm{Si}) = 645$ K and $T_D(\mathrm{Ge}) = 374$ K.

For the reference sake, we compared our results of SiNWs with previous studies. Our simulation results of 6.705 (uncorrected) $\mathrm{Wm^{-1}K^{-1}}$ for D = 3.235 nm and L = 176.62 nm SiNW are consistent with previously reported thermal conductivities of ~ 6 $\mathrm{Wm^{-1}K^{-1}}$ for the A = 5.29 $\mathrm{nm^2}$ and 150 nm long SiNW [237] from NEMD and 8.8 $\mathrm{Wm^{-1}K^{-1}}$ for the A = 4.72 $\mathrm{nm^2}$ SiNW from EMD. Also, in our study, the κ of D = 6.415 nm and L = 176.62 nm SiNW is estimated to be 15.526 (uncorrected) $\mathrm{Wm^{-1}K^{-1}}$ which is in excellent agreement withpreviously reported values (20.2$\mathrm{Wm^{-1}K^{-1}}$ for A = 21.16$\mathrm{nm^2}$ and L = 160nm [238] and 20 $\mathrm{Wm^{-1}K^{-1}}$ for A = 17.64 $\mathrm{nm^2}$ and L = 125 nm [67]). Considering that circular shaped-NWs have stronger surface scattering effects than rectangular shaped-NWs due to a larger surface-volume-ratio [239], our calculation results are quite consistent with previous MD results.

The calculated thermal conductivities for NWs are shown in Fig. 5.12. As demonstrated in previous studies [210,240], Si/Ge core-shell NWs ($\mathrm{NW_{Si/Ge}}$) turned out to have reduced κthan SiNW($\mathrm{NW_{Si}}$). $\mathrm{NW_{Si/Ge}}$ with D = 6.592 and $\mathrm{NW_{Si/Ge}}$ with D = 3.324 nm has about 43 % and 7 % reduced κ, in comparison to the case of $\mathrm{NW_{Si}}$, respectively. It is noteworthy that the reduction in κ is less significant for $\mathrm{NW_{Si/Ge}}$ with D = 3.324 nm, because the phonon-boundary scattering effect becomes stronger as D is smaller and it may dominate phonon scatterings in $\mathrm{NW_{Si/Ge}}$.

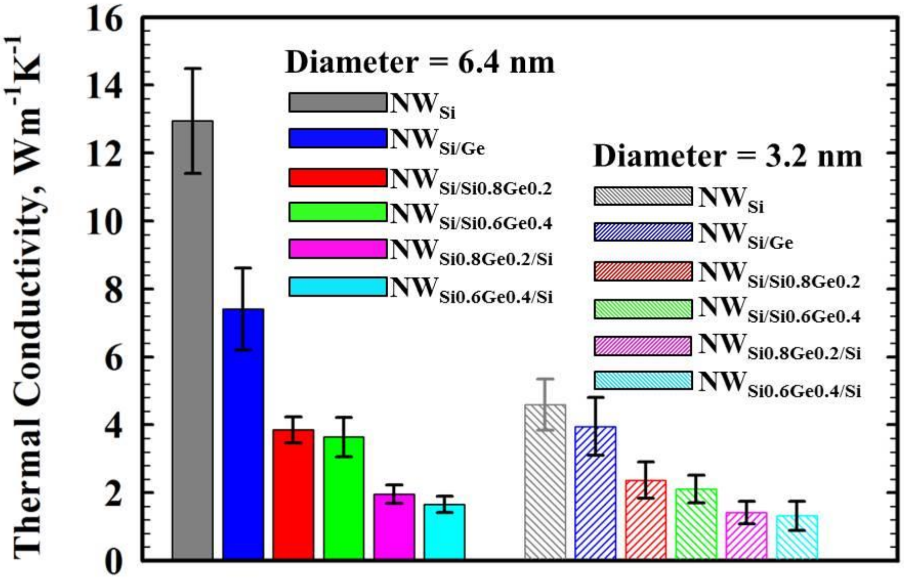

Figure 5.12: Calculated thermal conductivities (κ) for NWs. Solid colored bars correspond to κ values of NWs with D = 6.4 nm and patterned bars represent κ values of NWs with D = 3.2 nm. Two bars having same colors have the same atomic composition and same configuration (i.e. Si, Si/Ge, Si/SiGe, or SiGe/Si).

From our calculation results, we note that the κ of $NW_{Si/SiGe}$ and $NW_{SiGe/Si}$ is substantially smaller than that of $NW_{Si/Ge}$. For NWs with D = 6.415 nm, the reduction of κby alloying is about 50 % and 80 % for $NW_{Si/SiGe}$ and $NW_{SiGe/Si}$ with $Si_{0.6}Ge_{0.4}$ in the alloy regions, respectively. This reduction originates from the strong alloy scattering of phonons which increases heat transport resistivity in the SiGe part. For bulk SiGe alloys, the previously reported minimum κ values at 300K are about one or two orders of magnitude smaller than that of pure *c*-Si or *c*-Ge[164,168,165,235,236] due to significant alloy scattering. Therefore, strong alloy scattering in conjunction with surface scattering reduces significantly the κ of $NW_{Si/SiGe}$ and $NW_{SiGe/Si}$ compared to that of $NW_{Si/Ge}$.

As the D of $NW_{Si/SiGe}$ decreases, κ decreases due to enhanced boundary phonon scattering. However, because thermal conduction in NWs is highly impeded already by alloy scattering, the dependency of κ on D is not significant, compared to $NW_{Si/Ge}$ and NW_{Si}. Furthermore, for $NW_{Si/SiGe}$ (or $NW_{SiGe/Si}$) with D = 6.450 or 3.253 nm, κ is reduced only by 0.21(0.31) or 0.26(0.09) $Wm^{-1}K^{-1}$ when the Ge content in the alloy region increases from 20% to 40%, respectively. This result is consistent with previous studies [57,70] indicating that κ rapidly decreases as Si and Ge are alloyed, and nearly falls to a valley plateau between 20 ~ 80 % of Ge.An interesting aspect of our results lies in the comparison of κ between $NW_{SiGe/Si}$ and $NW_{Si/SiGe}$. With the same alloy composition and the same D of NW, $NW_{SiGe/Si}$ exhibits about 45~60% more reduced κ compared to $NW_{Si/SiGe}$.

To better understand the effect of SiGe alloy shell on thermal transport, detailed phonon studies were performed. Local vibrational density of states (LVDOS) was obtained by measuring the velocity autocorrelation function and taking a Fourier transform of it. LVDOS is given by $g(\omega) = \int_{-\infty}^{\infty} dt \frac{\langle v_i(t)|v_i(0)\rangle}{\langle v_i(0)|v_i(0)\rangle} e^{i\omega t}$ where v_i denotes the velocity of the *i*th atom of each part. The system was first equilibrated for 1.0 *ns* using the Nose-Hoover thermostat at 300K and the correlation value is calculated for every 3 *fs* and for a total time period of 12 *ps* in the micro-canonical ensemble (NVE).

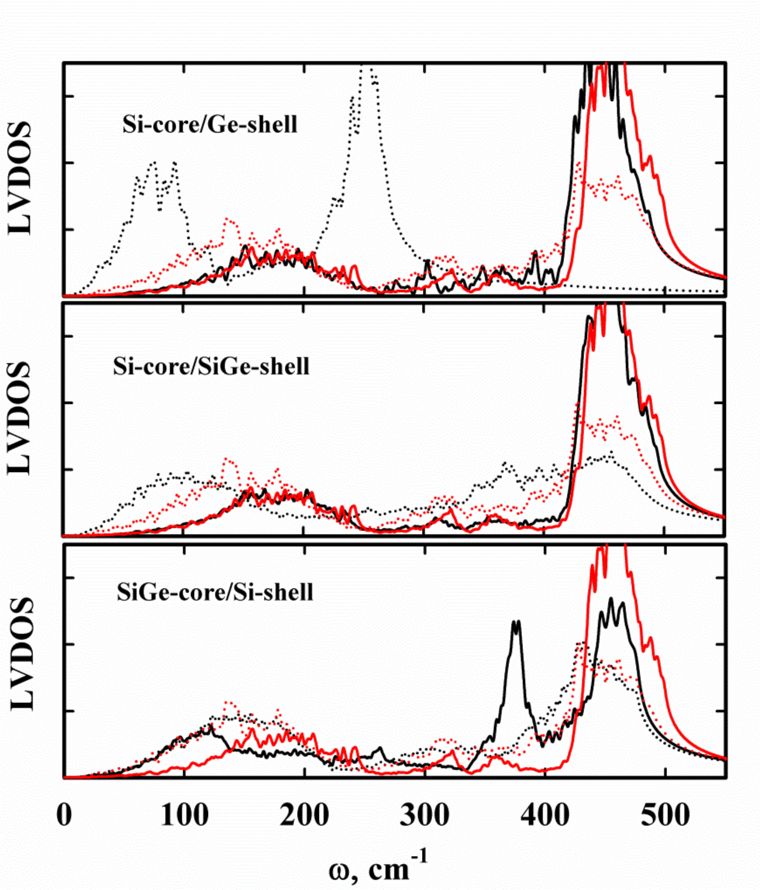

Figure 5.13: Local vibrational density of states (LVDOS) for $NW_{Si/Ge}$ (top), $NW_{Si/SiGe}$ (intermediate), and $NW_{SiGe/Si}$ (bottom); black solid and dotted lines indicate LVDOS for core and shell of each NW, respectively. Red solid and dotted lines indicates LVDOS for core and shell of NW_{Si}, respectively.

In Fig. 5.13, the results for LVDOS are shown. For the $NW_{Si/Ge}$ core, LVDOS differs little compared to that of NW_{Si} core which is analogous to bulk *c*-Si as shown in previous studies [241]. For the LVDOS of the shell, sharp peaks are observed corresponding to Ge characteristic modes. Therefore, this LVDOS for core and shell leads to the redshift of TO peaks due to depression in the PDOS of Si atoms near the core-shell interface upon existence of the Ge shell [210]. Also, for $NW_{Si/Ge}$, additional minor peaks (in the range of 300~400 cm^{-1}) are observed due to the lattice mismatch and the atomic mass difference between Si and Ge, which causes phonon interferences at the Si/Ge interface.

For $NW_{Si/SiGe}$, the LVDOS of the core part is also quite similar to that of NW_{Si}, regardless of the shell type. On the other hand, for the shell part, the large peak of transverse acoustic (TA) modes in the range centered around 180 cm^{-1} for NW_{Si} is shifted to lower frequencies (around 100cm^{-1}) due to lattice softening caused by alloying. Also, a pronounced transfer of weight from the transverse optical (TO) modes to intermediate frequencies is observed due to alloying, which indicates increased phonon scattering by alloying. It is noteworthy that compared to the LVDOS for the core part of $NW_{Si/Ge}$, minor peaks in the range of 250-400 cm^{-1} are not significant and the redshift of TO peak is negligible, which indicates the interface effect is unimportant because the lattice mismatch at the interfaces is not significant due to alloying.

For $NW_{SiGe/Si}$, the LVDOS of the core part is significantly different from that of $NW_{Si/Ge}$. Primary changes are twofold: (1) in 350 – 400 cm^{-1}, a distinct peak by Si-Ge vibrational modes, and a notable loss in the height of the TO mode peak due to alloying, and (2) a shift of the TA mode peak toward lower frequencies due to alloying-induced lattice softening. Meanwhile, the LVDOS of the shell part is nearly similar to that of NW_{Si} which shows the surface scattering effect. These results demonstrate that the differences of κ between $NW_{SiGe/Si}$ and $NW_{Si/SiGe}$ can be attributed to the fact that significant phonon scatterings occur in both core and shell regions through $NW_{SiGe/Si}$, while the phonons through the shell region are substantially scattered in $NW_{Si/SiGe}$.

5.4.2 Effect of Interfacial Atomic Arrangement on Thermal Conductivity of Core-Shell Nanowires

In order to investigate the effect of alloyed interfaces on the κ of Si/Ge core-shell NWs, samples ($NW_{Si/Ge,alloyed}$) with alloyed interfaces were generated using Monte Carlo (MC) simulations, as illustrated in Fig. 5.14. Initially, the $NW_{Si/Ge}$ structure ($NW_{Si/Ge,clear}$)an abrupt interface with D = 6.592 nm and Si:Ge = 50:50. After a number of MC steps, the fraction of Si-Ge bonds with respect to the total number of bonds for $NW_{Si/Ge,alloyed}$ was increased to 0.183 from 0.055 in $NW_{Si/Ge,clear}$.

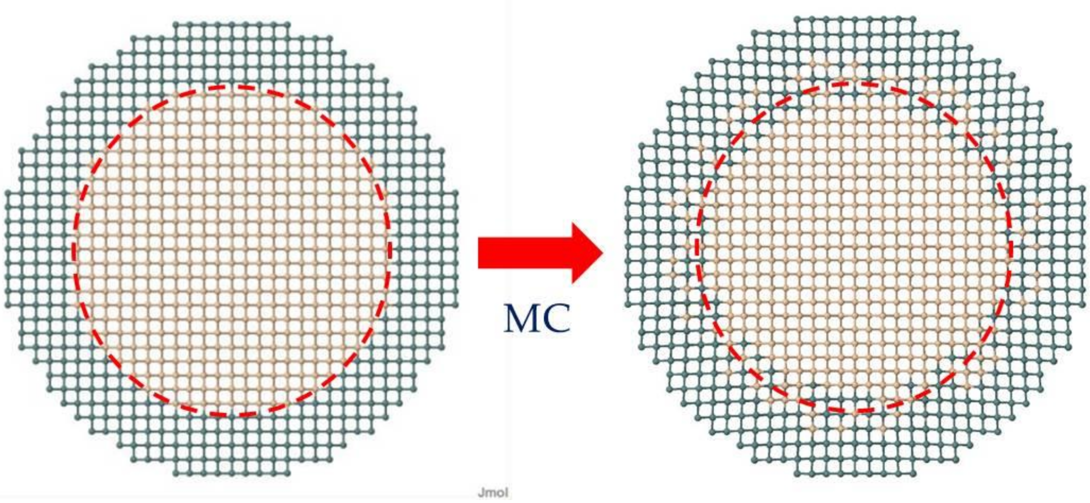

Figure 5.14: Schematic view of cross-sections of Si/Ge core-shell NW having clear (left) or alloyed (right) interface between core and shell. Using MC algorithm, interfacial regions were alloyed.

For NEMD calculations, the simulation cell was divided with several layers including heat source and sink layers. A periodic boundary condition was imposed along the axial (heat flow) direction while fixed boundary conditions were in the cross-sectional directions. We calculated κ values for NW structures at 300K through extrapolation of finite-size results to infinite size. For quantum correction, the Debye temperature was approximated by $T_D(\mathrm{Si}_{1-x}\mathrm{Ge}_x) = (1-x)T_D(\mathrm{Si}) + xT_D(\mathrm{Ge})$, where $T_D(\mathrm{Si})$ = 645 K and $T_D(\mathrm{Ge})$ = 374 K.

From our calculation results, we find that the κof $\mathrm{NW}_{\mathrm{Si/Ge,alloyed}}$ (= 3.43±0.83 $\mathrm{Wm^{-1}K^{-1}}$) is about a half of 7.41±1.21 $\mathrm{Wm^{-1}K^{-1}}$as predicted for $\mathrm{NW}_{\mathrm{Si/Ge,clear}}$; the reduction is quite significant [$\kappa(\mathrm{NW}_{\mathrm{Si/Ge,clear}}) - \kappa(\mathrm{NW}_{\mathrm{Si/Ge,alloyed}})$ = 3.98 $\mathrm{Wm^{-1}K^{-1}}$].

To better understand the effect of interface alloying, we examined phonon transmission characteristics using the NEGF approach[105,106]. Here, the dynamic matrices for the G and Γ calculations were obtained from the second derivative of the SW potential energy surface with a displacement of 0.02 Å. Within the NEGF framework, each calculation system consists of a central scattering region ($\mathrm{NW}_{\mathrm{Si/Ge}}$ with alloy or clear interface) and two semi-infinite leads consisting of $\mathrm{NW}_{\mathrm{Si/Ge}}$ with clear interface.

Figure 5.15 shows the calculated phonon transmission coefficients (T_{ph}) for $\mathrm{NW}_{\mathrm{Si/Ge,alloyed}}$ and $\mathrm{NW}_{\mathrm{Si/Ge,clear}}$. Figure 5.16 presents the local phonon densities of states (LPDOS) for $\mathrm{NW}_{\mathrm{Si/Ge,alloyed}}$ and $\mathrm{NW}_{\mathrm{Si/Ge,clear}}$ as a function of radial atomic position. LPDOS can be expressed as the imaginary part of the Green's function as $\mathrm{LPDOS}[\omega]_{ll} = -2\omega\mathbf{Im}\mathrm{Tr}_{\mathrm{x,y,z}}(G^r)_{l,l}/\pi$ where the subscript l is the index of the diagonal term of the Green's function matrix for each atom. The trace operation $\mathrm{Tr}_{\mathrm{x,y,z}}$ for each atom is only carried out in three directions.

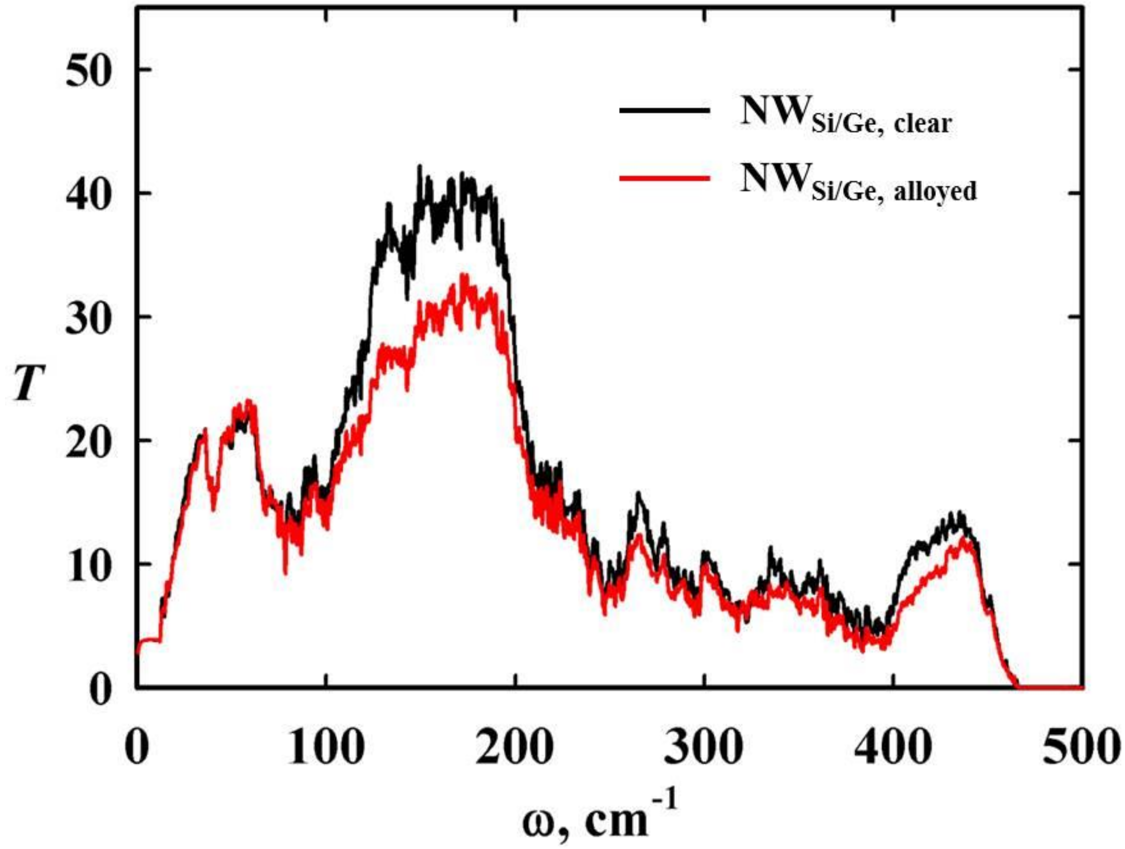

Figure 5.15: Frequency-dependent phonon transmission coefficients (T_{ph}) calculated for Si/Ge core-shell nanowire having clear (black line) or alloyed (red line) interface.

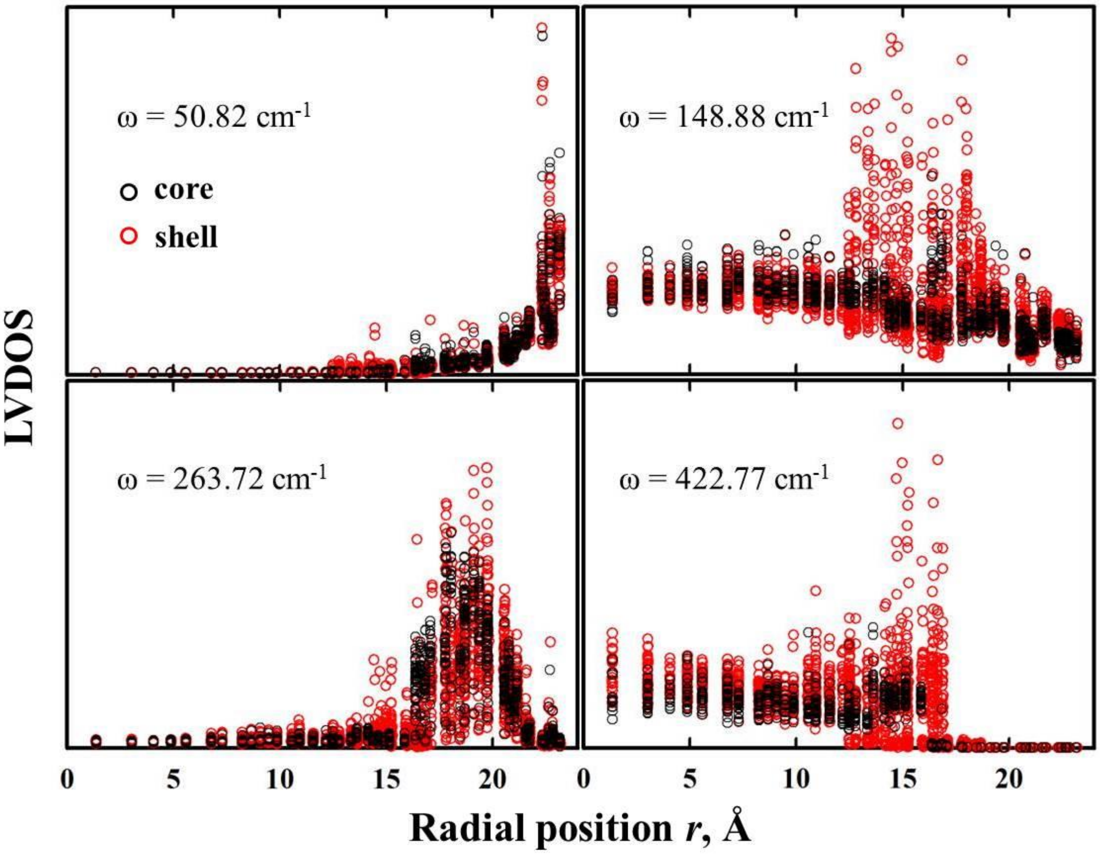

Figure 5.16: Local vibrational density of states (LVDOS) for atoms as a function of radial position (r) of atoms, at four frequencies (ω = 50.82, 148.88, 263.72, and 422.77 cm^{-1}) where significant suppression of T_{ph} is observed. Open black or red circles correspond to LVDOS of atoms in core or shell.

Compared to T_{ph} for $\mathrm{NW_{Si/Ge,clear}}$, it is clearly shown that T_{ph} for $\mathrm{NW_{Si/Ge,alloyed}}$ are strongly suppressed in the frequency range between 100 and 200 $\mathrm{cm^{-1}}$ where a significant amount of transmission channels exist. For $\mathrm{NW_{Si/Ge,clear}}$, phonon modes between 100 $\mathrm{cm^{-1}}$ and 200 $\mathrm{cm^{-1}}$ are involved in both Si core and Ge shell because the PDOSs for Ge shell and Si core largely overlap in this frequency region. At the radial position of about r = 17 Å where the interface between core and shell exists, phonon modes are localized on heavy Ge atoms due to alloy scattering of phonons. When the interface is alloyed, this localization becomes significant and occurs in a wider range of r, which results in significant suppression of T_{ph}. This enhancement of phonon mode localization due to alloy scattering near the interface is also observed for other regions. For example, at ω = 263.72 $\mathrm{cm^{-1}}$ (or 422.77 $\mathrm{cm^{-1}}$), phonon modes are mainly engaged in the Ge shell (or Si core) because these modes correspond to Ge-Ge (or Si-Si) vibrations. When the interface is alloyed, T_{ph} are reduced. However, for the low frequency regime ($\omega < 100$ $\mathrm{cm^{-1}}$), T_{ph} are nearly unaffected by the interfacial alloying, because phonon modes participate only the near-surface region of NWs as shown in Fig. 5.16.

5.5 Interplay between Alloy Scattering and Grain Boundary Scattering in Polycrystalline SiGe Alloys

5.5.1 Development of Computational Approach for Generating Polycrystalline Sitructure

It is a very challenging and computationally intensive task to generate atomistic models for polycrystalline materials, because we need to accurately reproduce both local and global structural features such as grain size, shape distribution, and grain boundary atomic architecture. There have been several previous attempts to generate polycrystalline Si or SiGe using MD simulations [242,243]. However, as one kind of covalent bonding systems, the properties of polycrystalline Si or SiGe are highly affected by bonding configurations at grain boundaries. Therefore, we attempted to develop a new multistep approach to generate polycrystalline SiGe structures by integrating MD and Continuous-Random-Network model based Metropolis Monte Carlo (CRN-MMC) simulations.

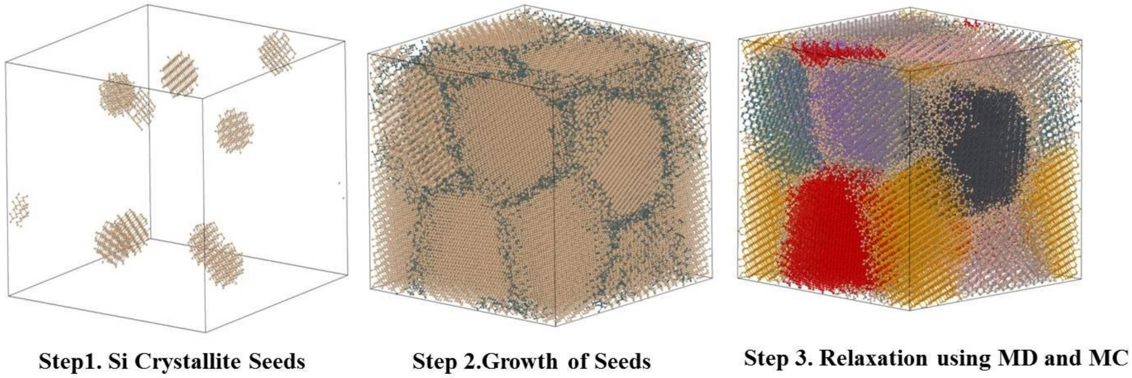

Figure 5.17: Schematic showing procedures for preparing polycrystalline structures. In step 2, green atoms indicate interfacial regions. In step 3, different colored regions represent crystallite grains.

First, in an empty cubic simulation cell, small crystalline Si seeds were randomly placed with different orientations (see Fig 5.17). Then, each crystalline seed was allowed to grow until nanocrystalline Si was obtained. The total number of atoms in a supercell was set at the *c*-Si density (= 2.28 g/cm^3)[228]. Next, for preliminary relaxation, the polycrystalline structures were annealed at T = 500 K for 200 ps using MD, while maintaining non-interfacial parts fixed. Finally, the entire structures were fully relaxed using CRN-MMC simulations with the Keating-like potential optimized with the aid of density functional theory (DFT) calculations.

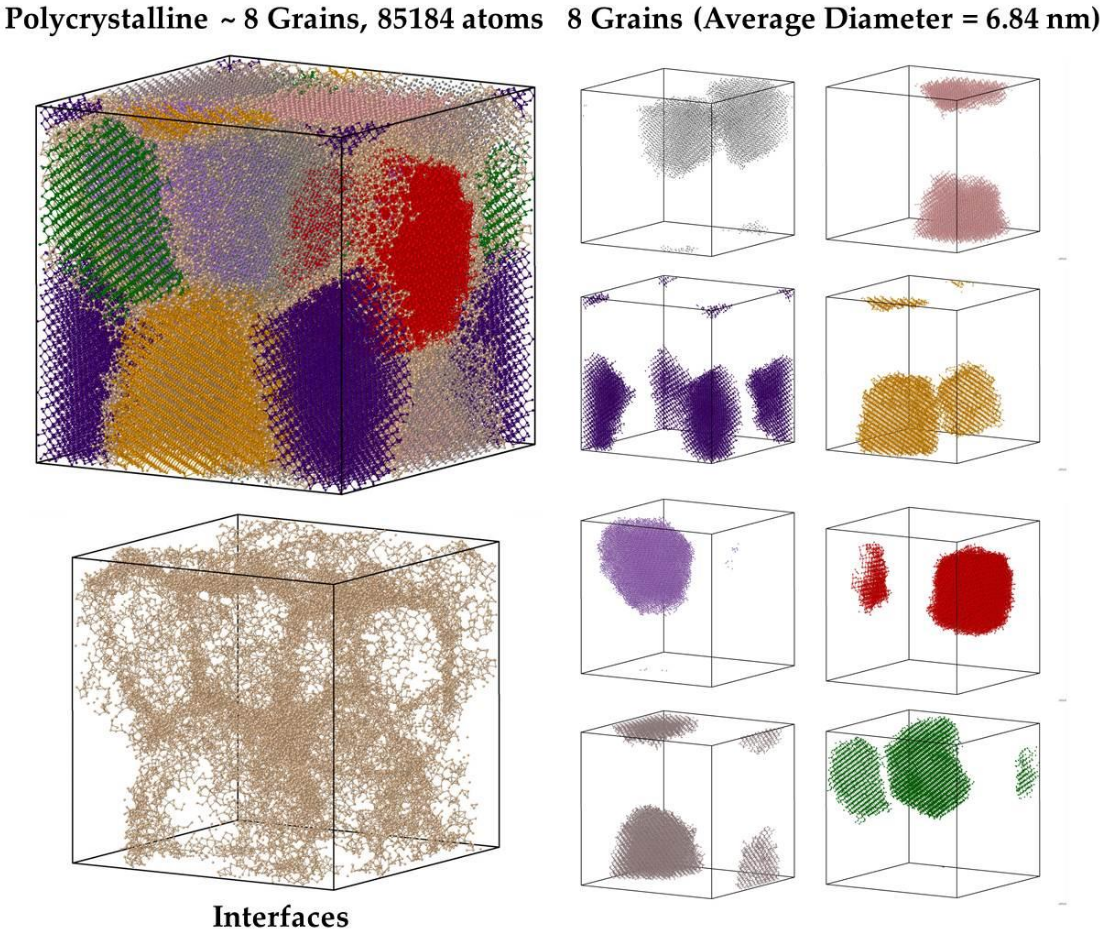

Figure 5.18: Schematic showing a polycrystalline structure prepared by a new multi-step approach. This structure has 8 grains with average diameter = 6.84 nm.

In order to consider the randomness and size effects on the κ of polycrystalline Si (*pc*-Si) structures, three sizes of simulation cell were prepared; i) (8.185 nm × 8.185 nm × 8.185 nm) cube containing 8 grains (average size = 4.31 nm), (10.914 nm × 10.914 nm × 10.914 nm) cube containing 16 grains (average size = 4.72 nm), and (12.005 nm × 12.005 nm × 12.005 nm) cube containing 8 grains (average size = 6.84 nm).

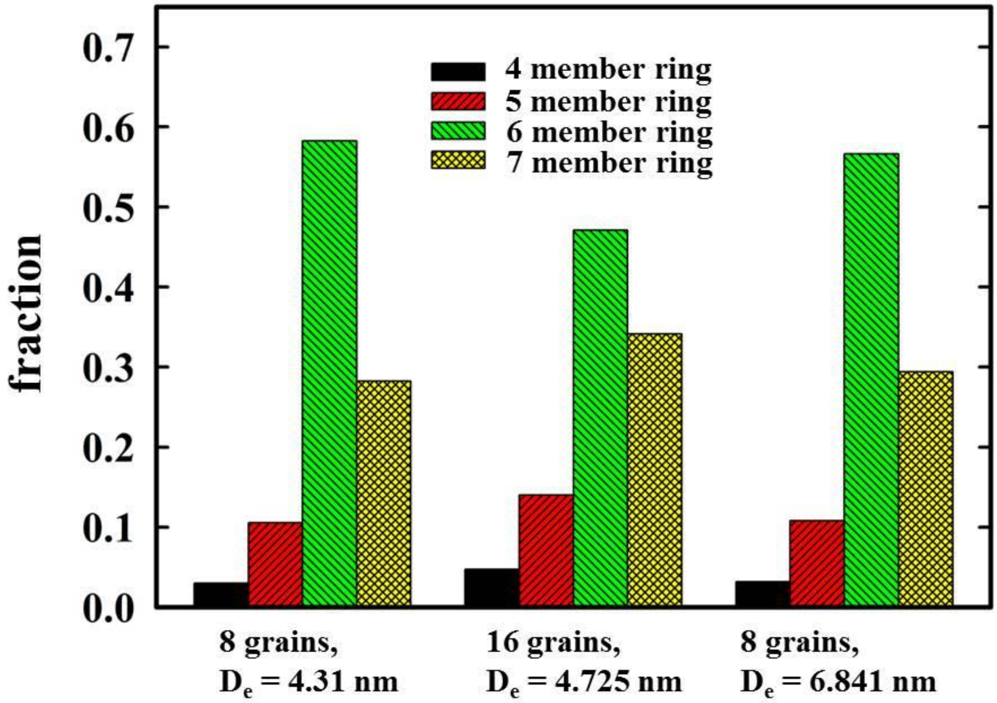

Figure 5.19: Fraction of four, five, six, or seven member ring for polycrystalline structures prepared using a new multistep approach.

For the *pc*-Si structures constructed, analysis of ring sizes at the ground boundaries was performed, and the distribution of ring sizes for each sample are shown in Fig 5.19. For all the samples, 6 membered rings are dominant.

After obtaining fully relaxed *pc*-Si structures, polycrystalline SiGe (*pc*-SiGe) structures were prepared. In order to investigate the interplay between alloy and grain boundary scatterings of phonons, we generated three different types of *pc*-SiGe samples at composition ratio of Si/Ge = 80/20. First, we generated polycrystalline structures consisting of Si and Ge chunks which are similar to experimentally obtained structures via high energy ball milling[33,244]. For *pc*-$Si_{0.8}Ge_{0.2}$, one-fourth of Si crystallites was randomly chosen and replaced with Ge atoms. And the interfaces between Si and Ge were alloyed to set the overall composition ratio of Si/Ge to be 80/20. Next, we prepared polycrystalline SiGe structures consisting of SiGe crystallines. In this case (*pc*-$Si_{0.8}Ge_{0.2}$(R)), Si atoms of *pc*-Si were randomly replaced with Ge atoms throughout the entire cells, at 20% Ge content. Also, for the references, single crystalline $Si_{0.8}Ge_{0.2}$ alloys (*sc*-$Si_{0.8}Ge_{0.2}$) were prepared. The lattice parameter of polycrystalline structures was set according to Vergard's law which is a linear interpolation between the lattice constants from the DFT calculation. Prepared *pc*-SiGe structures underwent further careful relaxation. Resulting structures are shown in Fig 5.20.

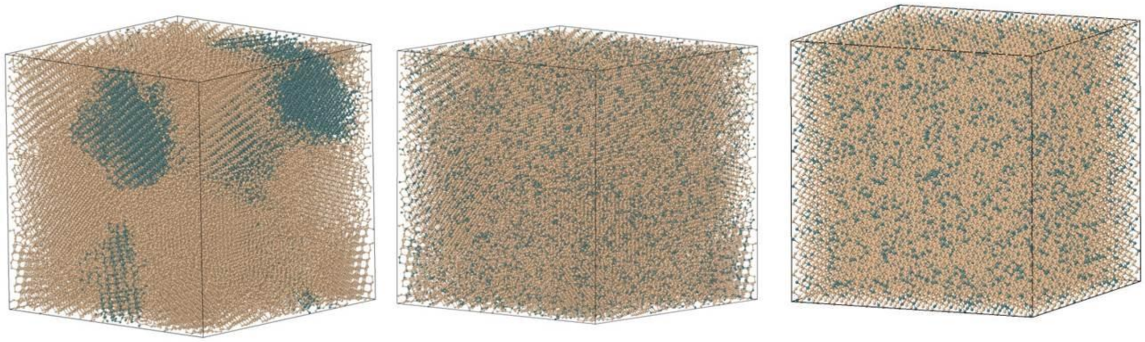

$\boldsymbol{pc}$-$\mathbf{Si_{0.8}Ge_{0.2}}$ $\boldsymbol{pc}$-$\mathbf{Si_{0.8}Ge_{0.2}(R)}$ $\boldsymbol{sc}$-$\mathbf{Si_{0.8}Ge_{0.2}}$

Figure 5.20: Polycrystalline alloy structure *pc*-$Si_{0.8}Ge_{0.2}$ (or *pc*-$Si_{0.8}Ge_{0.2}$(R)) consisted of Si and Ge crystallites (or SiGe alloy crystallites) and single-crystalline alloy structure *sc*-$Si_{0.8}Ge_{0.2}$.

5.5.2 Investigation of Heat Transport in Polycrystalline Si and SiGe alloys

In order to calculate the κ values at 300K, EMD using the LAMMPS, was employed. For EMD simulations, we employed a general form of SW potential function with modified parameters using a force-matching method[71] based on DFT calculations. In EMD simulations, the periodic boundary condition is applied in all three directions and each MD timestep is 0.5 fs. All reported values are quantum corrected ones.

Our calculation results are summarized in Table 5.4. First, it is observed that the reduction of κ in *pc*-Si is significant, compared to that of *c*-Si from previous MD simulations (κ = 136.65 $Wm^{-1}K^{-1}$)[71] and experiments (κ = 156.38 $Wm^{-1}K^{-1}$)[165]. The predicted κ values for *pc*-Si are consistent with previous MD calculations [244]. In addition, our results clearly indicate that the κ of *pc*-Si increases with grain size, which is consistent with previous studies [244] because the strength of grain boundary scattering is proportional to 1/grain size. For *pc*-$Si_{0.8}Ge_{0.2}$ consisting of Si and Ge crystallites, the κ values are reduced by about 20% compared to those of *pc*-Si at the corresponding grain sizes, and consistent with previous experimental results[245]. Interestingly, for *pc*-$Si_{0.8}Ge_{0.2}$(R) having a random distribution throughout the entire system, the κ values decrease by about 54%, 53%, and 67 % compared to those of corresponding *pc*-$Si_{0.8}Ge_{0.2}$. Furthermore, the κ values for *pc*- $Si_{0.8}Ge_{0.2}$(R) are about 40~50% smaller than those of sc-$Si_{0.8}Ge_{0.2}$.

Table 5.4: Summary of calculated thermal conductivities (κ) for polycrystalline structures.

	8 grains, D_e = 4.31 nm	16 grains, D_e = 4.725 nm	8 grains, D_e = 6.841 nm
	κ, $Wm^{-1}K^{-1}$	κ, $Wm^{-1}K^{-1}$	κ, $Wm^{-1}K^{-1}$
pc-Si	1.906	1.932	2.509
pc-$Si_{0.8}Ge_{0.2}$	1.493	1.615	2.124
pc-$Si_{0.8}Ge_{0.2}$(R)	0.692	0.758	0.706
sc-$Si_{0.8}Ge_{0.2}$	1.693	1.574	1.552

In order to better understand these results, detailed phonon studies were performed. LVDOS was obtained by measuring the velocity autocorrelation function and taking a Fourier transform of it. LVDOS is given by $g(\omega) = \int_{-\infty}^{\infty} dt \frac{\langle v_i(t)|v_i(0)\rangle}{\langle v_i(0)|v_i(0)\rangle} e^{i\omega t}$ where v_i denotes the velocity of the *i*th atom of each part. The system was first equilibrated for 1.0 *ns* using the Nose-Hoover thermostat at 300K and the correlation value is calculated for every 3 *fs* and for a total time period of 12 *ps* in the micro-canonical ensemble (NVE).

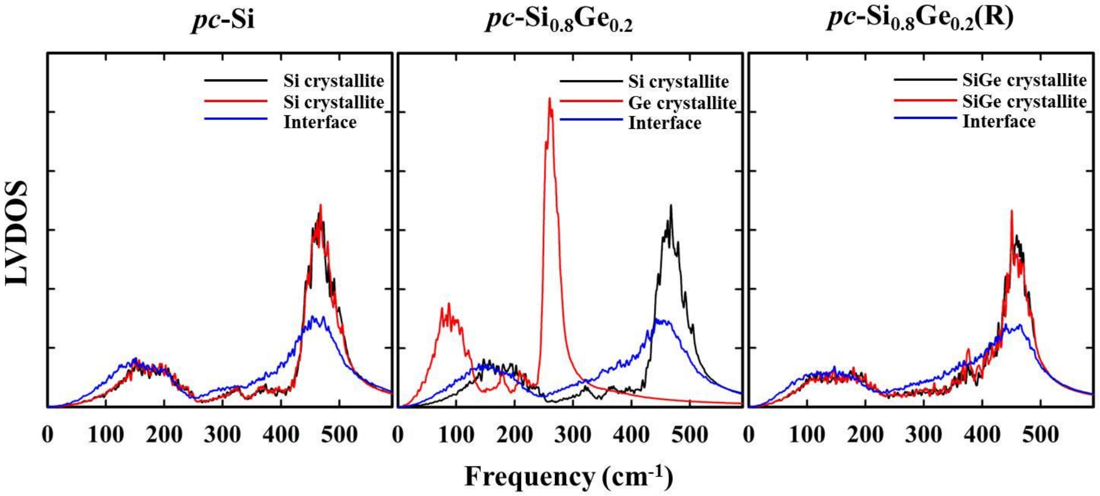

Figure 5.21: Local vibrational density of states (LVDOS) for *pc*-Si, *pc*-$Si_{0.8}Ge_{0.2}$, and *pc*-$Si_{0.8}Ge_{0.2}$(R). Black and red lines indicate LVDOS for crystalline grains, and blue lines correspond to LVDOS for interfaces.

Calculated LVDOS are shown in Fig 5.21, for *pc*-Si, *pc*-$Si_{0.8}Ge_{0.2}$, and *pc*-$Si_{0.8}Ge_{0.2}$(R), respectively. For *pc*-Si, the LVDOS for Si crystallites is analogous to bulk Si, which indicates phonons might propagate nearly without additional scatterings compared to those in bulk Si. Therefore, the reduced κ of *pc*-Si can be attributed to the interfaces between grains. As shown in Fig 5.21, the LVDOS for interfaces of *pc*-Si is highly dispersive due to induced disorder and strain, compared to that of Si crystallite, which causes strong interfacial scatterings of phonons, suppressing the mean free path (MFP) of phonon modes which have MFP longer than the grain size, in bulk Si. In addition, a large amount of disordered grain interfaces impose resistance to heat transport because of their low κ.

For *pc*-$Si_{0.8}Ge_{0.2}$, alloy scattering at the interfaces and the mismatch of vibrational frequencies between Si and Ge crystallites additionally impose impedance to heat flow.

The very small κ for *pc*-$Si_{0.8}Ge_{0.2}$(R) can be explained by a combination of alloy scattering of phonons mainly in the high frequency region and strong grain boundary scattering of phonons in the low frequency region. As shown in Fig 5.21, LPDOS for each crystallite becomes significantly dispersive, due to strong alloy scattering within crystallites.

Chapter 6. Summary

6.1 Overview

We have developed a new computational scheme that can be used to predict and explain complicate thermal transport phenomena in various disordered and Si-based nanostructured materials, with an overarching goal of identifying high quality and performance materials for applications in nano/micro-electronics and energy generation/storage application. The key features of the computational platform include (1) construction of realistic nanostructures with atomic-scale precision, (2) first principles-based determination of reliable force fields for κ calculation, (3) direct simulation of phonon transport in large disordered systems using massively parallel computing, and (4) detailed analysis of phonon properties to better understand complicate phonon transport phenomena in nanostructured materials. This program couples various state-of-the-art computational methods including quantum mechanics, non-equilibrium MD, Monte Carlo, non-equilibrium Green's function, multivariable optimization, and massively parallel computing. We have applied the newly developed computational approach to explain and predict the thermal transport properties of various Si-based disordered and complex nanostructures. Summary of our findings are as follows.

In chapter 3, effect of various kinds of defects on heat transport in c-Si was investigated. First, we have revealed the effects of vacancy defects on the κ of c-Si. According to the results, κ rapidly drops with an inverse power-law relation as the vacancy concentration increases. Our calculations suggest that the reduction of κ with vacancy concentration is a function of vacancy cluster size; smaller clusters tend to more effectively inhibit phonon transport for the same concentration. Second, for four different dopant elements (B, Al, P, and As), we analyzed the relative roles played by the differences in atomic mass (mass disorder) and atomic radius (lattice strain) as well as the hetero bonds (bond disorder) between host and dopant atoms in the κ suppression of Si by doping-induced phonon-impurity scatterings. Our study demonstrates that the mass disorder effect is primarily responsible for the suppression of κ in the As- and B-doped cases, whereas the bond disorder contribution is found to be more important than the mass disorder contribution in the Al- and P-doped cases; for all these systems, the lattice strain effect turns out to play a minor role in the reduction of κ. Third, we have elucidated the effect of the As_4V complex on the κ of *c*-Si and the origin of enhanced phonon scattering by As_4V compared to substitutional As. Our calculations demonstrate that the vacancy presence at the As_4V center leads to a stronger local resonance scattering of phonons, which significantly suppresses long range phonons at frequencies below 130 cm^{-1} which are important heat carries in *c*-Si.

Alloying effects on heat transport in SiGe alloys were investigated in chapter 4. First, we have investigated the dependence of predicted κ value for SiGe alloys on the supercell size employed in MD simulations. Our calculations turned out that the supercell size should be sufficiently larger than mean free paths of phonons in SiGe alloys, in order to obtain a fully converged κ value. This result may address the necessity of employing MD calculations for studying heat transport in disordered systems. Next, we have investigated the dependence of the magnitude of alloy scattering of phonons as a function of composition ratio. Our calculations address the strong dependence of κ on the Si:Ge ratio and the occurrence of the minimum κ around $Si_{0.8}Ge_{0.2}$, consistent with existing experimental observations. Moreover, based on a few previous experimental evidences that a fraction of Si and Ge atoms may remain locally segregated in mechanically alloyed SiGe samples, we attempted to answer an important question that alloy segregation may perhaps affect alloy scattering and subsequently alter noticeably κ. Our study clearly demonstrates that the κ of $Si_{0.8}Ge_{0.2}$ increases substantially and monotonically as Ge atoms undergo segregation; that is, the magnitude of alloy scattering is found to be sensitive to homogeneity in the distribution of alloying elements. Lastly, the possibility that the alloying of Sn with Si and Ge may allow for ultra-low κ below alloy limit of κ in binary SiGe alloys was tested. This study included the first time ever quantum accurate force field optimization for Sn alloying systems. Our calculations revealed that alloying with Sn further increases alloy scattering effect mainly due to heavy mass of Sn, compared to SiGe alloys.

Chapter 5 is dedicated to the analysis of heat transport in Si-based nanostructures. First, we have investigated the effect of surface structure and composition by designing NW samples with tailored morphologies on heat transport in SiNWs. Our calculations revealed that the –a-SiO_x passivation significantly reduces the κ of NWs compared to –H termination; the reductions are about 70~90 % depending on orientations of NWs and become more significant as the thickness of surface a-SiO_x increases. Second, we have revealed the relative contribution of alloying and boundary phonon scatterings on the reduction of κ of SiGeNW. From our calculation results, it was observed that the boundary scattering effect in the SiGe alloy system seems to be unimportant as alloy scattering is dominant. Third, we have found a promising approach to reduce the κ of core-shell NWs with a combination of strong alloy and surface phonon scatterings. According to our calculations, NWs consisting of Si core and SiGe alloy shell yield about 50% reduced thermal conductivities, compared to NWs with Si core and Ge shell. Interestingly, with making core as SiGe alloy(i.e. SiGe/Si core-shell NW), κ is # times more reduced. Additionally, we have generated polycrystalline Si or SiGe structures using a new computational approach integrating MD and MC, and investigated the effect of grain boundaries on thermal transport. Our calculations have found that polycrystalline SiGe alloys consisting of SiGe crystallites exhibit about 40~50% reduced κ values than those consisting of Si and Ge crystallites which are conventionally prepared in experiments.

6.2. Contribution

Besides the predictions reported herein, this computational scheme can be broadly applicable to other disordered and complex materials systems. While current experimental techniques alone are limited to providing complementary real space information, the systematic and integrated computational approach combined with experimental validations will contribute to developing a quantitative understanding of phonon transport in complex TE nanomaterials. The outcome will further provide valuable hints on how to improve the performance of existing TE devices and discover next-generation TE materials and systems.

Bibliography

1. S. Krishnan, S.V. Garimella, G.M. Chrysler, and R.V. Mahajan, “Towards a thermal Moore’s law” *IEEE. T. Compon. Pack. T* **30**, 462 (2007).
2. S. Kaur, N. Raravikar, B. A. Helms, R. Prasher, and D. F. Ogletree, “Enhanced thermal transport at covalently functionalized carbon nanotube array interfaces” *Nat. Commun.* **5**, 3082 (2014).
3. S.V. Garimella, Y.K. Joshi, A. Bar-Cohen, R. Mahajan, K.C. Toh, V.P. Carey, M. Baelmans, J. Lohan, B. Sammakia, and F. Andros, “Thermal challenges in next-generation electronic systems” *IEEE T. Compon. Pack. T* **31**, 801 (2008).
4. D. Kraemer, B. Poudel, H.-P. Feng, J.C. Caylor, B. Yu, X. Yan, Y. Ma, X. Wang, D. Wang, A. Muto, K. McEnaney, M. Chiesa, Z. Ren, and G. Chen, “High-performance flat-panel solar thermoelectric generators with high thermal concentration” *Nat. Mater.* **10**, 532 (2011).
5. S. Lee, “Thermal challenges and opportunities in concentrated photovoltaics” *Electron Packag Technol Conference (EPTC)*, 608 (2010).
6. T.M. Bandhauer, S. Garimella, and T.F. Fuller, “A critical review of thermal issues in Lithium-Ion batteries” *J. Electrochem. Soc.* **15**, R1 (2011).
7. G. J. Snyder and E. S. Toberer, “Complex thermoelectric materials” *Nat. Mater.* **7**, 105114 (2008).
8. M. Zebarjadi, K. Esfarjani, M. S. Dresselhaus, Z. F. Ren, and G. Chen, “Perspectives on thermoelectrics: from fundamentals to device applications” *Energy Environ. Sci.* **5**, 5147 (2012).
9. C. K. Chan, H. Peng, G. Liu, K. McIlwrath, X. F. Zhang, R. A. Huggins, and Y. Cui, “High-performance lithium battery anodes using silicon nanowires" *Nature. Nanotech.* **3**, 31 (2008).

10. R. Noufi and K. Zweibel, “High-efficiency CdTe and CIGS thin-film solar cells: Highlights and challenges" *Conf. paper: NREL/CP-520-39894, 4th World Conference on Photovoltaic Energy Conversion* (2006).
11. F. X. Xiu, Z. Yang, L. J. Mandalapu, D. T. Zhao, J. L. Liu, and W. P. Beyermann, “High-mobility Sb-doped p-type ZnO by molecular-beam epitaxy" *Appl. Phys. Lett.* **87**, 152101 (2005).
12. W. McCray, “MBE deserves a place in the history books" *Nature Nanotech.* **2**, 259 (2007).
13. T. Kubart, D. Depla, D. M. Martin, T. Nyberg, and S. Berg, “High rate reactive magnetron sputter deposition of titanium oxide" *Appl. Phys. Lett.* **92**, 221501 (2008).
14. G. M. Veith, A. R. Lupini, S. J. Pennycook, A. Villa, L. Prati, and N. J. Dudney, “Magnetron sputtering of gold nanoparticles onto WO3 and activated carbon" *Catal. Today* **122**, 248 (2007).
15. G. A. T. Eyck, J. J. Senkevich, F. Tang, D. Liu, S. Pimanpang, T. Karaback, G.-C. Wang, T.-M. Lu, C. Jezewski, and W. A. Lanford, “Plasma-assisted atomic layer deposition of palladium" *Chem. Vap. Deposition* **11**, 60 (2005).
16. H.-X. Zhang, J.-P. Ge, and Y.-D. Li, “High-temperature growth of silica sheathed Bi2S3 semiconductor nanowires" *Chem. Vap. Deposition* **11**, 147 (2005).
17. H. Sunami, “Dimension Increase in Metal-Oxide-Semiconductor Memories and Transistors” *Advances in Solid State Circuit Technologies, Paul K Chu (Ed.),* ISBN: 978-953-307-086-5 (2010).
18. Krishnan, S., Garimella, S. V., Chrysler, G. M. & Mahajan, R. V. Towards a thermal Moore’s law. *IEEE. T. Compon. Pack. T* **30**, 462 (2007).
19. S.V. Garimella, “Advances in mesoscale thermal management technologies for mirco electronics” *Microelectron. J.* **37**, 1165 (2006).
20. A.A. Balandin, "The heat is on: Graphene applications " *IEEE Nanotechnol. Mag.* **5**, 15 (2011).

21. D. G. Cahill, W. K. Ford, K. E. Goodson, G. D. Mahan, A. Majumdar, H. J. Maris, R. Merlin, and S. R. Phillpot, “Nanoscale thermal transport” *J. Appl. Phys.* **93**, 793 (2003).
22. E. Pop and K. E. Goodson, “Thermal phenomena in nanoscale transistors” *ASME J. Electron. Packag.* **128**, 102 (2006).
23. K. E. Goodson, L. Jiang, S. Sinha, Eric Pop, and S. Im, “Microscale thermal engineering of electronic systems” *In Rohsenow Symposioum on Future Trends of Heat Transfer*, Cambridge, MA (2003).
24. A.D. McConnell and K.E. Goodson, “Thermal conduction in silicon micro- and nanostructures” *Annu. Rev. Heat Transfer* **14**, 129 (2005).
25. F.H. Stillinger and T. A. Weber, "Computer simulation of local order in condensed phases of silicon" *Phys. Rev. B* **31**, 5262 (1985).
26. F. Ercolessi and J.B. Adams, “Interatomic Potentials from First-Principles Calculations: The Force-Matching Method” *Europhys. Lett.* **26**, 583 (1994).
27. J.S. Reid and J.D. Pirie, “Dynamic Deformation and the Debye-Waller Factors for Silicon-Like Crystals” *Acta Cryst. A* **36**, 957 (1980).
28. C. Flensburg and R.F. Stewart, “Lattice dynamical Debye-Waller factor for silicon” *Phys. Rev. B* **60**, 284 (1999).
29. https://flowcharts.llnl.gov/energy.html
30. D.M. Rowe, “CRC handbook of thermoelectrics” *CRC Press*, Boca Raton (1995).
31. R. Venkatasubramanian, E. Siivola, T. Colpitts, and B. O’Quinn, "Thin-film thermoelectric devices with high room-temperature figures of merit." *Nature* **413**, 597 (2001).
32. T.C. Harman, P.J. Taylor, M.P. Walsh, and B.E. LaForge, “Quantum dot superlattice thermoelectric materials and devices” *Science* **297**, 2229 (2002).
33. X. W. Wang, H. Lee, Y. C. Lan, G. H. Zhu, G. Joshi, D. Z. Wang, J.Yang, A. J. Muto, M. Y. Tang, J. Klatsky, S. Song, M. S. Dresselhaus, G.Chen, and Z. F. Ren, “Enhanced thermoelectric figure of merit in nanostructured n-type silicon germanium bulk alloy” *Appl. Phys. Lett.* **93**, 193121 (2008).

34. C.B. Vining, "A model for the high-temperature transport properties of heavily doped n-type silicon-germanium alloys" *J. Appl. Phys*. **69**, 331 (1991).

35. Y. Lee and G.S. Hwang, "Microsegregation effects on the thermal conductivity of silicon-germanium alloys" *J. Appl. Phys.* **114**, 174910 (2013).

36. S. Ganguly, C. Zhou, D. Morelli, J. Sakamoto, and S. Block, "Synthesis and Characterization of Telluride Aerogels: Effect of Gelation on Thermoelectric Performance of Bi_2Te_3 and $Bi_{2-x}Sb_xTe_3$ Nanostructures" *J. Phys. Chem. C* **116**, 17431 (2012).

37. G.S. Nolas, J. Poon, and M. Kanatzidis, "Thermoelectric Materials, Phenomena, and Application: A Bird's Eye View" *MRS Bull.* **31**, 199 (2006).

38. S.K. Bux, J.-P. Fleurial, R.B. Kaner, "Nanostructured Materials for Thermoelectric Applications" *Chem. Commun.* **46**, 8311 (2010).

39. M.S. Dresselhaus, G. Chen, M.Y. Tang, R.G. Yang, H. Lee, D.Z. Wang, Z.F. Ren, J.-P. Fleurial, and P. Gogna, "New directions for low-dimensional thermoelectric materials" *Adv. Materials* **19**, 1043 (2007).

40. B. Poudel, Q. Hao, Y. Ma, Y. Lan, A. Minnich, B. Yu, X. Yan, D. Wang, A. Muto, D. Vashaee, X. Chen, J. Liu, M.S. Dresselhaus, G. Chen, Z. Ren, "High-thermoelectric performance of nanostructured Bismuth Antimony Telluride bulk alloys" *Science* **2**, 634 (2008).

41. Z.-Y. Li and J.-F. Li, "Fine-grained and nanostructured AgPbmSbTem+2 alloys with high thermoelectric figure of merit at medium temperature" *Adv. Engr. Materials* **4**, 2 (2014).

42. W. Xie, A. Weidenkaff, X. Tang, Q. Zhang, J. Poon, and T.M. Tritt, "Recent advances in nanostructured thermoelectric half-heusler compounds" *Nanomaterials* **2**, 379 (2012).

43. Z.-G. Chen, G. Han, L. Yang, L. Cheng, J. Zou, "Nanostructured thermoelectric materials: current research and future challenge" *Prog. Nat. Sci.: Materials international* **22**, 535 (2012).

44. D. G. Cahill, K. E. Goodson, and A. Majumdar, "Thermometry and thermal transport in micro/nanoscale solid-state devices and structures" *ASME J. Heat Transfer* **124**, 223 (2002).

45. J. M. Ziman, "Electrons and Phonons: The Theory of Transport Phenomena in Solids", *Claren-don Press*, Oxford (1960).

46. R.E. Peierls, "Quantum Theory of Solids" *Clarendon Press*, Oxford (1955).

47. P. Carruthers, "Theory of Thermal Conductivity of Solids at Low Temperatures", *Rev. Mod. Phys.* **33**, 92 (1961).

48. A.J.H. McGaughey and M. Kaviany, "Phonon Transport in Molecular Dynamics Simulations: Formulation and Thermal Conductivity Prediction", *Advances in Heat Transfer* **39**, 169 (2006).

49. P. Heino, "Thermal Conduction Simulations in the Nanoscale", *J. Comput. Theor. Nanos.* B, 896 (2007).

50. M. Michel, G. Mahler, and J. Gemmer, "Fourier's Law from Schrodinger Dynamics", *Phys. Rev. Lett.* **95**, 180602 (2005).

51. D. Segal, A. Nitzan, and P. Hänggi, "Thermal conductance through molecular wires", *J. Chem. Phys.* **119**, 6840 (2003).

52. D. A. Broido, M. Maloney, G. Birner, N. Mingo, and D. Stewart, "Intrinsic lattice thermal conductivity of semiconductors from first principles" *Appl. Phys. Lett.* **91**, 231922 (2007).

53. K. Esfarjani, G. Chen, and H. T. Stokes, "Heat transport in silicon from firstprinciples calculations" *Phys. Rev. B* **84**, 085204 (2011).

54. L. Lindsay, D. A. Broido, and T. L. Reinecke, "Thermal conductivity and large isotope effect in GaN from first principles" *Phys. Rev. Lett.* **109**, 095901 (2012).

55. M. N. Luckyanova, J. Garg, K. Esfarjani, A. Jandl, M. T. Bulsara, A. J. Schmidt, A. J. Minnich, S. Chen, M. S. Dresselhaus, Z. Ren, E. A. Fitzgerald, and G. Chen, "Coherent phonon heat conduction in superlattices" *Science* **338**, 936939 (2012).

56. W. Li, L. Lindsay, D. A. Broido, D. A. Stewart, and N. Mingo, “Thermal conductivity of bulk and nanowire $Mg_2Si_xSn_{1-x}$ alloys from first principles” *Phys. Rev. B* **86**, 174307 (2012).

57. J. Garg, N. Bonini, B. Kozinsky, and N. Marzari, “Role of Disorder and Anharmonicity in the Thermal Conductivity of Silicon-Germanium Alloys: A First-Principles Study” *Phys. Rev. Lett.* **106**, 045901 (2011).

58. A. Kundu, N. Mingo, D. A. Broido, and D. A. Stewart, “Role of light and heavy embedded nanoparticles on the thermal conductivity of SiGe alloys” *Phys. Rev. B* **84**, 125426 (2011).

59. Z. Tian, K. Esfarjani, and G. Chen, “Enhancing phonon transmission across a Si/Ge interface by atomic roughness: First-principles study with the green’s function method” *Phys. Rev. B* **86**, 235304 (2012).

60. P.K. Schelling, S.R. Phillpot, and P. Keblinski, “Comparison of atomic-level simulation methods for computing thermal conductivity” *Phys. Rev. B* **65**, 144306 (2002).

61. Y.H. Lee, R. Biswas, C.M. Soukoulis, C.Z. Wang, C.T. Chan, and K.M. Ho, “Molecular-dynamics simulation of thermal conductivity in amorphous silicon” *Phys. Rev. B* **43**, 6573 (1991).

62. S.S. Mahajan, G. Subbarayan, and B.G. Sammakia, “Estimating thermal conductivity of amorphous silica nanoparticles and nanowires using molecular dynamics simulations” *Phys. Rev. E* **76**, 056701 (2007).

63. J. Che, T. Cagin, and W.A. Goddard III, “Thermal conductivity of carbon nanotubes” *Nanotechnology* **11**, 65 (2000).

64. J.-P. Crocombette, and L. Proville, “Effect of point defects on the phonon thermal conductivity of bcc iron” *Appl. Phys. Lett.* **98**, 191905 (2011).

65. Y. Lee, S. Lee, and G.S. Hwang, “Effects of vacancy defects on thermal conductivity in crystalline silicon: A nonequilibrium molecular dynamics study” *Phys. Rev. B* **83**, 125202 (2011).

66. N. Yang, G. Zhang, and B. Li, “Ultralow Thermal Conductivity of Isotope-Doped Silicon Nanowires” *Nano Lett.* **8**, 276 (2008).

67. Ponomareva, D. Srivastava, and M. Menon, “Thermal Conductivity in Thin Silicon Nanowires: Phonon Confinement Effect” *Nano Lett.* **7**, 1155(2007).

68. D. Donadio and G. Galli, "Atomistic simulations of heat transport in silicon nanowires.", *Phys. Rev. Lett.* **102**, 195901 (2009).

69. Y. He, D. Donadio, J.-H. Lee, J.C. Grossman, and G.Galli, “Thermal Transport in Nanoporous Silicon: Interplay between Disorder at Mesoscopic and Atomic Scales” *ACS Nano* **5**, 1839 (2011).

70. A. Skye, and P.K. Schelling, “Thermal resistivity of Si-Ge alloys by molecular-dynamics simulation” *J. Appl. Phys.* **103**, 113524 (2008).

71. Y. Lee and G. S. Hwang, "Force-matching-based parameterization of the Stillinger-Weber potential for thermal conduction in silicon" *Phys. Rev. B* **85**, 125204 (2012).

72. F. Muller-plathe, "A simple nonequilibrium molecular-dynamics method for calculating the thermal-conductivity" *J. Chem. Phys.* **106**, 6082 (1997).

73. M.S. Green, "Markoff Random Processes and the Statistical Mechanics of Time-Dependent Phenomena" *J. Chem. Phys.* **20**, 1281 (1952).

74. S.G. Volz and G. Chen, "Molecular-dynamics simulation of thermal conductivity of silicon crystals." *Phys. Rev. B* **61**, 2651 (2000).

75. H.B. Callen and T.A. Welton, "Irreversibility and Generalized Noise." *Phys. Rev.* **83**, 34 (1951).

76. S. Plimpton, “Fast Parallel Algorithms for Short-Range Molecular Dynamics.” *J. Comput. Phys.* **117**, 1 (1995).

77. C. Oligschleger and J. C. Schön, "Simulation of thermal conductivity and heat transport in solids." *Phys. Rev. B* **59**, 4125 (1999).

78. Maiti, G.D. Mahan, and S.T. Pantelides, “Dynamical simulations of nonequilibrium processes – Heat flow and the Kapitza resistance across grain boundaries” *Solid State Commun.* **102**, 517 (1997).

79. D. A. McQuarrie, Statistical Mechanics, *University Science Books*, Sausalito (2000)

80. J.E. Turney, A.J.H. McGaughey, and C.H. Amon, “Assessing the applicability of quantum corrections to classical thermal conductivity predictions” *Phys. Rev. B* **79**, 224305 (2009)

81. J. Tersoff, “New empirical approach for the structure and energy of covalent systems” *Phys. Rev. B* **37**, 6991 (1988).

82. X.-P. Li, G. Chen, P.B. Allen, and J.Q. Broughton, “Energy and vibrational spectrum of the Si(111) (7×7) surface from empirical potential” *Phys. Rev. B* **38**, 3331 (1988).

83. M. Karimi, H. Yates, J.R. Ray, T. Kaplan, and M. Mostoller, “Elastic constants of silicon using Monte Carlo simulations” *Phys. Rev. B* **58**, 6019 (1998).

84. E.R. Cowley, “Lattice Dynamics of Silicon with Empirical Many-Body Potentials” *Phys. Rev. Lett.* **60**, 2379 (1988).

85. C. Kittel, “Introduction to Solid State Physics”, 7th Ed. Wiley, New York (2006).

86. M.T. Dove, “Introduction to lattice dynamics”, *Cambridge University Press* (1993).

87. Z. Jian, Z. Kaiming, and X. Xide, “Modification of Stilling-Weber potentials for Si and Ge” *Phys. Rev. B* **41**, 12915 (1990).

88. L. Lindsay and D.A. Broido, “Optimized Tersoff and Brenner empirical potential parameters for lattice dynamics and phonon thermal transport in carbon nanotubes and graphene” *Phys. Rev. B* **81**, 205441 (2010).

89. J.P. Perdew, Y. Wang, “Accurate and simple analytic representation of the electron-gas correlation energy” *Phys. Rev. B* **45**, 13244 (1992).

90. G. Kresse and J. Furthmuller, VASP the guide (Vienna University of Technology, Vienna, 2001).

91. D. Vanderbilt, “Soft self-consistent pseudopotentials in a generalized eigenvalue formalism” *Phys. Rev. B* **41**, 7892 (1990).

92. G. Nilsson and G. Nelin, “Phonon Dispersion Relations in Ge at 80ºK” *Phys. Rev. B* **3**, 364 (1971).

93. G. Nilsson and G. Nelin, “Study of the Homology between Silicon and Germanium by Thermal-Neutron Spectrometry” *Phys. Rev. B* **6**, 3777 (1972).

94. J.D. Gale, “GULP – a computer program for the symmetry adapted simulation of solids” *JCS Faraday Trans.* **93**, 629 (1997).

95. Ward, D.A. Broido, D.A. Stewart, and G. Deinzer, “Ab initio theory of the lattice thermal conductivity in diamond” *Phys. Rev. B* **80**, 125203 (2009).

96. L. Lindsay and D.A. Broido, “Three-phonon phase space and lattice thermal conductivity in semiconductors” *J.Phys.: Condens. Matter* **20**, 165209 (2008).

97. D.A. Broido, A. Ward, and N. Mingo, “Lattice thermal conductivity of silicon from empirical interatomic potentials” *Phys. Rev. B* **72**, 014308 (2005).

98. Zhang, J. He, T. J. Zhu, S. N. Zhang, X. B. Zhao, and T. M. Tritt, “High figures of merit and natural nanostructures in $Mg_2Si_{0.4}Sn_{0.6}$ based thermoelectric materials” *Appl. Phys. Lett.* **93**, 102109 (2008).

99. G. Henkelman, A. Arnaldsson, and H. Jonsson, "A fast and robust algorithm for Bader decomposition of charge density" *Comput. Mater. Sci.* **36**, 254 (2006).

100. G.V. Lewis and C.R.A. Catlow, “Potential models for ionic oxides” *J. Phys. C* **18**, 1149 (1985).

101. D. Wolf, P. Keblinski, S. R. Phillpot, J. Eggebrecht, “Exact method for the simulation of Coulombic systems by spherically truncated, pairwise r-1 summation” *J. Chem. Phys.* **110**, 8254 (1999).

102. E. E. Gdoutos. R. Agrawal, and H.D. Espinosa, “Comparison of the Ewald and Wolf methods for modeling electrostatic interactions in nanowires” *Int. J. Numer. Meth. Eng.* **84**, 1541 (2010).

103. D.J. Adams, “On the use of the Ewald summation in computer simulation” *J. Chem. Phys.* **78**, 2585 (1983).

104. J. Shiomi, K. Esfarjani, and G. Chen, “Thermal conductivity of half-Heusler compounds from first-principles calculations” *Phys. Rev. B* **84**, 104302 (2011).

105. Bodapati, P.K. Schelling, S.R. Phillpot, and P. Keblinski, “Vibrations and thermal transport in nanocrystalline silicon” *Phys. Rev. B* **74**, 245207 (2006).

106. R.J. Bell and P. Dean, “Atomic vibrations in vitreous silica” *Discuss. Faraday Soc.* **50**, 55 (1970).

107. Madelung, Landolt-Börnstein Numerical Data and functional Relationships in Science and Technology, New Series, Group III, Springer-Verlag, Berlin, 1983, Vol.17e, p.163, 432.

108. J. Tani and H. Kido, “Thermoelectric properties of Bi-doped Mg2Si semiconductors” *Physica B* **364**, 218 (2005).

109. M.Yang, L. Zhang, and Q. Shen, “Nanostructuring and Thermoelectric Properties of Bulk N-type Mg2Si” *J. Wuhan University of Technology-Mater.Sci. Ed.* **24**, 912 (2009).

110. T. Nemoto, M. Akasaka, T. Iida, J. Sato, J. Soga, K. Nishio, T. Takei, and Y. Takanashi, 25th International Conference on Thermoelectrics: ICT 06 (2006).

111. M. Akasaka, T. Iida, T. Nemoto, J. Soga, J. Sato, K. Makino,M. Fukano, and Y. Takanashi, “Non-wetting crystal growth of Mg2Si by vertical Bridgman method and thermoelectric characteristics” *J. Cryst. Growth* **304**, 196 (2007).

112. P. Wachter, M. Filzmoser, and J. Rebizant, “Electronic and elastic properties of the light actinide tellurides” *Physica B* **293**, 199 (2001).

113. R.J. LaBotz, D.R. Mason, and D.F. O’Kane, “The thermoelectric properties of mixed crystals of $Mg_2Ge_xSi_{1-x}$” *J. Electrochem. Soc.* **110**, 127 (1963).

114. J.P. Heremans, V. Jovovic, E.S. Toberer, A. Saramat, K. Kurosaki, A. Charoenphakdee, S. Yamanaka, and G.J. Snyder, "Enhancement of thermoelectric efficiency in PbTe by distortion of the electronic density of states.", *Science* **321**, 554 (2008).

115. P.F.P. Poudeu, J. D’Angelo, A.D. Downey, J.L. Short, T.P. Hogan, and M.G. Kanatzidis, "High Thermoelectric Figure of Merit and Nanostructuring in Bulk p-type $Na_{1-x}Pb_mSb_yTe_{m+2}$", *Angew. Chem.* **118**, 3919 (2006).

116. L. Weber and E. Gmelin, "Transport properties of silicon.", *Appl. Phys. A Mater. Sci. Process.* **53**, 136 (1991).

117. W. Liu and M. Asheghi, "Thermal conduction in ultrathin pure and doped single-crystal silicon layers at high temperatures", *J. Appl. Phys.* **98**, 123523 (2005).

118. M. Asheghi, "Thermal conduction in doped single-crystal silicon films.", *J. Appl. Phys.* **91**, 5079 (2002).

119. M. Brinson and W. Dunstant, "Thermal conductivity and thermoelectric power of heavily doped n-type silicon." *J. Phys. C* **3**, 483 (2001).

120. A.D. McConnell and S. Uma, "Thermal conductivity of doped polysilicon layers." *J. Microelectromech. Syst.* **10**, 360 (2001).

121. T. M. Gibbons, B. Kang, S. K. Estreicher, and C. Carbogno, "Thermal conductivity of Si nanostructures containing defects: Methodology, isotope effects, and phonon trapping" *Phys.Rev. B* **84**, 035317 (2011).

122. S. Coffa and S. Libertino, "Room-temperature diffisivity of self-interstitials and vacancies in ion-implanted Si probed by in situ measurements" *Appl. Phys. Lett.* **73**, 3369 (1998).

123. G.S. Hwang and W.A. Goddard III, "Diffusion and dissociation of neutral divacancies in crystalline silicon" *Phys. Rev. B* **65**, 233205 (2002).

124. S. Lee, and G. S. Hwang, "Theoretical determination of stable fourfold coordinated vacancy clusters in silicon" *Phys. Rev. B* **78**, 125310 (2008)

125. S. Lee, R.J. Bondi, and G.S. Hwang, "Formation and structure of vacancy defects in silicon: Combined Metropolis Monte Carlo, tight-binding molecular dynamics, and density functional theory calculations" *Phys. Rev. B* **80**, 245209 (2009).

126. J.W. Schwartz and C.T. Walker, "Thermal Conductivity of Some Alkali Halides Containing Divalent Impurities. II. Precipitate Scattering" *Phys. Rev.* **155**, 969 (1967).

127. D.G. Cahill, and F. Watanabe, "Thermal conductivity of isotopically pure and Ge-doped Si epitaxial layers from 300 to 500 K" *Phys. Rev. B* **70**, 235322 (2004).

128. G. A. Slack, “Thermal Conductivity of Pure and Impure Silicon, Silicon Carbide, and Diamond” *J. Appl. Phys.* **35**, 3460 (1964).

129. M. Asheghi, K. Kurabayashi, R. Kasnavi, and K. E. Goodson, “Thermal conduction in doped single-crystal silicon films” *J. Appl. Phys.* **91**, 5079 (2002).

130. A.D. McConnell, U. Srinivasan, M. Asheghi, and K. E. Goodson, “Thermal conductivity of doped polysilicon layers” *J. Microelectromech. Syst.* **10**, 360 (2001).

131. P.G. Klemens, “The Scattering of Low-Frequency Lattice Waves by Static Imperfections” *Proc. Phys. Soc. London* **68**, 1113 (1955).

132. M.G. Holland, “Analysis of Lattice Thermal Conductivity” *Phys. Rev.* **132**, 2461 (1963).

133. R. Pinacho, M. Jaraiz, P. Castrillo, I. Martin-Bragado, J.E. Rubio, and J. Barbolla, "Modeling arsenic deactivation through arsenic-vacancy clusters using an atomistic kinetic Monte Carlo approach.", *Appl. Phys. Lett.* **86**, 252103 (2005).

134. M. Ramamoorthy and S. T. Pantelides, "Complex dynamical phenomena in heavily arsenic doped silicon.", *Phys. Rev. Lett.* **76**, 4753 (1996).

135. D.C. Mueller, E. Alonso, and W. Fichtner, "Arsenic deactivation in Si: Electronic structure and charge states of vacancy-impurity clusters.", *Phys. Rev. B* **68**, 045208 (2003).

136. K.C. Pandey, A. Erbil, G.S. Cargill III, R.F. Boehme, and D. Vanderbilt, "Annealing of Heavily Arsenic-Doped Silicon: Electrical Deactivation and a New Defect Complex.", *Phys. Rev. Lett.* **61**, 1282 (1988).

137. V. Ranki, J. Nissilä, K. Saarinen, "Formation of Vacancy-Impurity Complexes by Kinetic Processes in Highly As-Doped Si.", *Phys. Rev. Lett.* **88**, 105506 (2002).

138. D. Lawther, U. Myler, P.J. Simpson, P.M. Rousseau, P.B. Griffin, and J.D. Plummer, "Vacancy generation resulting from electrical deactivation of arsenic.", *Appl. Phys. Lett.* **67**, 3575 (1995).

139. D. Nobili, S. Solmi, A. Parisini, M. Derdour, A. Armigliato, and L. Moro, "Precipitation, aggregation, and diffusion in heavily arsenic-doped silicon.", *Phys. Rev. B* **49**, 2477 (1994).

140. J. Che, T. Cagin, W. Deng, and W.A. Goddard III, “Thermal conductivity of diamond and related materials from molecular dynamics simulations” *J. Chem. Phys.* **113**, 6888 (2000).

141. C.J. Glassbrenner and G.A. Slack, “Thermal Conductivity of Silicon and Germanium from 3K to the Melting Point” *Phys. Rev.* **134**, A1058 (1964).

142. Y.S. Ju and K.E. Goodson, “Phonon scattering in silicon films with thickness of order 100 nm” *Appl. Phys. Lett.* **74**, 3005 (1999).

143. J. W. Schwartz and C. T. Walker, “Thermal Conductivity of Some Alkali Halides Containing Divalent Impurities” *Phys. Rev.* **155**, 969 (1967)

144. S. Barman and G. P. Srivastava, “Quantitative estimate of phonon scattering rates in different forms of diamond” *Phys. Rev. B* **73**, 073301(2006).

145. F. Schaffler, “Properties of Advanced Semiconductor Materials GaN,AlN, InN, BN, SiC, SiGe”, edited by M. E. Levinshtein, S. L.Rumyantsev, M. S. Shur (John Wiley & Sons, Inc., New York,2001).

146. G. A. Slack, “Thermal conductivity of elements with complex lattices: B, P, S” *Phys. Rev.* **139**, A507 (1965).

147. B. Abeles, “Lattice Thermal Conductivity of Disordered Semiconductor Alloys at High Temperatures” *Phys. Rev.* **131**, 1906 (1963).

148. Y. Lee and G. S. Hwang, "Mechanism of thermal conductivity suppression in doped silicon studied with nonequilibrium molecular dynamics.", *Phys. Rev. B* **86**, 075202 (2012).

149. J.P. Crocombette and L. Proville, "Thermal conductivity degradation induced by point defects in irradiated silicon carbide." *Appl. Phys. Lett.* **98**, 191905 (2011).

150. W. Liu, K. Etessan-Yazdani, R. Hussin, K.E. Goodson, and M. Asheghi, "Modeling and data for thermal conductivity of ultrathin single-crystal SOI layers at high temperature.", *IEEE Trans. Electron Devices* **53**, 1868 (2006).

151. H. Zhang, G. Lee, and K. Cho, “Thermal transport in graphene and effects of vacancy defects” *Phys. Rev. B* **84**, 115460 (2011).

152. J.-S. Wang, J. Wang, and J.T. Lü, "Quantum thermal transport in nanostructures.", *EPJ B* **62**, 381 (2008).

153. J.-S. Wang, J. Wang, and N. Zeng, "Nonequilibrium Green’s function approach to mesoscopic thermal transport.", *Phys. Rev. B* **74**, 033408 (2006).

154. J.-S. Wang, N. Zeng, J. Wang, and C.K. Gan, "Nonequilibrium Green’s function method for thermal transport in junctions.", *Phys. Rev. E* **75**, 061128 (2007).

155. J.-W. Jiang, J.-S. Wang, and B. Li, "A nonequilibrium Green’s function study of thermoelectric properties in single-walled carbon nanotubes." *J. Appl. Phys.* **109**, 014326 (2011).

156. M.V. Klein, "Phonon Scattering by Lattice Defects.", *Phys. Rev.* **131**, 1500 (1963).

157. M. Yao, T. Watanabe, P.K. Schelling, P. Keblinski, D.G. Cahill, and S.R. Phillpot, "Phonon-defect scattering in doped silicon by molecular dynamics simulation.", *J. Appl. Phys.* **104**, 024905 (2008).

158. D.K. Brice, "Phonon Resonances Associated with Interstitial Atoms in Germanium and Silicon.", *Phys. Rev.* **140**, A1211 (1965).

159. C. Ratsifaritana and P. Klemens, "Scattering of phonons by vacancies.", *Int. J. Thermophys.* **8**, 737 (1987).

160. G. S. Nolas, J. Sharp, and H. Goldsmid, Thermoelectrics: Basic Principles and New Materials Developments(Springer, New York, 2001).

161. H. Stohr and W. Klemm, "Über Zweistoffsysteme mit Germanium. I. Germanium/Aluminium, Germanium/Zinn und Germanium/Silicium” *Z. Anorg. Allg. Chem.* **241**, 305 (1939).

162. B. Abeles, D. S. Beers, G. D. Cody, and J. P. Dismukes, “Thermal Conductivity of Ge-Si Alloys at High Temperatures” *Phys. Rev.* **125**,44 (1962).

163. J. P. Dismukes, L. Ekstrom, E. F. Steigmeier, I. Kudman, and D. S. Beers, “Thermal and Electrical Properties of Heavily Doped Ge-Si Alloys up to 1300 K” *J. Appl. Phys.* **35**, 2899 (1964).

164. M. C. Steele and F. D. Rosi, “Thermal Conductivity and Thermoelectric Power of Germanium-Silicon Alloys” *J. Appl. Phys.* **29**, 1517 (1958).

165. R. K. Kremer, K. Graf, M. Cardona, G. G. Devyatykh, A. V. Gusev, A. M. Gibin, A. V. Inyushkin, A. N. Taldenkov, and H. J. Pohl, “Thermal conductivity of isotopically enriched ^{28}Si: revisited” *Solid State Commun.* **131**, 499 (2004).

166. C. B. Vining, W. Laskow, J.O. Hanson, R. R. Van der Beck, and P. D. Gorsuch, “Thermoelectric properties of pressure-sintered Si0.8Ge0.2 thermoelectric alloys” *J. Appl. Phys.* **69**, 4333 (1991).

167. D. M. Rowe, V. S. Shukla, and N. Savvides, “Phonon scattering at grain boundaries in heavily doped fine-grained silicon-germanium alloys” *Nature* **290**, 765 (1981).

168. D. M. Rowe, L. W. Fu, and S. G. K. Williams, “Comments on the thermoelectric properties of pressure-sintered $Si_{0.8}Ge_{0.2}$ thermoelectric alloys” *J. Appl. Phys.* **73**, 4683(1993).

169. G. Joshi, H. Lee, Y. Lan, X. Wang, G. Zhu, D. Wang, R. W. Gould, D. C.Cuff, M. Y. Tang, M. S. Dresselhaus, G. Chen, and Z. Ren, “Enhanced Thermoelectric Figure-of-Merit in Nanostructured p-type Silicon Germanium Bulk Alloys” *Nano Lett.* **8**, 4670 (2008).

170. Y. Lan, A. J. Minnich, G. Chen, and Z. Ren, “Enhancement of Thermoelectric Figure-of-Merit by a Bulk Nanostructuring Approach” *Adv. Funct. Mater.* **20**, 357 (2010).

171. W. Kim, J. Zide, A. Gossard, D. Klenov, S. Stemmer, A. Shakouri, and A.Majumdar, “Thermal Conductivity Reduction and Thermoelectric Figure of Merit Increase by Embedding Nanoparticles in Crystalline Semiconductors” *Phys. Rev. Lett.* **96**, 045901 (2006).

172. Y. Bao, W. L. Liu, M. Shamsa, K. Alim, A. A. Balandin, and J. L. Liu, “Electrical and Thermal Conductivity of Ge/Si Quantum Dot Superlattices” *J. Electrochem. Soc.* **152**, G432 (2005).

173. G. Pernot, M. Stoffel, I. Savic, F. Pezzoli, P. Chen, G. Savelli, A. Jacquot,J. Schumann, U. Denker, I. Mönch, Ch. Deneke, O. G. Schmidt, J. M.Rampnoux, S. Wang, M. Plissonnier, A. Rastelli, S. Dilhaire, and N.Mingo, "Precise control of thermal conductivity at the nanoscale through individual phonon-scattering barriers" *Nature Mater.* **9**, 491 (2010).

174. J. B. Haskins, A. Kinaci, and T. Cagin, "Thermal Conductivity of Si-Ge Quantum Dot Superlattices" *Nanotechnology* **22**, 155701(2011).

175. Y. He, I. Savic´, D. Donadio, and G. Galli, "Lattice Thermal Conductivity of Semiconducting Bulk Materials: Atomistic Simulations" *Phys. Chem. Chem. Phys.* **14**, 16209 (2012).

176. J. S. Lannin, "Vibrational Properties of Concentrated Ge-Si Alloys" *Solid State Commun.* **19**, 35 (1976).

177. K. Owusu-Sekyere, W. A. Jesser, and F. D. Rosi, "Characterization of Si-Ge and Si-Ge-GaP Thermoelements" *Mater. Sci. Eng.* **B3**, 23 (1989).

178. V. R. D'Costa, C. S. Cook, J. Menéndez, J. Tolle, J. Kouvetakis and S. Zollner, "Transferability of Optical Bowing Parameters Between Binary and Ternary Group-IV Alloys" *Solid State Commun.* **138** (6), 309 (2006).

179. V. R. D'Costa, Y. Y. Fang, J. Tolle, J. Kouvetakis and J. Menéndez, "Tunable Optical Gap at a Fixed Lattice Constant in Group-IV Semiconductor Alloys" *Phys. Rev. Lett.* **102**, 107403 (2009).

180. V. R. D'Costa, Y. Y. Fang, J. Tolle, J. Kouvetakis and J. Menéndez, "Ternary GeSiSn Alloys: New Opportunities for Strain and Band Gap Engineering Using Group-IV Semiconductors" *Thin Solid Films* **518**, 2531 (2010).

181. Group IV Elements, IV-IV and III-V Compounds. Part A—Lattice Properties, Landolt-Bornstein—Group III Condensed Matter Volume €41A1a, edited by O. Madelung, U. Rossler, and M. Schulz (Springer, 2001).

182. J. M. Cowley, "An Approximate Theory of Order in Alloys" *Phys. Rev.* **77**, 669 (1950).

183. J.-H. Fournier-Lupien, S. Mukherjee, S. Wirths, E. Pippel, N. Hayazawa, G. Mussler, J.M. Hartmann, P. Desjardins, D. Buca, and O. Moutanabbir, “ Strain and Composition Effects on Raman Vibrational Modes of Silicon-Germanium-Tin Ternary Alloys” *Appl. Phys. Lett.* **103**, 263103 (2013).

184. G. Sun, R. A. Soref, and H. H. Cheng, “Design of a Si-based Lattice-Matched Room-Temperature GeSn/GeSiSn Multi-Quantum-Well Mid-Infrared Laser Diode” *Opt. Express* **18**, 19957 (2010).

185. G. Sun, R. A. Soref, and H. H. Cheng, “Design of an Electrically Pumped SiGeSn/GeSn/SiGeSn Double-Heterostructure Midinfrared Laser” *J. Appl. Phys.* **108**, 033107 (2010).

186. J. Xie, A. V. G. Chizmeshya, J. Tolle, V. R. D’Costa, J. Menendez, and J.Kouvetakis, “Synthesis, Stability Range, and Fundamental Properties of Si-Ge-Sn Semiconductor Grown Directly on Si(100) and Ge(100) Platforms” *Chem. Mater.* **22**, 3779 (2010).

187. V. D’Costa, Y.-Y. Fang, J. Tolle, J. Kouvetakis, and J. Menendez, “Tunable Optical Gap at a Fixed Lattice Constant in Group-IV Semiconductor Alloys” *Phys. Rev. Lett.* **102**, 107403 (2009).

188. S. Wirths, A. T. Tiedemann, Z. Ikonic, P. Harrison, B. Holländer, T.Stoica, G. Mussler, M. Myronov, J. M. Hartmann, D. Grützmacher, D.Buca, and S. Mantl, “Band Engineering and Growth of Tensile Strained Ge/(Si)GeSn Heterostructures for Tunnel Field Effect Transistors” *Appl. Phys. Lett.* **102**, 192103 (2013).

189. R. T. Beeler, C. Xu, D. J. Smith, G. Grzybowski, J. Menendez, and J.Kouvetakis, “Compositional Dependence of the Absorption Edge and Dark Currents in Ge1-x-ySixSny/Ge(100) Photodetectors Grown via Ultra-Low-Temperature Epitaxy of Ge4H10, Si4H10, and SnD4” *Appl. Phys. Lett.* **101**, 221111 (2012).

190. P. Moontragoon, P. Pengpit, T. Burinprakhon, S. Maensiri, N. Vukmirovic, Z. Ikonic, and P. Harrison, “Electronic Properties Calculation of Ge1-x-ySixSny Ternary Alloy and Nanostructure” *J. Non-Cryst. Solids* **358**, 2096 (2012).

191. C.G. Shirley, "A simple interpolation formula for the Debye temperatures of disordered alloys" *Acta Cryst. A* **31**, 853 (1975).

192. A.I. Hochbaum, R. Chen, R. D. Delgado, W. Liang, E. C.Garnett, M. Najarian, A. Majumdar, and P. Yang, "Enhanced Thermoelectric Performance of Rough Silicon Nanowires" *Nature* **451**, 163 (2008).

193. A.I. Boukai, Y. Bunimovich, J. Tahir-Kheli, J.-K. Yu, W.A. Goddard III, and J.R. Heath, "Silicon nanowires as efficient thermoelectric materials.", *Nature* **451**, 168 (2008).

194. D. Li, Y. Wu, R. Fan, P. Yang, and A. Majumdar, "Thermal conductivity of Si/SiGe superlattice nanowires.", *Appl. Phys. Lett.* **83**, 3186 (2003).

195. P. Martin, Z. Aksamija, E. Pop, and U. Ravaioli, "Impact of Phonon-Surface Roughness Scattering on Thermal Conductivity of Thin Si Nanowires.", *Phys. Rev. Lett.***102**, 125503 (2009).

196. T.T.M. Vo, A.J. Williamson, and V. Lordi, "Atomistic design of thermoelectric properties of silicon nanowires." *Nano Lett.* **8**, 1111 (2008).

197. F. Sansoz, "Surface Faceting Dependence of Thermal Transport in Silicon Nanowires.", *Nano Lett.* **11**, 5378 (2011).

198. J. Lim, K. Hippalgaonkar, S.C. Andrew, A. Majumdar, and P. Yang, "Quantifying Surface Roughness Effects on Phonon Transport in Silicon Nanowires.", *Nano Lett.* **12**, 2475 (2012).

199. T. Markussen, A.-P. Jauho, and M. Brandbyge, "Surface-Decorated Silicon Nanowires: A Route to High-ZT Thermoelectrics." *Phys. Rev. Lett.* **103**, 055502 (2009).

200. D. Li, Y. Wu, P. Kim, L. Shi, P. Yang, and A. Majumdar, "Thermal Conductivity of Individual Silicon Nanowires" *Appl. Phys. Lett.* **83**, 2934 (2003).

201. K. Hippalgaonkar, B. Huang, R. Chen, K. Sawyer, P.Ercius, and A. Majumdar, "Fabrication of Microdevices with Integrated Nanowires for Investigating Low-Dimensional Phonon Transport" *Nano Lett.* **10**, 4341 (2010).

202. L. Moore, S. K. Saha, R. S. Prasher, and L. Shi, “Phonon Backscattering and Thermal Conductivity Suppression in Sawtooth Nanowires” *Appl. Phys. Lett.* **93**, 083112 (2008).

203. P. Martin, Z. Aksamija, E. Pop, and U. Ravaioli, "Impact of Phonon-Surface Roughness Scattering on Thermal Conductivity of Thin Si Nanowires.", *Phys. Rev. Lett.* **102**, 125503 (2009).

204. J. Carrete, L. J. Gallego, L. M. Varela, and N. Mingo, “Surface Roughness and Thermal Conductivity of Semiconductor Nanowires: Going below the Casimir Limit” *Phys. Rev. B* **84**, 075403 (2011).

205. Z. Wang, Z. Ni, R. Zhao, M. Chen, K. Bi, and Y. Chen, “The Effect of Surface Roughness on Lattice Thermal Conductivity of Silicon Nanowires” *Physica B* **406**, 2515 (2011).

206. J. Sadhu and S. Sinha, “Room-Temperature Phonon Boundary Scattering below the Casimir Limit” *Phys. Rev. B* **84**, 115450 (2011).

207. Y. He and G. Galli, “Microscopic Origin of the Reduced Thermal Conductivity of Silicon Nanowires” *Phys. Rev. Lett.* **108**, 215901 (2012).

208. R. Yang, G. Chen, "Thermal conductivity modeling of core-shell and tubular nanowires.", *Nano Lett.* **5**, 1111 (2005).

209. E. Pokatilov, D.L. Nika, and A.A. Balandin, "Acoustic-phonon propagation in rectangular semiconductor nanowires with elastically dissimilar barriers.", *Phys. Rev. B* **72**, 113311 (2005).

210. M. Hu, K.P. Giapis, J.V. Goicochea, X. Zhang, and D. Poulikakos, "Significant reduction of thermal conductivity in Si/Ge core-shell nanowires.", *Nano Lett.* **11**, 618 (2011).

211. J. Chen, G. Zhang, and B. Li, "Phonon coherent resonance and its effect on thermal transport in core-shell nanowires.", *J. Chem. Phys.* **135**, 104508 (2011).

212. G. Zhang, W. Wang, and X. Li, "Enhanced Thermoelectric Properties of Core/Shell Heterostructure Nanowire Composites.", *Adv. Mater.* **20**, 3654 (2008).

213. M.C. Wingert, Z.C.Y. Chen, E. Dechaumphai, J. Moon, J.-H. Kim, J. Xiang, and R. Chen, "Thermal Conductivity of Ge and Ge–Si Core–Shell Nanowires in the Phonon Confinement Regime.", *Nano Lett.* **11**, 5507 (2011).

214. L. Yin, E.K. Lee, J.W. Lee, D. Whang, B.L. Choi, and C. Yu, “The Influence of Phonon Scatterings on the Thermal Conductivity of SiGe Nanowires” *Appl. Phys. Lett.* **101**, 043114 (2012).

215. H. Kim, I. Kim, H.-J. Choi, and W. Kim, “Thermal Conductivities of Si1-xGex Nanowires with Different Germanium Concentrations and Diameters” *Appl. Phys. Lett.* **96**, 233106 (2010).

216. J.A. Martinez, P.P. Provencio, S.T. Picraux, J.P. Sullivan, and B.S. Swartzentruber, “Enhanced Thermoelectric Figure of Merit in SiGe Alloy Nanowires by Boundary and Hole-Phonon Scattering” *J. Appl. Phys.* **110**, 074317 (2011).

217. E.K. Lee, L. Yin, Y. Lee, J.W. Lee, S.J. Lee, J. Lee, S.N. Cha, D. Whang, G.S. Hwang, K. Hippalgaonkar, A. Majumdar, C. Yu, B.L. Choi, J.M. Kim, and K. Kim, “Large Thermoelectric Figure-of-Merits from SiGe Nanowires by Simultaneously Measuring Electrical and Thermal Transport Properties” *Nano. Lett.* **12**, 2918 (2012).

218. L. Shi, D. Yao, G. Zhang, and B. Li, “Large Thermoelectric Figure of Merit in Si1-xGex Nanowires” *Appl. Phys. Lett.* **96**, 173108 (2010).

219. Z. Wang and N. Mingo, “Diameter Dependence of SiGe Nanowire Thermal Conductivity” *Appl. Phys. Lett.* **97**, 101903 (2010).

220. J. Chen, G. Zhang, B. Li, “Tunable Thermal Conductivity of Si1-xGex Nanowires” *Appl. Phys. Lett.* **95**, 073117 (2009).

221. S. Munetoh, T. Motooka, K. Moriguchi, and A. Shintani, “Interatomic Potential for Si-O Systems Using Tersoff Parameterization” *Comput. Mater. Sci.* **39**, 334 (2007)

222. F. de B. Mota, J.F. Justo, and A. Fazzio, “ Hydrogen role on the properties of amorphous silicon nitride” *J. Appl. Phys.* **86**, 1843 (1999).

223. R.Q. Zhang, Y. Lifshitz, D.D.D. Ma, Y.L. Zhao, Th. Frauenheim, S.T. Lee, and S.Y. Tong, "Structures and Energetics of Hydrogen-Terminated Silicon Nanowire Surfaces" *J. Chem. Phys.* **123**, 144703 (2005).

224. J. Li and A.J. Freeman, "First-Principles Determination of the Electronic Structures and Optical Properties of One-Nanometer(001) and (111) Si Nanowires" *Phys. Rev. B* **74**, 075333 (2006).

225. D.D.D. Ma, C.S. Lee, F.C.K. Au, S.Y. Tong, and S.T. Lee, "Small-Diameter Silicon Nanowire Surfaces" *Science* **299**, 1874 (2003).

226. N. Wang, Y.H. Tang, Y.F. Zhang, C.S. Lee, and S.T. Lee, "Nucleation and Growth of Si Nanowires from Silicon Oxide" *Phys. Rev. B* **58**, R16024 (1998).

227. S. Lee, R.J. Bondi, and G.S. Hwang, "Atomistic Structural Description of the Si(001)/a-SiO2 Interface: The Influence of Different Keating-Like Potential Parameters" *J. Appl. Phys.* **109**, 113519 (2011).

228. J. Sarnthein, A. Pasquarello, and R. Car, "Structural and Electronic Properties of Liquid and Amorphous SiO2: An Ab Initio Molecular Dynamics Study" *Phys. Rev. Lett.* **74**, 4682 (1995).

229. K. Laaziri, S. Kycia, S. Roorda, M. Chicoine, J.L. Robertson, J. Wang, and S.C. Moss, "High-Energy X-Ray Diffraction Study of Pure Amorphous Silicon" *Phys. Rev. B* **60**, 13520 (1999).

230. R. J. Bondi, S. Lee, G. S. Hwang, "First-Principles Study of the Structural , Electronic, and Optical Properties of Oxide-Sheathed Silicon Nanowires" *ACS NANO* **5**, 1713 (2011).

231. T. Markussen, A.-P. Jauho, and M. Brandbyge, "Heat Conductance is Strongly Anisotropic for Pristine Silicon Nanowires" *Nano Lett.* **8** 3771 (2008).

232. N. Mingo, "Calculation of Si nanowire thermal conductivity using complete phonon dispersion relations" *Phys. Rev. B* **68**, 113308 (2003).

233. A.J.H. McGaughey, E.S. Landry, D.P. Sellan, and C.H. Amon, "Size-dependent model for thin film and nanowire thermal conductivity" *Appl. Phys. Lett.* **99**, 131904 (2011).

234. R. Chen, A.I. Hochbaum, P. Murphy, J. Moore, P. Yang, and A. Majumdar,"Thermal conductance of thin silicon nanowires" *Phys. Rev. Lett.* **101**, 105501 (2008).

235. J. Dismukes, L. Ekstrom, E.F. Steigmeier, I. Kudman, and D.S. Beers, "Thermal and Electrical Properties of Heavily Doped Ge-Si Alloys up to 1300 °K.", *J. Appl. Phys.* **35**, 2899 (1964).

236. M. Steele and F. Rosi, "Thermal Conductivity and Thermoelectric Power of Germanium-Silicon Alloys." , *J. Appl. Phys.* **29**, 1517 (1958).

237. X. Yang, A.C. To, and R. Tian, “Anomalous Heat Conduction Behavior in Thin Finite-Size Silicon Nanowires” *Nanotechnology* **21**, 155704 (2010).

238. M. Hu, K.P. Giapis, J.V. Goicochea, X. Zhang, and D. Poulikakos, "Significant reduction of thermal conductivity in Si/Ge core-shell nanowires.", *Nano Lett.* **11**, 618 (2011).

239. A. Paul, M. Luisier, and G. Klimeck, “Shape and Orientation Effects on the Ballistic Phonon Thermal Properties of Ultra-Scaled Si Nanowires” *J. Appl. Phys.* **110**, 114309 (2011)

240. M. Hu, X. Zhang, K.P. Giapis, and D. Poulikakos, "Thermal conductivity reduction in core-shell nanowires.", *Phys. Rev. B* **84**, 085442 (2011).

241. R. Meyer and D. Comtesse, “Vibrational density of states of silicon nanoparticles”, *Phys. Rev. B* **83**, 014301 (2011).

242. C. Melis and L. Colombo, “Lattice Thermal Conductivity of $Si_{1-x}Ge_x$ Nanocomposites” *Phys. Rev. Lett.* **112**, 065901 (2014)

243. C.A. da Cruz, N.A. Katcho, N. Mingo, and R.G.A. Veiga, “Thermal Conductivity of Nanocrystalline SiGe Alloys Using Molecular Dynamics Simulations” *J. Appl. Phys.* **114**, 164310 (2013).

244. S. Ju and X. Liang, “Thermal Conductivity of Nanocrystalline Silicon by Direct Molecular Dynamics Simulation” *J. Appl. Phys.* **112**, 064305 (2012).

245. R. Basu, S. Bhattacharya, R. Bhatt, M. Roy, S. Ahmad, A. Sinqh, M. Navaneethan, Y. Hayakawa, D.K. Aswal, and S.K. Gupta, "Improved

thermoelectric performance of hot pressed nanostructured n-type SiGe bulk alloys" *J. Mater. Chem. A* **2**, 6922 (2014).

Vita

Yongjin Lee was born in Incheon, Korea on 5 March, 1980, the second son of Jongman Lee and Moonhwa Hur. After graduating from Seoincheon High School in Incheon, Korea, in 1999, he entered Seoul National University in Seoul, Korea. While in college, he completed his military service in 2001-2003. In February of 2006, he graduated from Seoul National University with a Bachelor of Science in Chemical and Biological Engineering. He received the Master of Science degree in Chemical and Biological Engineering from Seoul National University in 2008. In August of 2009, he entered the Graduate School at the University of Texas at Austin to pursue a Ph.D. and began research under the guidance of Professor Gyeong S. Hwang in the Department of Chemical Engineering.

Permanent address: Guwol-dong 6-3, Namdong-gu,
Incheon 405-823,
Republic of Korea

This dissertation was typed by the author.